CCBDI READOUT CIRCUIT FOR YBaCuO MICROMACHINED MICROBOLOMETERS

by

SANDEEP KUMAR

Presented to the Faculty of the Graduate School of

The University of Texas at Arlington in Partial Fulfillment

of the Requirements

for the Degree of

DOCTOR OF PHILOSOPHY

THE UNIVERSITY OF TEXAS AT ARLINGTON

May 2007

Copyright © by Sandeep Kumar 2007

All Rights Reserved

To Lord Jesus Christ

ACKNOWLEDGEMENTS

I would like to express my sincere thanks and deep appreciation to my dissertation supervisor, Prof. Donald Butler for his encouragement, support and guidance in my research work. He has been providing me with good understanding and approach during different phases of the assigned project. His immense knowledge and deep intellect are the guiding factors for my efforts in completing the design and fabrication involved in the research.

I would like to thank the members of my dissertation committee, Prof. Zeynep Celik-Butler, Prof. Jonathan Bredow, Prof. Jung-Chih Chiao and Prof. Choong-Un Kim for their valuable time and suggestions for further improvement.

I am grateful to the NanoFab staff for all their help and support. My special thanks to Dennis Bueno for all his help and time spent in productive technical discussions related to fabrication in Cleanroom. I would like to express appreciation to my colleagues in the microsensors and noise laboratories for their help and friendship.

With all my hearts, I am extremely grateful to my father Krishan and mother, Kusum, for all their love, blessings, support and encouragement in achieving the target.

With my whole being, I submit my dissertation work to the pure grace of my glorious Lord Jesus Christ in the Triune God.

This project is supported by Air Force Office of Scientific Research.

May 14, 2007

ABSTRACT

CCBDI READOUT CIRCUIT FOR YBaCuO MICROMACHINED MICROBOLOMETERS

Publication No. ______

Sandeep Kumar, PhD.

The University of Texas at Arlington, 2007

Supervising Professor: Dr. Donald P. Butler

Semiconducting YBaCuO (Yttrium-Barium-Copper-Oxide) as a new uncooled microbolometer material is evaluated for CMOS compatibility. By not requiring cryogenic cooling, the self-supporting semiconducting YBaCuO micromachined microbolometers have found an attractive application for thermal detection with substantial reduction in system cost, size, weight and power consumption as compared to cooled photon detectors. The lower thermal conductance of the microbolometers to the substrate provides good sensitivity for infrared detection. The CCBDI (Constant Current Buffered Direct Injection) readout circuit is designed to work with a traditional

frame rate of 30Hz and as a novel approach improves the performance of uncooled IR cameras by a higher frame rate of 200Hz for a 640x480 array for faster thermal imaging in commercial, military and biomedical applications. The 18-µm-long electrode arm geometry of YBaCuO microbolometer provides a higher frame rate of 200Hz and hence meets the design compatibility requirement for the faster 200Hz frame rate by the CCBDI readout circuit. The 75-µm-long electrode arm geometry is designed to achieve a traditional 30Hz frame rate. YBaCuO microbolometers based on self-supporting structure have been designed, fabricated, on-chip integrated and characterized as a novelty with the CCBDI readout circuit in AMI 1.5 µm double-poly-double-metal n-well 2.5V CMOS technology. The CCBDI readout circuit offers advantages of high linearity and uniformity, low offset error, provides maximum sensitivity at a bias current and has a great potential in the application of large uncooled bolometer focal plane arrays. The CCBDI readout is a better performance circuit as compared to other designs due to increase in the injection efficiency of the CCBDI amplifier and the stable detector bias control. The merits of YBaCuO include relatively high temperature coefficient of resistance (TCR), relatively low 1/f-noise, ease of fabrication by rf magnetron sputtering, room temperature operation and post-CMOS compatibility. The measured TCR is -3.16 %/K at 295K and measured value of thermal conductance is 1.01×10^{-7} W/K for a 30Hz frame rate. The maximum responsivity of 1.62×10^{5} V/W and maximum detectivity of 3.51×10^{7} $cmHz^{1/2}/W$ are measured of a single YBaCuO microbolometer pixel from the 4x4 array CCBDI readout circuit for a 200Hz frame rate, and hence confirm higher sensitivity.

TABLE OF CONTENTS

ACKNOWLEDGEMENTS.......... iv

ABSTRACT v

LIST OF ILLUSTRATIONS.......... x

LIST OF TABLES.......... xv

Chapter

1. INTRODUCTION.......... 1

1.1 Background.......... 1

1.2 Infrared Detector Array 2

1.3 CMOS Readout Circuit for Infrared Detectors 6

1.3.1 CMOS Readout Techniques 7

1.4 Outline of Dissertation.......... 17

2. BOLOMETERS.......... 19

2.1 Introduction.......... 19

2.2 Infrared Detectors.......... 23

2.2.1 Photon Detectors.......... 23

2.2.2 Thermal Detectors 26

2.3 Microbolometers.......... 28

2.3.1 Basic Functionality 28

2.3.2 Microbolometer Materials 34

2.3.3 Microbolometer Noise.. 36

2.3.4 Microbolometer Figures of Merit……….............................. 39

2.4 Conclusions... 40

3. CCBDI READOUT CIRCUIT 42

3.1 Introduction... 42

3.2 CCBDI Amplifier……. 44

3.2.1 Constant Current (CC) Configuration 44

3.2.2 AC and DC Analysis 47

3.3 Unitcell CCBDI Readout Circuit.. 49

3.3.1 Functional Unit Blocks 50

3.3.2 DC and Transient Analysis 54

3.4 4x4 Array CCBDI Readout Circuit 56

3.4.1 Functional Unit Blocks.. 56

3.4.2 DC and Transient Analysis... 59

3.5 Conclusions………... 61

4. CMOS TEST CIRCUITS …………….. 63

4.1 Characterization……... 63

4.1.1 CCBDI Amplifier 63

4.1.2 CMOS Inverter ……. 64

4.1.3 NMOS and PMOS Transistors 65

4.1.4 Micromachined Microbolometers…………………………… 66

4.2 Conclusions……….. 68

5. MICROBOLOMETER DESIGN AND FABRICATION………… 69

5.1 Introduction…………………………………………………………….. 69

5.2 Design and Fabrication…………... 70

5.3 Conclusions……….. 79

6. MICROBOLOMETER CHARACTERIZATION………………… 80

6.1 Introduction…………………………………………………………….. 80

6.2 Temperature Dependent Resistance (R(T)) and
Temperature Coefficient of Resistance (TCR) 81

6.3 Activation Energy (E_a) …….. 85

6.4 Current-Voltage (IV) Characteristic... 87

6.5 Thermal Conductance (G_{th})…… 89

6.6 Responsivity (R_v), Detectivity (D*) and
Thermal Time Constant (τ_{th})……….. 92

6.7 Conclusions………………………………………………………......... 109

7. SUMMARY AND CONCLUSIONS……... 117

REFERENCES 120

BIOGRAPHICAL INFORMATION.. 126

LIST OF ILLUSTRATIONS

Figure		Page
1.1	Thermal image obtained from an IR camera	3
1.2	Electromagnetic spectrum	5
1.3	CMOS readout circuit structure for the IR detector 4x4 FPAs	7
1.4	Constant bias readout circuit	9
1.5	Constant current readout circuit	9
1.6	Constant current with reference bolometer readout circuit	10
1.7	Source-follower per detector (SFD) readout circuit	11
1.8	Direct injection (DI) readout circuit	12
1.9	Gate modulation input (GMI) readout circuit	13
1.10	Buffered direct injection (BDI) readout circuit	14
1.11	Capacitive transimpedance amplifier (CTIA) readout circuit	16
1.12	Share-buffered direct injection (SBDI) readout circuit	17
2.1	The electrical circuit describing the operation of a bolometer. R_B and R_L denote the resistances of the bolometer and the load resistor respectively	20
2.2	Spectral exitance of a blackbody and graybody at 300 K	22
2.3	Schematic of the basic microbolometer operation circuit	29
3.1	Constant Current (CC) Configuration of the CCBDI amplifier	44
3.2	Schematic of the CCBDI Amplifier with biasing circuitry	45

3.3 AC analysis of the CCBDI Amplifier 47

3.4 DC analysis of the CCBDI Amplifier 48

3.5 Schematic and layout of the Unitcell CCBDI readout circuit 49

3.6 Schematic of the MBDI transistor and CCBDI Amplifier 51

3.7 Transient analysis of the integration capacitor and reset transistor/clock 52

3.8 DC analysis of the Unitcell CCBDI readout circuit 54

3.9 Plot of dV_{dt}/dR_{dt} versus bolometer resistance R_{dt} of the Unitcell CCBDI readout circuit 54

3.10 Transient analysis of the Unitcell CCBDI readout circuit for R_{dt} = 1.58 MΩ and R_{ref} = 1 MΩ 55

3.11 Schematic and layout of the 4x4 array CCBDI readout circuit 57

3.12 DC analysis of the 4x4 array CCBDI readout circuit 59

3.13 Transient analysis of the 4x4 array CCBDI readout circuit for Rdt = 1.58 MΩ, 1.68 MΩ, 1.78 MΩ, 1.88 MΩ and R_{ref} = 1 MΩ 60

4.1 DC transfer characteristic of the CCBDI Amplifier before and after fabrication 64

4.2 DC transfer characteristic of the CMOS inverter before and after fabrication 64

4.3 Current-voltage characteristic of three NMOS transistors before and after fabrication 65

4.4 Current-voltage characteristic of three PMOS transistors before and after fabrication 66

4.5 Current-voltage characteristic of four-micromachined YBaCuO test microbolometers for a 75-µm-long electrode arm geometry 67

5.1 (a) Cross-sectional view of a YBaCuO microbolometer. CoventorWare® model of the micromachined microbolometers showing (b) the 18-µm-long electrode arm geometry for a 200 Hz frame rate and (c) the 75-µm-long electrode arm geometry for a 30 Hz frame rate 71

5.2 (a) Fabrication started with the CMOS readout die bonded to silicon carrier wafer. (b) Aluminum deposition. Shown in a CoventorWare® schematic, a Unitcell, and a 4x4 array integrated with the CCBDI readout circuitry. (c) Sacrificial polyimide PI2737 coating and patterning for a 200 Hz frame rate shown for the same series of photos. (d) Titanium deposition and patterning to form the 18-µm-long electrode arms with the same series of photos 77

5.3 Microbolometer fabrication continued using a Coventorware® schematic, image of a Unitcell, and a 4x4 array integrated with the CCBDI readout circuitry. (a) Gold contact deposition and patterning. (b) YBaCuO thermometer deposition and patterning. (c) Sacrificial polyimide PI2737 ashing to complete the microbolometer fabrication process 78

5.4 SEM micrograph of fabricated YBaCuO microbolometers for the 75-µm-long electrode arm geometry for a 30 Hz frame rate with pixel size of 31x31 μm^2 (a) a portion of 4x4 microbolometer pixel array with the CCBDI readout circuit. (b) Closer view of the 4x4 array 79

6.1 Test YBaCuO micromachined microbolometers with pixel size of 31x31 μm^2 for characterization. (a) the 75-µm-long electrode arm geometry for a 30 Hz frame rate. (b) the 18-µm-long electrode arm geometry for a 200 Hz frame rate 81

6.2 Measurement set up for temperature dependent resistance R (T) and temperature coefficient of resistance TCR versus temperature 83

6.3 Resistance R (T) and TCR versus temperature range of 200 K to 325 K for the 75-µm-long electrode arm geometry for a 30 Hz frame rate 84

6.4 Resistance R (T) and TCR versus temperature range of 200 K to 325 K for the 18-µm-long electrode arm geometry for a 200 Hz frame rate 85

6.5 Plot of ln (Resistance) versus $1/k_BT$ plot showing activation energy (E_a) for the 75-µm-long electrode arm geometry for a 30 Hz frame rate 86

6.6 Plot of ln (Resistance) versus $1/k_BT$ plot showing activation energy (E_a) for the 18-µm-long electrode arm geometry for a 200 Hz frame rate............ 87

6.7 IV characteristic of test YBaCuO microbolometer for a 75-µm-long electrode arm geometry for a 30 Hz frame rate 88

6.8 IV characteristic of test YBaCuO microbolometer for a 18-µm-long electrode arm geometry for a 200 Hz frame rate 88

6.9 Resistance versus Power plot of test bolometer to find effective thermal conductance G_{eff} for the 75-µm-long electrode arm geometry for a 30 Hz frame rate.. 90

6.10 Resistance versus Power plot of test bolometer to find effective thermal conductance G_{eff} for the 18-µm-long electrode arm geometry for a 200 Hz frame rate 90

6.11 (a) Bonded packaged die of 0.5x0.5 cm^2 comprising self-supporting YBaCuO microbolometers fabricated and integrated with the CCBDI readout circuitry and test circuits. (b) Closer view of the bonded packaged die 92

6.12 Measurement set up for responsivity (R_v) and detectivity (D*) versus chopper frequency.. 94

6.13 Detector irradiance versus chopper frequency using Pyroelectric detector 95

6.14 DC transfer characteristic of a single YBaCuO microbolometer pixel with V_{DDA} = +0.5 V for the measured and simulated output from row 1 column 1 of the 4x4 array CCBDI readout circuit for a 200 Hz frame rate of the DEVICE200A1 96

6.15 Output voltage signal response versus frequency of IR radiation chopped at 5 Hz of a single YBaCuO microbolometer pixel from row 1 column 1 of the 4x4 array CCBDI readout circuit for a 200 Hz frame rate of the DEVICE200A1.. 97

6.16 Noise voltage signal response versus frequency of IR radiation chopped at 5 Hz of a single YBaCuO microbolometer pixel from row 1 column 1 of the 4x4 array CCBDI readout circuit for a 200 Hz frame rate of the DEVICE200A1 98

6.17 Responsivity and Detectivity versus chopper frequency biased as V_{DDA} = +1 V, V_{SSA} = -1 V of a single YBaCuO microbolometer pixel from row 1 column 1 of the 4x4 array CCBDI readout circuit for a 200 Hz frame rate of the DEVICE200A1 99

6.18 Responsivity and Detectivity versus chopper frequency using LP-2500 biased as V_{DDA} = +1 V, V_{SSA} = -1 V of a single YBaCuO microbolometer pixel from row 1 column 1 of the 4x4 array CCBDI readout circuit for a 200 Hz frame rate of the DEVICE200A1 101

6.19 Responsivity and Detectivity versus chopper frequency using LP-2500 biased as V_{DDA} = +1 V, V_{SSA} = -1 V (shown as 1V), and V_{DDA} = +0.5 V, V_{SSA} = -0.5 V (shown as 0.5V) of a single YBaCuO microbolometer pixel from row 1 column 1 of the 4x4 array CCBDI readout circuit for a 200 Hz frame rate of the DEVICE200A2 103

6.20 Responsivity and Detectivity versus chopper frequency using LP-2500 biased as V_{DDA} = +1 V, V_{SSA} = -1 V of a single YBaCuO microbolometer pixel from the Unitcell CCBDI readout circuit for a 200 Hz frame rate of the DEVICE200UC2 104

6.21 Responsivity and Detectivity versus chopper frequency using LP-2500 biased as V_{DDA} = +1 V, V_{SSA} = -1 V of a single YBaCuO microbolometer pixel from row 1 column 1 of the 4x4 array CCBDI readout circuit for a 30 Hz frame rate of the DEVICE30A3 106

6.22 Responsivity and Detectivity versus chopper frequency using LP-2500 biased as V_{DDA} = +1 V, V_{SSA} = -1 V of a single YBaCuO microbolometer pixel from the Unitcell CCBDI readout circuit for a 30 Hz frame rate of the DEVICE30UC3 107

6.23 Responsivity and Detectivity versus chopper frequency using LP-2500 biased as V_{DDA} = +2.5 V, V_{SSA} = -0.5 V of a single YBaCuO microbolometer pixel from row 1 column 3 of the 4x4 array CCBDI readout circuit for a 30 Hz frame rate of the DEVICE30A3.............. 108

LIST OF TABLES

Table Page

2.1 Comparison of the general properties of photon and thermal detectors 41

3.1 CCBDI Amplifier transistors sizes.. 46

3.2 Biasing of the CCBDI Amplifier 46

3.3 Performance analysis of the CCBDI Amplifier 48

6.1 Summary of results for the two different electrode arm geometries............... 110

6.2 Summary of results for the DEVICE200A1, DEVICE200A2 and DEVICE30A3 with V_{DDA}= +1 V, V_{SSA}= -1 V biasing 111

6.3 Summary of results for the DEVICE200A2 with V_{DDA}= +0.5 V, V_{SSA}= -0.5 V biasing.. 112

6.4 Summary of results for the DEVICE200UC2 and DEVICE30UC3 with V_{DDA}= +1 V, V_{SSA}= -1 V biasing.. 112

6.5 Summary of results for the DEVICE30UC3 with V_{DDA}= +2.5 V, V_{SSA}= -0.5 V biasing.. 113

6.6 Technical specifications of the three DRS's VO_x microbolometer models.... 115

6.7 Technical specifications of the three DEVICE200A1, DEVICE200A2 and DEVICE30A3 115

CHAPTER 1

INTRODUCTION

1.1 Background

The emergence of uncooled infrared (IR) detectors has welcomed new opportunities for IR detection both for military and civil applications. This dual-use technology has emphasized the integration of commercial and military IR imaging systems to meet the challenges of economic and defense.[1] This led to the research and development of commercial complementary metal-oxide-semiconductor (CMOS) very large scale integration (VLSI) technologies in the design of IR imaging systems. The merger of the rapid advancement in CMOS VLSI with the progress in the infrared focal plane arrays (IR FPA) technologies like detector material, sensing structure, readout electronics and image enhancement results in the revolution of IR image systems with significant performance improvement.[2] IR FPA offer wide range of military, medical, industrial and scientific applications, which requires high resolution and performance readout electronics. The resolution can be increased by increasing the number of pixels, however at the same time the size of pixels need to be reduced in order to decrease the overall chip area, its cost and also the cost of optics. There is always a tradeoff exists

between the requirement of high readout performance and the capacity to afford additional circuit complexity, chip area and power dissipation, while choosing the readout circuit to readout the microbolometer arrays. A high performance circuit should provide a stable detector bias to reduce the detector noise. It should have low input impedance to obtain high injection efficiency of the readout circuit for integrating maximum amount of current generated by the detector on the integration capacitor and for increasing its bandwidth and decreasing its input referred noise. The integration capacitor needs to be placed outside of the pixel to increase its value without increasing the pixel size. This research presents the amplifier structure known as buffered-direct-injection (BDI) incorporated with constant-current (CC) configuration to provide better performance in terms of injection efficiency and detector bias stability.

1.2 Infrared Detector Array

This research project is focused on the fabrication and on-chip integration of the infrared (IR) detector array of thermal type with the CCBDI readout circuit performed at cleanroom facility in NanoFAB center at the University of Texas at Arlington. The major advantage of this type of detector is room temperature operation and integration with a CMOS readout integrated circuit. The thermal detectors are uncooled infrared detectors such as microbolometers, micropyroelectrics and thermal piles. Thermal detectors, as uncooled infrared detectors, have emerged to replace cryogenically cooled infrared detectors in various applications hence eliminating the need for cryogenic cooling. This can result in substantial reduction in system cost, size, weight, power consumption and mission time because cryogens need not to be replenished. The

applications of thermal detectors are thermal imaging, for example surveillance purposes in military, night vision camera for security and policing, car industry, forest fire sensing and suppression, industrial applications like temperature monitoring and measurement, thermal imagery for firefighters, and medical imaging applications.

Thermal detectors are thermal imagers that create pictures of heat rather than light. They measure radiated infrared energy and convert the data to corresponding maps of temperatures. The thermal detector based instruments provide temperature data at each image pixel. Images may be digitized, stored, manipulated, processed and printed out. Fig. 1.1 below is a typical thermal or infrared image obtained from an IR camera showing three humans in total darkness.

Figure 1.1 Thermal image obtained from an IR camera.[3]

The thermal detector or IR imaging technology is based on the fact that any object whose temperature is above 0 K radiates infrared energy. The amount of radiated energy is a function of the temperature of the object and its relative efficiency of thermal radiation, known as emissivity. The fundamental operation is that the infrared energy emitted by a viewed scene is focused through the lens of an IR camera onto the

camera's detector or focal plane array (FPA). The FPA employs materials that respond by generating electrical impulses when infrared energy strikes them. These electrical impulses are then sent to a signal processor that converts them into video data for display on a monitor.

This research is focused on uncooled microbolometric IR detectors based on micromachining technology having higher temperature coefficient of resistance (TCR) than others. Extending from the visible light to microwave signals as shown in the electromagnetic spectrum (Fig. 1.2), the thermal detector arrays have wider wavelength response approximately from 0.7 μm to 1000 μm than the IR photon detectors,[4] limited only by the ability to absorb the incident radiation.[5,6,7,8,9]

In general, the IR FPA can be divided into two parts, the one would be the detector array and the other one is the readout circuit. In comparison to the conventional discrete design, the IR FPA has the inherent advantage of high packing density, low cost, reduced signal leads, high feasibility on-chip signal processing, and high flexibility for system integration.

Based on the micromachining technology, the thermal detector arrays can be monolithically manufactured by using a standard CMOS process with good uniformity and yield. Hence, thermal detector arrays can be on-chip integrated with signal readout circuit and signal processors. The thermal detectors are suitable for commercial as well as military applications due to the advantages of high integration capability, high yield, good uniformity, low noise and low cost.

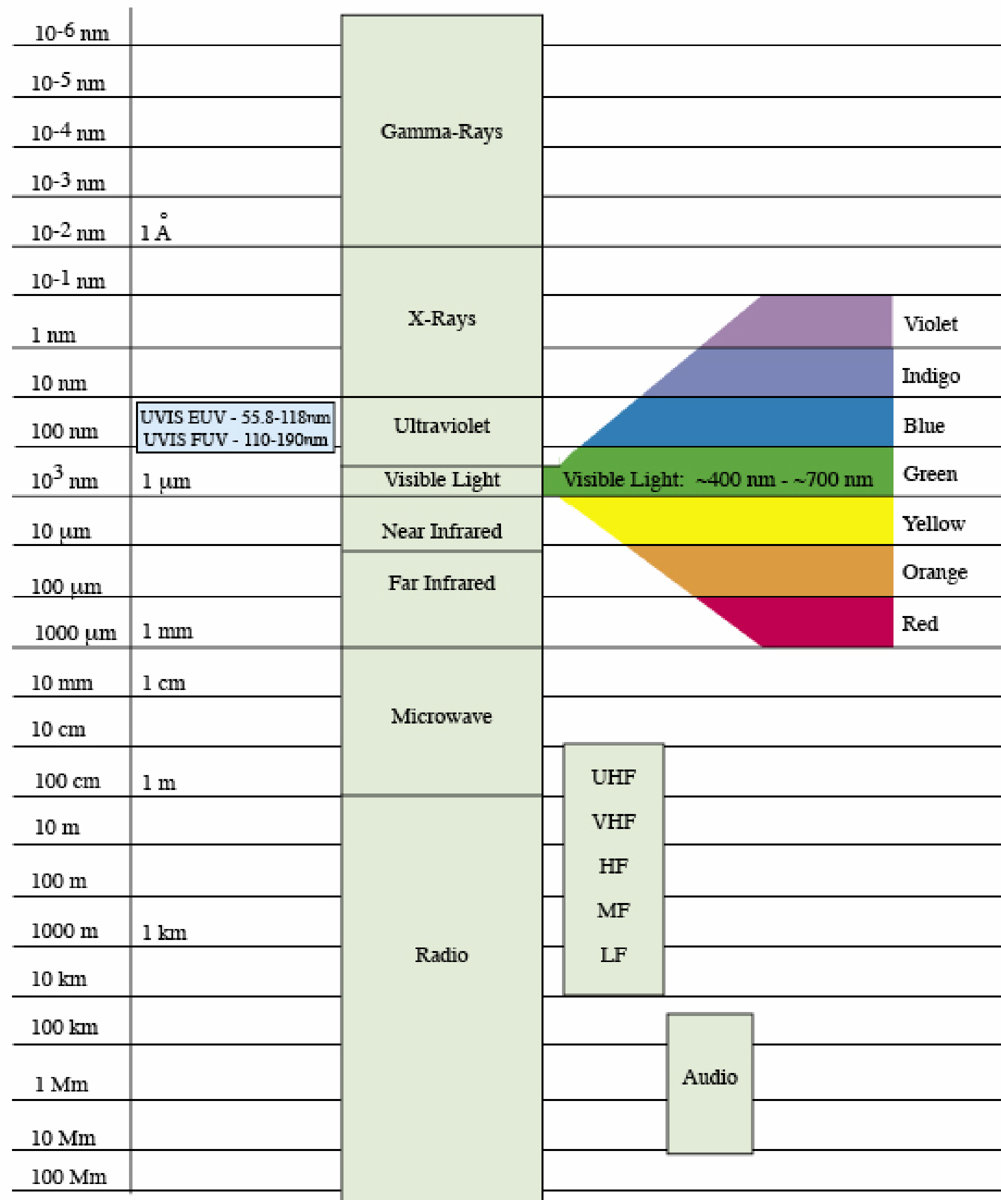

Figure 1.2 Electromagnetic spectrum.

1.3 CMOS Readout Circuit for Infrared Detectors

The self-supporting YBaCuO microbolometers[10] as IR detectors are integrated with the complementary metal-oxide-semiconductor (CMOS) readout circuit. This project will help improve the performance of uncooled IR cameras by higher frame rate of 200 Hz for a 640x480 array for faster thermal imaging in commercial, military and biomedical applications.

In the development of the IR detector Focal Plane Arrays (FPAs), the CMOS readout circuit is the second major part next to the fabrication of IR detector arrays. Fig. 1.3 shows a readout circuit topology, where CMOS readout circuit design includes multiplexing circuitry as row and column multiplexers to address the microbolometer array. The readout signals from the microbolometer pixels are amplified using a well defined CMOS readout circuit technique. This research is based on the CCBDI (Constant Current Buffered Direct Injection) readout circuit design technique. In this case there is a 4x4 pixel FPAs. The readout circuit is fabricated at a MOSIS foundry service in AMI 1.5 µm double-poly-double-metal n-well 2.5V CMOS technology.

The readout circuit serves as the substrate for the fabrication of the microbolometer arrays. The 2-D microbolometer arrays are fabricated on top of the readout circuit using a HD Microsystems polyimide sacrificial layer PI2737. Each microbolometer pixel represents the resistance. The change in the electrical property of the microbolometer pixel is amplified and finally readout as an output voltage. The microbolometer fabrication is performed at the NanoFAB Center at the University of Texas at Arlington, which contains comprehensive fabrication facilities

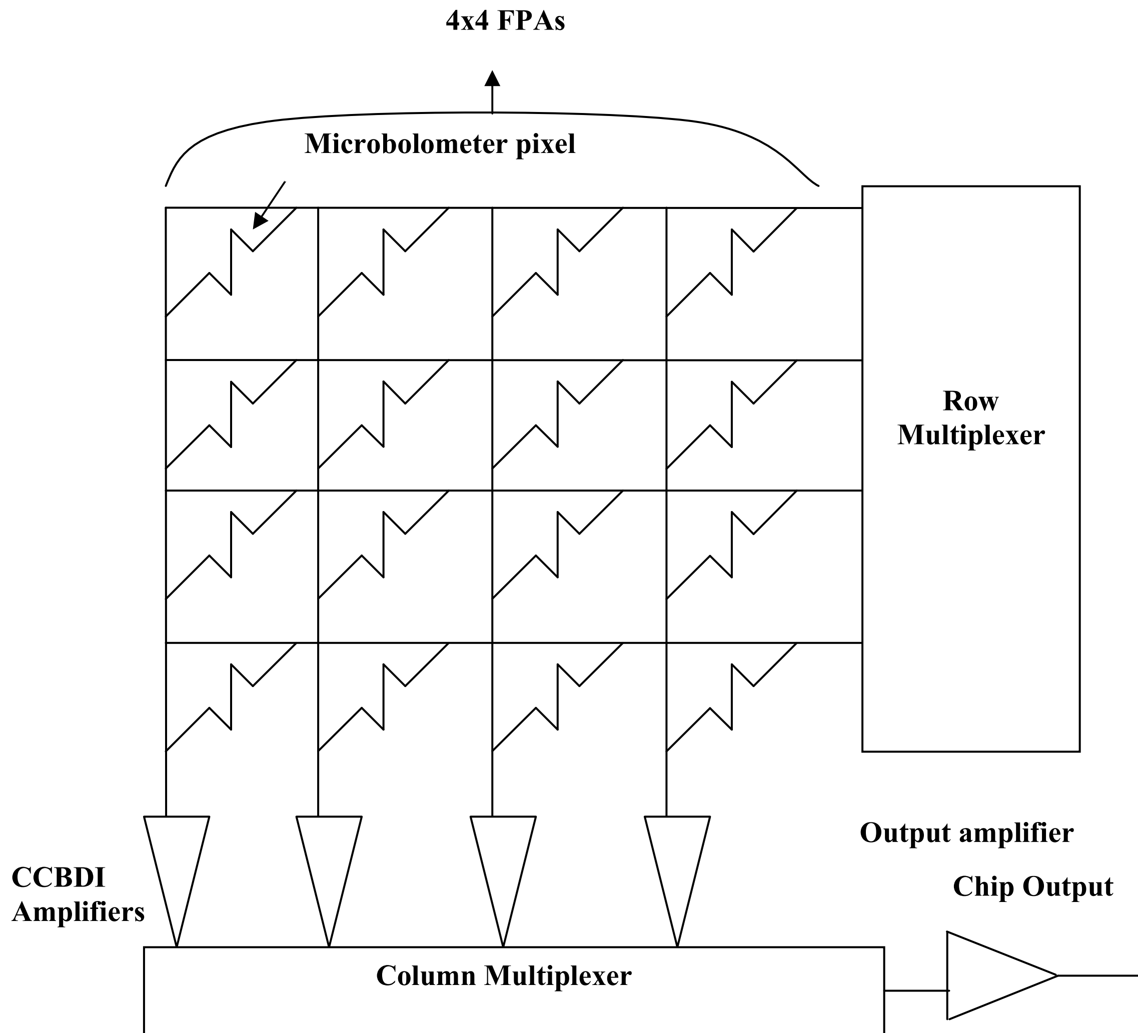

Figure 1.3 CMOS readout circuit structure for the IR detector 4x4 FPAs.

1.3.1 CMOS Readout Techniques

This section introduces the different readout techniques based on silicon CMOS VLSI technology. The two major factors that put limitations on the circuit design are area and complexity. Hence, generally the pixel pitch of IR FPAs is reduced with the increasing array size and resolution. Additionally, the total power dissipation of IR

FPAs is limited by the image system. The following describes the commonly used CMOS readout techniques with their state-of-the art structures. Generally, the readout circuits for uncooled bolometer IR detectors may be divided into three types, namely constant bias, constant current and constant current with reference bolometer. Some other simple readout circuits are used for diode readout, like source-follower per detector (SFD), direct injection (DI) and gate-modulation input (GMI) are commonly used in large staring IR FPAs. They have advantages of small pixel area and power consumption. Additionally, more complex readout techniques are used like buffered direct injection (BDI) and capacitive transimpedance amplifier (CTIA) which are developed to provide excellent bias control, high injection efficiency, linearity and noise performance. New readout technique such as share-buffered direct injection provides better compromise between pixel limitation and readout performance. This dissertation is focused on the constant current configuration (CC) incorporated with buffered direct injection (BDI), namely constant current buffered direct injection (CCBDI) readout circuit. CCBDI readout structure for the self-supporting semiconducting YBaCuO is discussed in detail in chapter 3.

1) *Constant Bias Readout*:

Fig. 1.4 shows the basic readout structure called the constant bias (CB) readout for the uncooled bolometer IR detectors. The readout structure shows the amplifier with the gain A having inputs as bolometer detector voltage V_D and V_{BS}. Select signal allows selection of a bolometer pixel from focal plane array to give the output readout voltage.

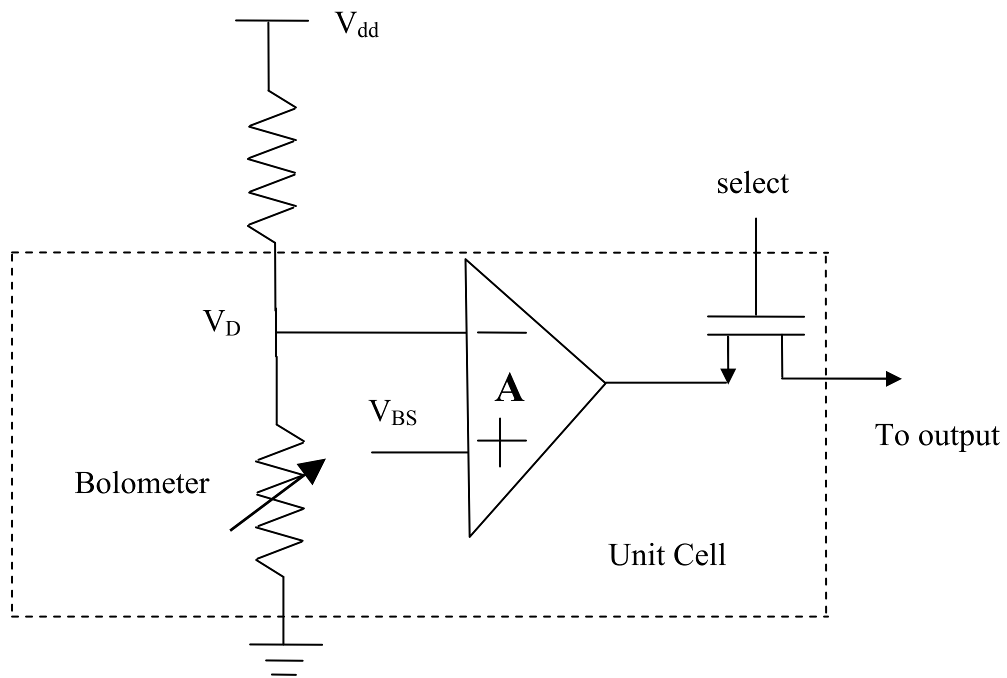

Figure 1.4 Constant bias readout circuit.

2) *Constant Current Readout*:

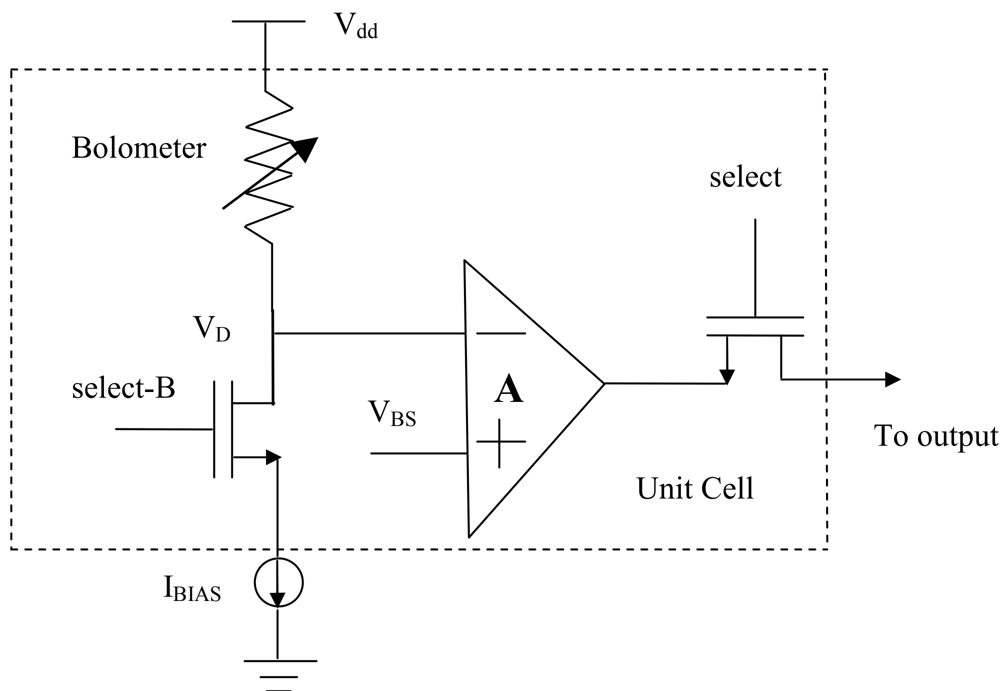

Figure 1.5 Constant current readout circuit.

Fig. 1.5 shows the basic readout structure called constant current (CC) readout for the uncooled bolometer IR detectors. In the CC configuration, the bias current I_{BIAS} is applied to the bolometer detector to generate the corresponding voltage on the resistor from the Ohm's law. The select-B signal controls the selection of the resistance variation of the bolometer resistor to be sensed as the node voltage V_D and then amplified by the amplifier with the gain A. Similarly the other select signal allows selection of a bolometer pixel from focal plane array to give the output readout voltage.

3) *Constant Current with Reference Bolometer Readout*:

Fig. 1.6 shows the basic readout structure called constant current with reference bolometer readout for the uncooled bolometer IR detectors.

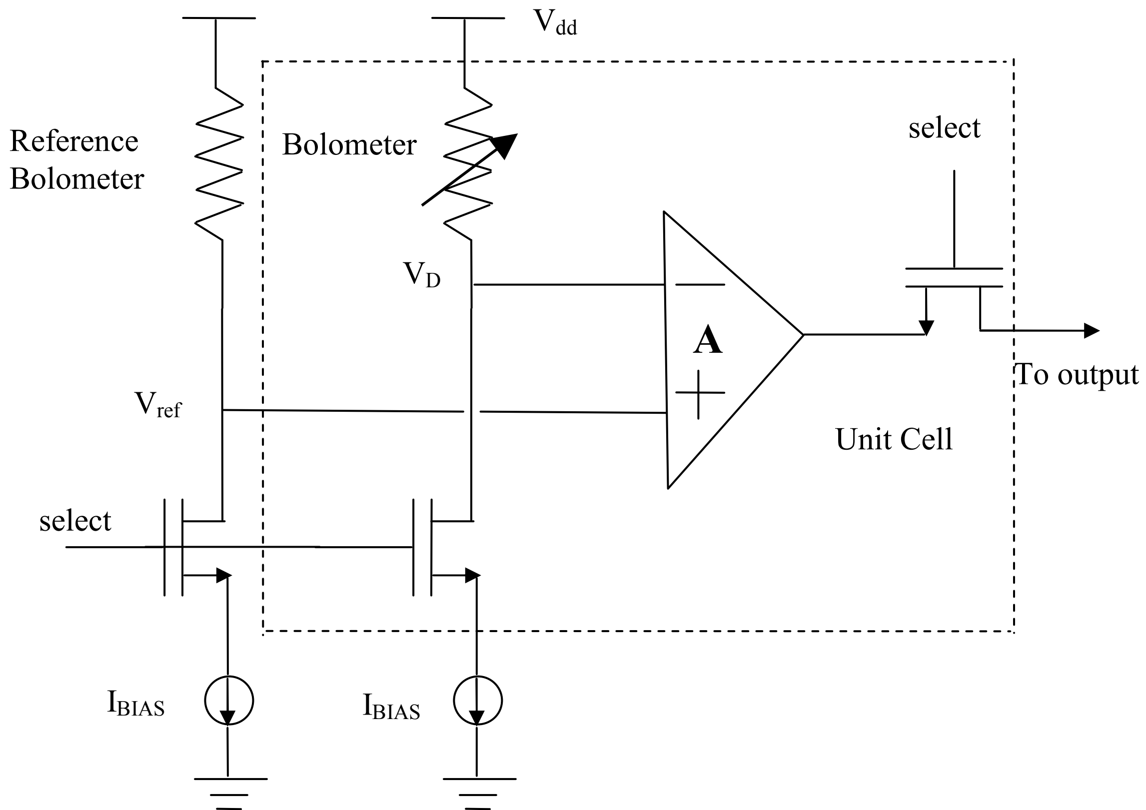

Figure 1.6 Constant current with reference bolometer readout circuit.

From Fig. 1.6, the reference bolometer resistor provides a fixed voltage V_{ref}. Any change in the bolometer resistor is sensed as voltage V_D with respect to the fixed voltage V_{ref} and is amplified by the amplifier with the gain A.

4) *Source-Follower Per Detector*[11,12]: Fig 1.7 shows a simple readout circuit called source-follower per detector (SFD). It utilizes NMOS source-follower (composed of MNI and MNL), a reset PMOS gate M-Rst, and a multiplexing NMOS device M-Sel used in each cell. The integration capacitance which is the summation of detector shunt capacitance $C_{detector}$ and input node capacitance of the SFD, is reset to high and then discharged by the photocurrent $I_{detector}$. The device M-Sel controlled by the clock Select samples the cell voltage signal serially to the output device. The simple structured SFD is suitable for the applications of high density, large format and low power IR FPA.

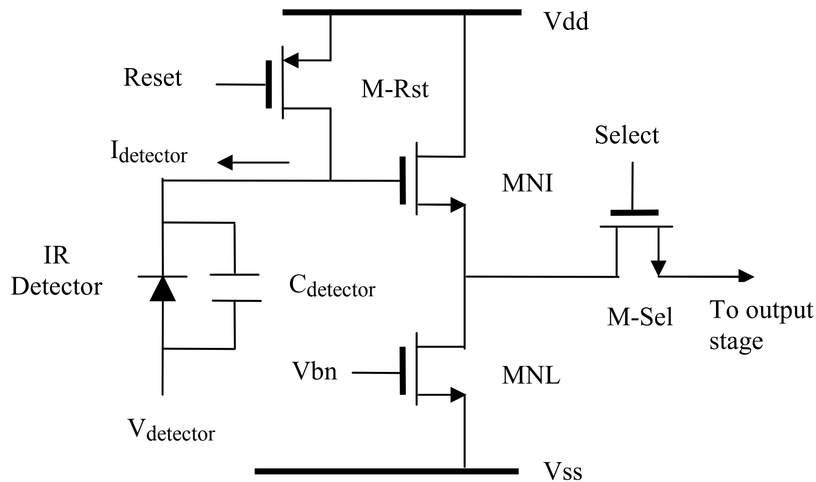

Figure 1.7 Source-follower per detector (SFD) readout circuit.

However, because of the photon excited carrier charges are directly integrated on the input node capacitance of the detector, the detector bias voltage changes through integration. Hence, it results in variations of detector characteristics and nonlinearity of

the readout circuit, and thus limiting the application of SFD. Also, the SFD is susceptible to KTC noise induced by the integration-and-reset function and fixed pattern noise caused by the process-dependent threshold voltage variations. The KTC noise is the integrated thermal noise appearing at the integration capacitor when the integrator's reset switch opens.[13]

5) *Direct Injection*[14,15,16]: Fig. 1.8 shows another simple readout circuit called the direct injection (DI). The common gate PMOS device M_{DI} is used to bias and sense the current of the IR detector. The detector current $I_{detector}$ passing though the gate M_{DI} is further integrated on the integration capacitor C_{int} which is reset by the NMOS device M-Rst. The PMOS source follower MPI and the multiplexing device M-Sel do the readout of the integrated voltage.

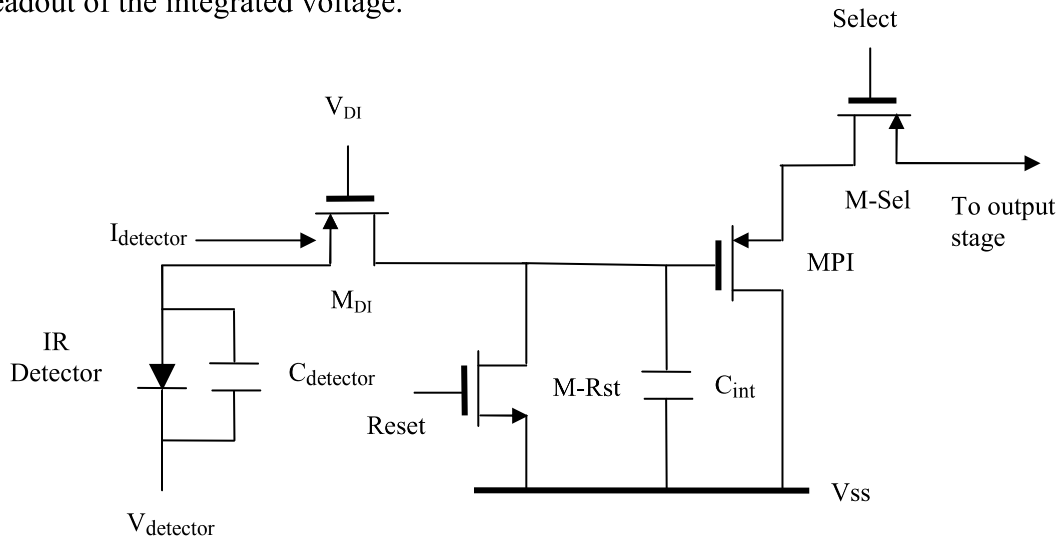

Figure 1.8 Direct injection (DI) readout circuit.

The common gate device offers a better bias control during integration than the SFD. DI has the similar simple structure and no active power dissipation, and hence making it suitable for high-density IR FPA applications. The injection efficiency is

defined as the ratio of the current flowing into the readout circuit to the detector current. The injection efficiency of the DI is determined by the ratio of detector shunt resistance to input resistance of M_{DI}. Therefore, lower input resistance means higher injection efficiency and better detectivity since the input resistance of PMOS device M_{DI} is proportional to its overall current including the background current level. Thus, DI is not suitable for the applications of low-background IR imaging readout. Moreover, a stable and low noise dc bias V_{DI} is needed in the DI circuit. Also, DI circuit suffers from both threshold voltage nonuniformity and KTC noise problems.

6) *Gate-Modulation Input*[11,17]: As shown in Fig. 1.9 the gate modulation input (GMI) readout circuit is comprised of current-mirror configuration with the tunable source V_{source} to control the current gain. The injection current is mirrored by the master device M_{load} and amplified by the slave device M_{input}. Then the amplified current is integrated on the integration capacitor C_{int} using the reset PMOS device M-Rst. The V_{source} is used as an adjustable bias to tune the current gain of the current mirror M_{load} and M_{input}.

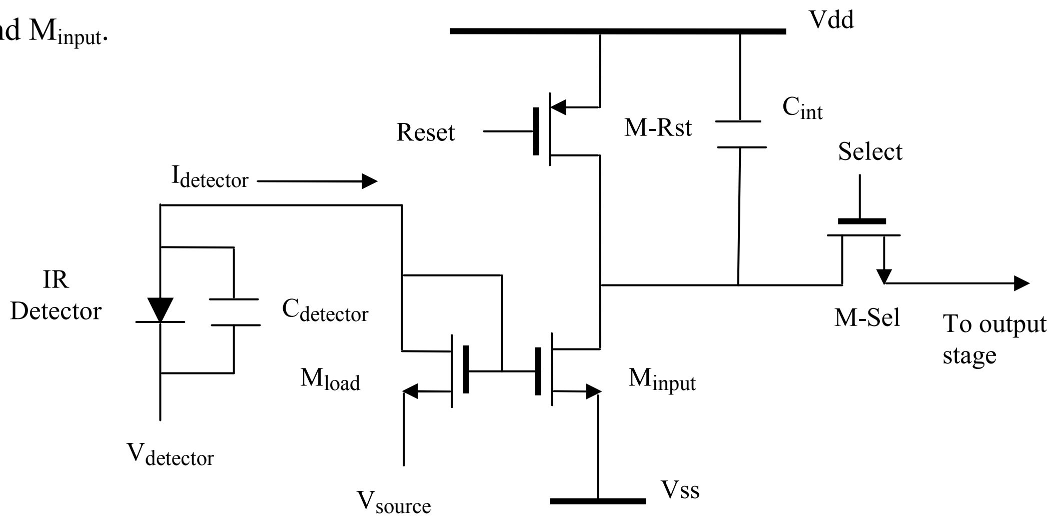

Figure 1.9 Gate modulation input (GMI) readout circuit.

The inherent current gain of the GMI results in higher detection sensitivity and reduced input referred noise as compared to DI. The current gain should be kept high and uniform to obtain a large total dynamic range (defined as the ratio of maximum charge capacity to noise floor), thereby resulting in strict requirements on MOSFET threshold voltage uniformity and dc bias stability of V_{source} which are difficult to be controlled.

7) *Buffered Direct Injection*[14,18]: The another readout circuit called the buffered direct injection (BDI) shown in Fig. 1.10 is similar to the DI except that an additional inverted gain –A is provided between gate node of the common-gate input transistor M_{BDI} and detector node. The BDI circuit is suitable for readout from the microbolometers and is thus designed as CCBDI readout circuit which is discussed in detail in chapter 3. The input impedance can be decreased by a factor of A due to the negative feedback structure. Hence, the injection efficiency is increased to near unity. The inverted gain stage can be implemented using a differential pair or inverter.

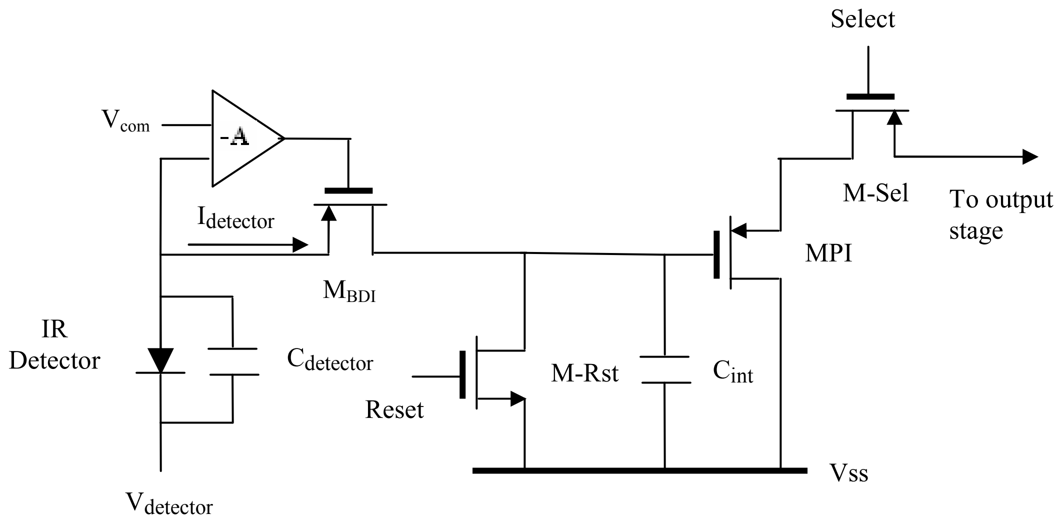

Figure 1.10 Buffered direct injection (BDI) readout circuit.

BDI increases the stability of detector bias control due to the virtual short property of gain-stage. Moreover, both equivalent input referred noise and operational bandwidth can also be improved in comparison to the DI. Since, the detector bias is controlled by the input voltage V_{com} of the differential pair instead of V_{DI} and gate-to-source voltage of M_{DI} in DI circuit, both the threshold voltage nonuniformity problem and strict low-noise bias requirement of the DI are resistant. The additional power loading, due to the gain stage consumption of active power, can be reduced by proper design of the gain stage with low bias current. The BDI is suitable for those applications which demand high readout performance and can afford additional complexity in circuit, chip area and power dissipation.

8) *Capacitive Transimpedance Amplifier*[19,20]: The schematic of the readout circuit called the capacitive transimpedance amplifier (CTIA) is shown in Fig. 1.11. The integration capacitor C_{int} is placed on the feedback loop of the amplifier with the reset device M-Rst . The reset device M-Rst is used to discharge the integration capacitor and to reset the amplifier output to reference voltage V_{com}. A good detector bias control is obtained by V_{com} through the virtual short feature of the amplifier. The Miller effect on the integration capacitor makes the capacitance extremely small to obtain low-noise and high-sensitivity performance. Unlike DI and BDI, the input resistance of the CTIA is independent of detector current. Also, the additional area and power consumption due to the inverted gain stage are needed in CTIA. The CTIA readout technique is suitable for readout application of the microbolometers.[21,22]

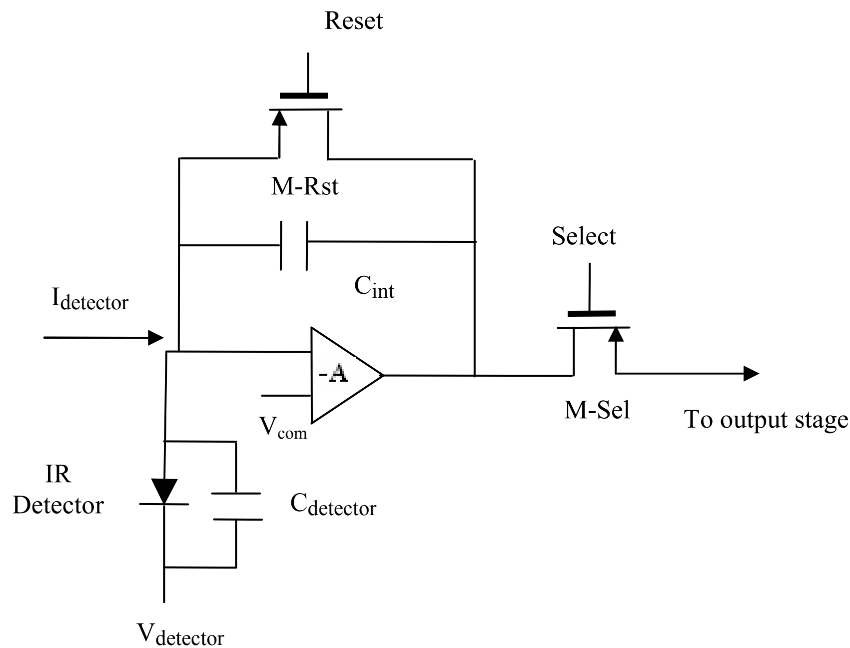

Figure 1.11 Capacitive transimpedance amplifier (CTIA) readout circuit.

9) *Share-Buffered Direct Injection*[23,24]: A newly improved readout circuit called share-buffered direct injection (SBDI) has been introduced as shown in Fig. 1.12. The gain stage in SBDI is implemented using differential pair with the shared half circuit techniques. The differential pair is comprised of the common left-half circuit Mb, MNS and MPS which is shared by all the cells in the same row and the two MOS devices MP and MN in each cell circuit. The source node of MP and the gate node of MN are biased by the shared half circuit through the global lines. Both the chip area and power consumption of the amplifier in SBDI can be reduced to nearly 50% of those in BDI and CTIA circuits.

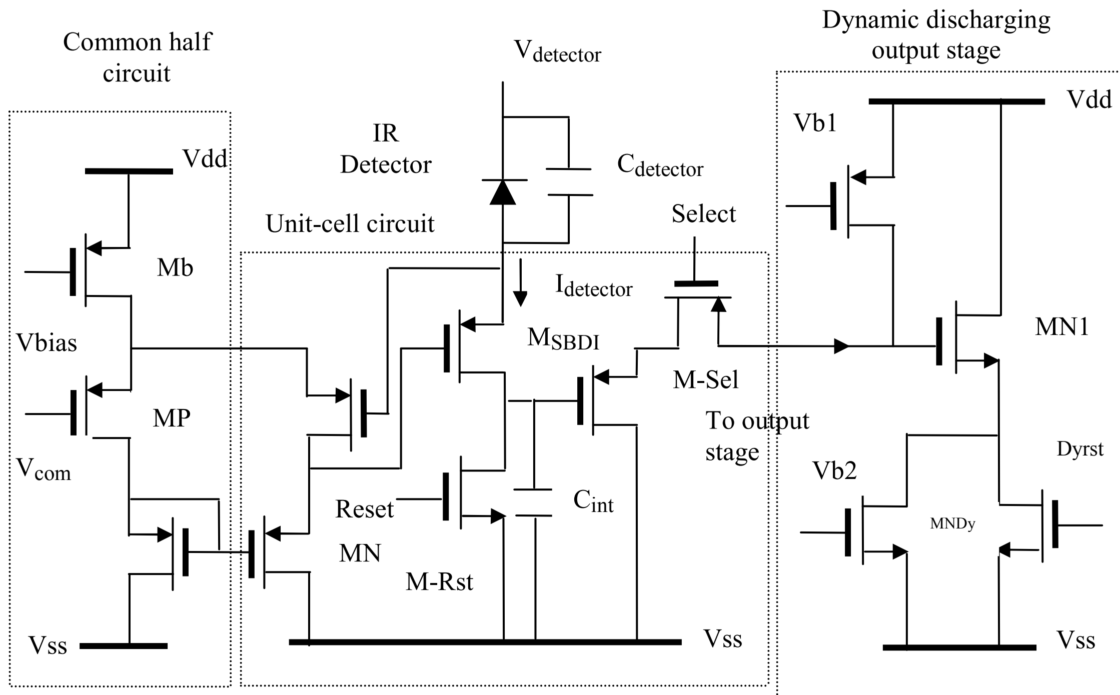

Figure 1.12 Share-buffered direct injection (SBDI) readout circuit.

The high injection efficiency, good detector bias control, threshold voltage variation immunity and low noise performance of the BDI circuit can be maintained in the SBDI. A dynamic discharging output stage is also introduced to save the static power dissipation and improve readout speed by applying a dynamic discharging gate MNDy and clock Dyrst. SBDI provides better tradeoff between circuit area, power consumption and circuit performance. Thus making it suitable for high density, large-array and high-performance applications in IR FPAs.

1.4 Outline of Dissertation

This document emphasizes the fabrication, integration and characterization of the micromachined microbolometer with the CCBDI readout circuit on a die which was fabricated from MOSIS. There were challenges associated with the fabrication process

and the solutions were created to the problems that arose in certain occasions throughout the fabrication process. This dissertation includes seven chapters:

1. The first chapter of this document provides general review of infrared detector array and CMOS readout circuit techniques.

2. The second chapter gives an introduction of infrared detector types, basic functionality of microbolometers, microbolometer materials, microbolometer noise, and microbolometer figures of merit.

3. The third chapter introduces CCBDI readout circuit, the CCBDI amplifier and AC & DC analysis. This is followed by description of the Unitcell and a 4x4 array CCBDI readout circuit, and the DC and transient analysis.

4. The fourth chapter provides the characterization of test circuits (fabricated by MOSIS foundry service on the die) before and after fabrication, e.g. CCBDI amplifier, CMOS Inverter, NMOS and PMOS Transistors, and Micromachined Microbolometers to verify YBaCuO microbolometer fabrication process is CMOS compatible.

5. The fifth chapter explains the design and fabrication process involved in the development of micromachined microbolometer integrated on top of the CCBDI readout circuit.

6. The sixth chapter presents the microbolometer characterization. This includes the measurement of figures of merit and the optical and thermal characterization carried out in the microsensors laboratory at NanoFab.

7. Finally, the seventh chapter summarizes the work done in this research project and the future work that can be investigated.

CHAPTER 2

BOLOMETERS

2.1 Introduction

A bolometer is a thermal detector whose resistance depends on its volume temperature. Fig 2.1 shows that the radiation of power P is allowed to incident onto the bolometer element. Since the resistance of the bolometer is heat sensitive, the radiation causes the heat change in the bolometer element and which in turn changes the value of the bolometer resistance $R_{B.}$ This in turn produces the variation in the output voltage V_{OUT}. The load resistor value of R_L is chosen to be the value corresponding to that of the bolometer. However, the load resistor is shielded from the incident radiation so that variations in the ambient temperature or of the bias V are automatically compensated in the output voltage. The absorption of radiation is converted into thermal energy and that determine the sensitivity of a bolometer. In addition, the response speed of a bolometer to changes in incident radiation is limited by the thermal time constant. In other words, the rate of heat transfer is an important factor in determining the response speed of the thermal detection process. The lower thermal mass of the bolometer detector will result in faster rate of heat transfer and hence lower thermal time constant.

At the time, when the radiation causes the bolometer element to be heated above the ambient, the temperature gradient drives the heat flow. Conduction and radiation are

the main heat flow mechanisms in the bolometer. However, the conduction mechanism of heat flow in the bolometer dominates.

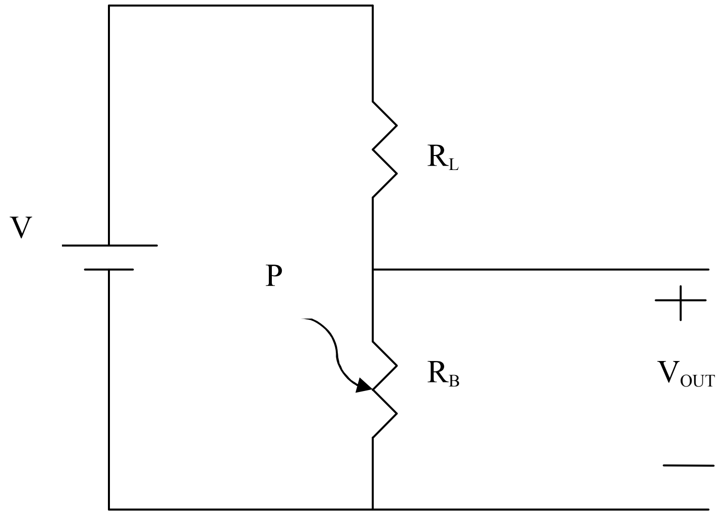

Figure 2.1 The electrical circuit describing the operation of a bolometer. R_B and R_L denote the resistances of the bolometer and the load resistor respectively.

During the case of radiation contributing to the major source of heat loss of the bolometer detector, the thermal conduction should be reduced. This is achieved by making a suspended detector separated from the substrate. This will not only reduce the thermal mass of the bolometer detector but also limit the heat loss from the detector. The self-supporting micromachined YBaCuO bolometer detector exhibits low thermal mass that in turn provides low thermal time constant for the same degree of thermal isolation. The heat loss of the bolometer depends upon the device geometry, which is typically the metal arms linking the detector to the bond pads. By appropriate selection of the arm material with low thermal conductance, geometry dimensions and the vacuum surrounding the detector will greatly help in reducing the thermal conductance of the bolometer.

All physical bodies emit radiation whose energy distribution, which is energy as a function of wavelength, depends on a large number of parameters of which the most important are the temperature of the body, its molecular composition and the state of its surface. The identification of many of the physical characteristics of a body is done by examining this electromagnetic radiation in wavelength ranges as ultraviolet, visible and infrared. For an infrared imager, the output signal is proportional to the energy received by the detector in its entire spectral sensitivity range. The amount of energy per unit area in the wavelength range between λ and λ+dλ, radiated from a surface at temperature T is given by Planck's equation and known as the spectral exitance given as

$$M_{e,\lambda}(\lambda,\mathrm{T}) = \frac{2hc^2}{\lambda^2\left[e^{hc/kT}-1\right]}\left[\frac{watt}{cm^2-\mu m}\right] \qquad (2.1)$$

where h is the Planck's constant ($6.62\text{x}10^{-34}$ Joule s), c is the speed of light, λ is the wavelength of the radiated signal, k is the Boltzmann's constant ($1.38\text{x}10^{-23}$ Joules/K), and T is absolute temperature.

The maximum of the radiated signal or exitance occurs at the wavelength when $\frac{\partial}{\partial\lambda}\left[\frac{\partial M_{e,\lambda}(\lambda,\mathrm{T})}{\partial \mathrm{T}}\right]=0$. Thus,

$$\lambda_{\max} = \frac{2898(\mu mK)}{T} \qquad (2.2)$$

This is called the Wien Displacement Law. For a blackbody source at 300 K, the maximum exitance occurs at approximately 9.7 μm (Fig. 2.2) which is the infrared region of the electromagnetic spectrum. This wavelength is targeted for the detector to detect and respond at room temperature.

The blackbody representing the perfect radiator and absorber is used as a standard to model a real radiation source or sink. The emission of radiation from a black body follows Planck's radiation law. The exitance of the graybody at any wavelength is a constant fraction called emissivity (ε) of the corresponding exitance of the blackbody. The emissivity depends on wavelength (λ) and temperature (T) and is give as

$$\varepsilon(\lambda, \mathrm{T}) = \frac{M_{e,\lambda}(\lambda, \mathrm{T})_{source}}{M_{e,\lambda}(\lambda, \mathrm{T})_{blackbody}} \tag{2.3}$$

Fig. 2.2 shows that the graybody and blackbody have spectrally the same shape. The total exitance for graybody at all wavelengths is

$$M^{gb}{}_{e}(\mathrm{T}) = \varepsilon \sigma_{e} \mathrm{T}^{4} \tag{2.4}$$

where σ_e is the Stefan-Boltzmann constant (5.67×10^{-12} Watt / $cm^2 K^4$).

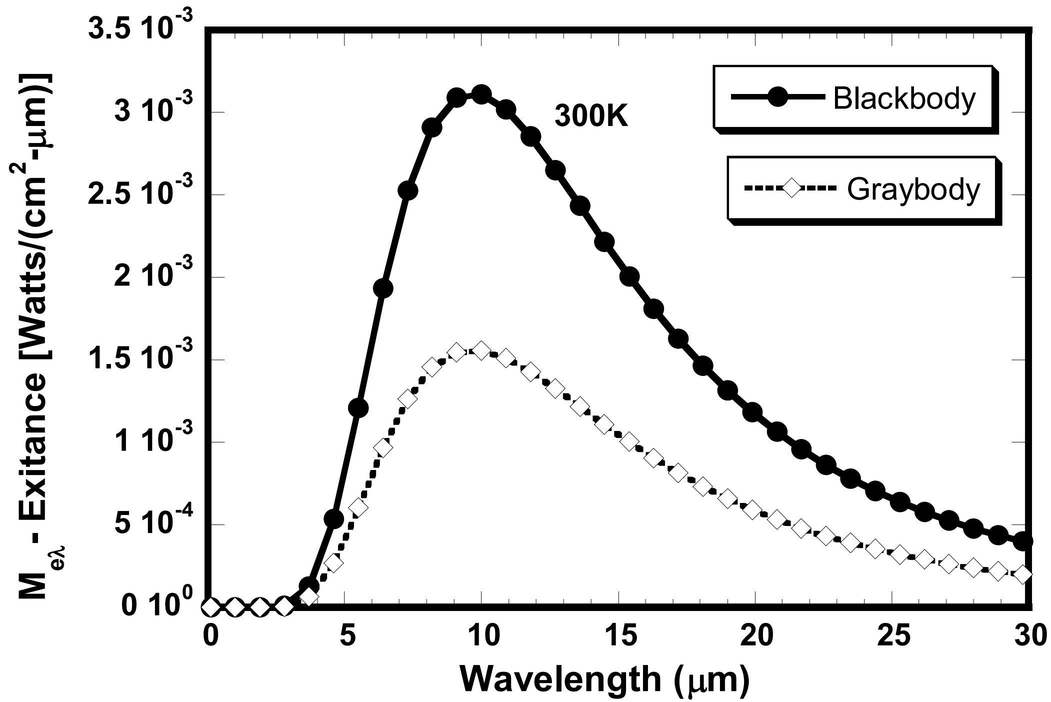

Figure 2.2 Spectral exitance of a blackbody and graybody at 300 K.[25]

Hence, emissivity can be described as a property of the surface characterizing how effectively the surface radiates compared to a blackbody. At a given wavelength, the emissivity power increases with increasing temperature and at shorter wavelengths more emissive energy appears as temperature is increased. Emissivity provides a parameter for use in the modeling of real source. A more complex real life model of a radiator or absorber is called selective radiator/absorber, where emissivity is a piecewise-constant function of wavelength for real models of source over a wider spectral range. The bolometer detector produces an IR image using the optical flux radiating from the various objects in the scene with different temperatures and their corresponding emissivity.

2.2 Infrared Detectors

Infrared detectors are classified as of two types, photon detectors and thermal detectors.

2.2.1 Photon Detectors

Photon or quantum detectors respond to incident radiation by generating photocarriers. The external photoelectric effect involves the emission of an electron from the surface of a metal and the internal photoelectric effect involves the production of an electron-hole pair in the interior of a semiconductor. Examples include photoconductive, photovoltaic and photoemissive solid-state detectors.[25] Photon detectors have a small bandwidth and are generally cooled to cryogenic temperatures in order to minimize the dark current and to maximize detectivity. Hence photon detectors incur more system cost and the complexity of device because of cryocooling, making

them applicable only in the highest performance military or civilian IR cameras. But in turn photon detectors have higher performance, with large detectivities and have very low time constant, hence smaller response times.

The function of photoconductive detectors is based on the photogeneration of charge carriers (electrons, holes or electron-hole pairs). These charge carriers increase the conductivity of the device material. Detector materials possible to utilize for photoconductive detectors are: mercury cadmium telluride (mercad, MCT, cut-off wavelength (λ_c) is 25 μm), lead sulfide (PbS, λ_c is 3 μm) and lead selenide (PbSe, λ_c is 5 μm).

Photovoltaic devices require an internal potential barrier with a built-in electric field for separating photo-generated electron-hole pair. Such potential barriers are created by the use of p-n junctions or Schottky barriers. The photovoltaic devices exhibit rectifying behavior, whereas the current-voltage characteristics of photoconductive devices are symmetric with respect to the polarity of the applied voltage. The examples of photovoltaic infrared detectors are indium antimonide (InSb, λ_c is 5.5 μm), mercury cadmium telluride (MCT), platinum silicide (PtSi, λ_c is 5 μm)-silicon Schottky barrier.

Photoemissive detectors operate with external photoelectron emission whereas the photoconductive and photovoltaic detectors operate with internal photoelectron emission. In photoemissive detectors, the excited electron physically leaves the detecting material and contributes to the external current flowing in the circuit. The examples of photoemissive detector are AgO:Cs (λ_c is 1.1 μm), Cs-Nag-K-Sb (λ_c is 0.9

μm) and GaAsP (λ_c is 0.9 μm).

Photon detectors can be further classified as intrinsic or extrinsic. When the photo-transition takes place across the fundamental band gap of the infrared sensitive material, then they are denoted as intrinsic. When the photo-transition takes place form impurity states to either of the valence or the conduction band. Since photon detectors require cooling due to the fact that dark current decreases with lower operating temperature. Also the dark current increases the larger of the cut-off wavelength of the detector (the largest wavelength at which the detector has a response). For constant cut-off wavelength and temperature, dark current is lower for intrinsic detectors than for extrinsic ones. Hence, the cooling requirements for intrinsic are less pronounced.

The photon detectors in most cases need to be cooled to the cryogenic temperatures like 77 K (liquid nitrogen) or 4 K (liquid helium). In some favorable cases thermoelectric cooling down to 200 K is sufficient for 3-5 μm wavelength mercury cadmium telluride ($Hg_{1-x}Cd_xTe$ for x=0.3, η is 65 %, λ_c is 5 μm and for x=0.2, η is 65 %, λ_c is 11 μm). Mercury cadmium telluride is mainly used in the field of photon detectors and to some extent indium antimonide is used. Mercury cadmium telluride or mercad (HgCdTe) is used both for the 3-5 μm (MWIR) and 8-12 μm (LWIR) atmospheric transmission window while indium antimonide (InSb) is used for the 3-5 μm. For the past few years, the low-dimensional structures based detectors are preferred for FPAs applications in LWIR region. These so called band-gap engineered detectors operate by electronic transitions between electronic states arising due to size quantization which is electron energy quantization because of small layer dimensions.

The three main materials of interest for IR detectors are: i) AlGaAs/GaAs quantum wells, ii) the strained SiGe/Si superlattices, and iii) the strained InAs/GaInSb superlattices. The AlGaAs/GaAs structure is named Quantum Well Infrared Photoconductive (QWIP). QWIP FPAs need to operate around 70-75 K to work properly and these temperatures are achieved by Stirling coolers. The main advantages of SiGe/Si quantum wells are the compatibility with silicon integrated circuit technology.

2.2.2 Thermal Detectors

A thermal detector converts incident radiation into heat, thus raising the temperature of some element of the detector. This change in temperature changes some temperature-dependent-parameter such as electrical conductivity and this change in parameter is then converted to an electrical or mechanical signal which in turn is amplified and displayed using CMOS readout circuit. As a thermal detector, larger conductivity in a bolometer detector ensures faster response but higher temperature change hence lowering the sensitivity. This makes a tradeoff on the structure design of the bolometer detectors. Thermal detectors have the desirable property that they are often capable of responding to a wide range of wavelengths without appreciable variations in sensitivity. Examples include bolometers, pyroelectrics, thermal piles and golay cell detectors.

Thermal detectors also known as uncooled IR detectors do not require cryogenic cooling which provides substantial reduction in system cost, weight, power consumption and mission time since the cryogens do not need to be replenished. The

major advantage of thermal detectors is that they can operate at room temperature. However, sensitivity is lower and the response time is longer than for photon detectors. Hence, this makes the thermal detectors suitable for focal plane array operation, where the later two properties are less critical. Thermal detectors are used in a large number of applications such as night vision, in transportation and the military, thermal imagery for firefighters, manufacturing, industrial nondestructive test and inspection, medicine, radiometry and spectroscopy applications in space sciences and medicine.[26, 27, 28, 29] Thermal detectors are often capable of operating over a large optical bandwidth and can be customized to detect in specific wavelength bands from visible up to 100 μm and beyond.A bolometer is basically a thermistor, containing a temperature dependent resistive material whose resistance changes with temperature. To obtain high sensitivity the temperature coefficient of resistance (TCR) should be as large as possible and the noise resulting from contacts and the material itself should be low. Resistive materials can be metals such as platinum or semiconductors. Metals have low noise but also have low TCR (about 0.2 %/K). On the other hand, semiconductors have high TCR (1-4 %/K) but are more susceptible to 1/f-noise. Semiconductors used for infrared detectors are amorphous, polycrystalline silicon, vanadium oxide and semiconducting Yttrium-Barium-Copper-Oxide (YBaCuO).

A pyroelectric detector is based on the fact that certain dielectric materials of low crystal symmetry exhibit spontaneous dielectric polarization. When the electric dipole moment depends on temperature the material is pyroelectric. Usually a capacitor is fabricated from the material and the change in the surface charge with temperature is

sensed. The pyroelectric material used for infrared detectors are TGS (tri-glycine sulphate), $LiTaO_3$ (lithium tantalate), PZT (lead zinconate titanate) and certain polymers. A dielectric bolometer makes use of pyroelectric materials operated in a way to detect the change of the dielectric constant with temperature. An example for this application is SBT (strontium barium titanate).

A thermal pile or thermocouple also called thermoelectric device is based on the presence of one or more several junctions between two materials. It is a proper connection of junctions used to develop a thermo-emk that changes with temperature, the so called Seebeck effect. To obtain high sensitivity the Seebeck coefficients should be as high as possible. Certain alloys containing antimony and bismuth have very high Seebeck coefficients of 150 μV/K. The CMOS compatible combination of aluminum/polycrystalline silicon gives 65 μV/K.

The Golay cell detector is based on the volume or pressure change of an encapsulated gas with temperature. The volume change is measured by the deflection of light rays resulting from the motion of properly positioned mirrors fastened to the walls of the gas container.

2.3 Microbolometers

A microbolometer is a thermal IR detector that detects the infrared radiations incident on the active region by the induced increase in the detector temperature[30].

2.3.1 Basic Functionality

The basic functionality or operation of the microbolometer is based on the change in the electrical resistance R of semiconductor materials as a function of

temperature T caused by the absorption of IR radiation. Fig. 2.3 shows the schematic of the basic microbolometer operation circuit.

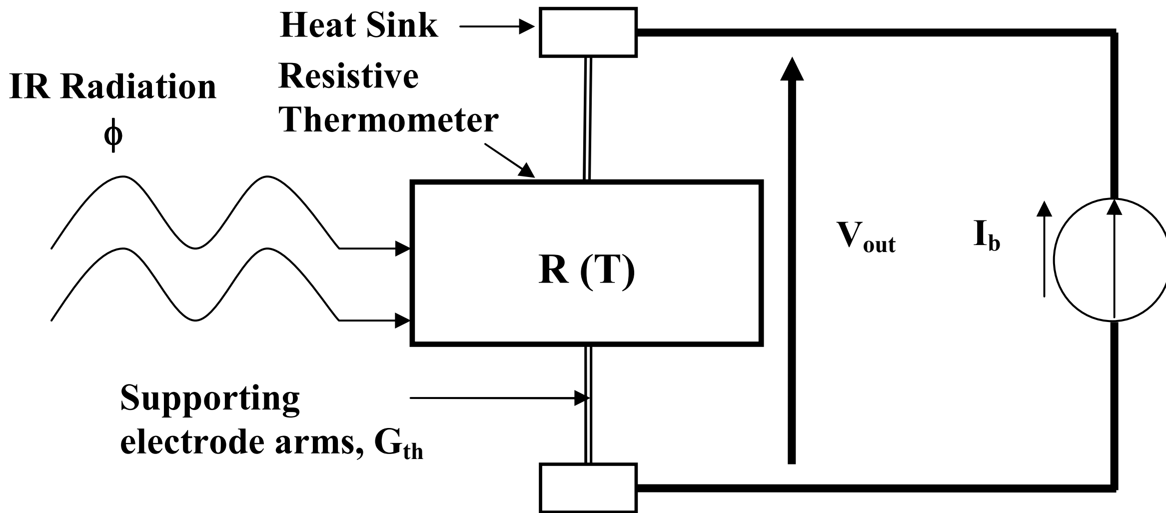

Figure 2.3 Schematic of the basic microbolometer operation circuit.

From the Ohm's law, after biasing the microbolometer with a constant dc current I_b, the output voltage V_{out} is measured which determines the change of resistance caused by the incident IR radiation. The resistive thermometer R(T) is connected to a heat sink through the electrode arms. Thermal conduction G_{th} occurs due to heat transfer through these electrode arms. Thus, the electrode arms should be optimized to reduce the thermal path between the thermometer and the substrate and to achieve the required thermal time constant and responsivity.

The electrical resistance of the semiconducting YBaCuO microbolometer obeys the following Arrhenius relationship

$$R(T) = R_0 \exp\left(\frac{E_a}{k_B T}\right) \tag{2.5}$$

where E_a is the activation energy. The activation energy corresponds to the energy between fixed state Fermi glass and the valence band which involves movement of holes to the valence band in p-type carrier semiconducting YBaCuO.

The thermodynamic interactions of the microbolometer detector with the surrounding atmosphere can be summarized as:

a) A fraction of incident radiation power P illuminated on the microbolometer is absorbed and produces the optical heating power P_{heat} with optical absorption efficiency η as shown as

$$P_{heat} = \eta P \tag{2.6}$$

b) The joule heating effect contributes to the heat loss from the microbolometer owing to the biasing current I_b that flows because of the electrical resistance R(T) of the microbolometer. The joule heating power due to current biasing is given as

$$P_I = I_b^2 R(T) \tag{2.7}$$

c) The heat exchange between the suspended microbolometer and the heat sink or the substrate through supporting electrode arms depends on the thermal conductance G_{th} of these arms. This heat exchange or transfer is shown as

$$P_{th} = G_{th}\left(T - T_{sub}\right) \tag{2.8}$$

where T is the microbolometer temperature and T_{sub} is temperature of the substrate. The thermal conductance of the electrode arm is determined as

$$G_{arm} = \frac{K_{arm} W_{arm} t_{arm}}{L_{arm}} \tag{2.9}$$

where K_{arm} is the thermal conductivity and W_{arm}, L_{arm} and t_{arm} are the corresponding width, length and the thickness of the arm. The effective length of the electrode arm is suspended above the substrate i.e. no thermal contact with the substrate. This dissertation project utilizes two different electrode arm geometries, one is 75-µm-long-electrode-arm geometry for 30 Hz frame rate and the other is 18-µm-long-electrode-arm geometry for 200 Hz frame rate.

For 75-µm-long-electrode-arm geometry, thermal conductance of the electrode arm is calculated as

$$G_{th} = 2G_{arm} = 2\frac{K_{arm}W_{arm}t_{arm}}{L_{arm}} = 2\frac{(0.219W/cmK)(5\times10^{-4}cm)(1\times10^{-5}cm)}{75\times10^{-4}cm} = 2.92\times10^{-7}W/K$$

For 18-µm-long-electrode-arm geometry, thermal conductance of the electrode arm is calculated as

$$G_{th} = 2G_{arm} = 2\frac{K_{arm}W_{arm}t_{arm}}{L_{arm}} = 2\frac{(0.219W/cmK)(5\times10^{-4}cm)(2\times10^{-5}cm)}{18\times10^{-4}cm} = 2.43\times10^{-6}W/K$$

The factor 2 is because there are two electrode arms suspending the microbolometer above the substrate.

d) The microbolometer radiates electromagnetic energy and hence loses optical power by radiation. This radiative power is expressed by Stefan-Boltzmann law as

$$M_{rad} = \varepsilon\sigma_e \mathrm{T}^4 \tag{2.10}$$

where σ_e is the Stefan-Boltzmann constant ($5.67\text{x}10^{-12}$ watt / cm^2 K^4).

The radiative conductance is given as

$$G_{rad} = 2A_d \frac{\partial M}{\partial T} = 8\eta A_d \sigma_e T^3 \tag{2.11}$$

For semiconducting YBaCuO microbolometer with A_d of 31x31 μm^2, η of 0.6 and T at 295K, the calculated value of G_{rad} is 6.72×10^{-9} W/ K.

e) The power balance equation for the microbolometer concerning heat transfer can be expressed as below

$$\frac{dQ}{dT} = P_{in} - P_{out} = \eta P + P_I + P_{sub} - P_{rad} - P_{th} \tag{2.12}$$

where Q is the thermal energy of the microbolometer, and P_{sub} is the radiated power from the substrate given as

$$P_{sub} = \varepsilon \sigma_e \mathrm{T}^4 \tag{2.13}$$

The heat capacity or thermal mass of the microbolometer is give as

$$C_{th} = \frac{dQ}{dT} = \frac{dQ}{dt}\frac{1}{\frac{dT}{dt}} \tag{2.14}$$

After substituting equations from (2.6)-(2.13), (2.12) is re-written as

$$C_{th}\frac{dT}{dt} = \eta P + I_b^2 R(T) - 2A_d \varepsilon \sigma_e (T^4 - T_{sub}^4) - G_{th}(T - T_{sub}) \tag{2.15}$$

Since microbolometer temperature increases by a small amount above room temperature Assuming $T=T_o + \Delta T$, Equation (2.15) can be simplified to

$$C_{th}\frac{d\Delta T}{dt} + (G_{th} + G_{rad} - \alpha P_I)\Delta T = \eta P + P_I \tag{2.16}$$

where α is the normalized rate of change of detector resistance called temperature coefficient of resistance (TCR).

The effective thermal conductance G_{eff} is defined as

$$G_{eff} = G_{th} + G_{rad} - \alpha P_I \tag{2.17}$$

Using equation (2.17), (2.16) becomes

$$C_{th} \frac{d\Delta T}{dt} + G_{eff} \Delta T = \eta P + P_I \tag{2.18}$$

The above equation expresses both the dc as well as ac component. The dc component is due to the dc bias of the microbolometer shown as

$$G_{eff} \Delta T_{dc} = P_I \tag{2.19}$$

where ΔT_{dc} is the temperature differential due to the power loss caused by current biasing and hence dissipating heat.

The ac component in (2.18) assumes a time varying signal exp($j\omega t$), where ω is the chopper frequency of the incident signal. Thus

$$C_{th}(j\omega \Delta T_{ac}) + G_{eff} \Delta T_{ac} = \eta P \tag{2.20}$$

where ΔT_{ac} is the temperature differential due to the power generated from the incident radiant power P.

$$\Rightarrow \Delta T_{ac} = \frac{\eta P}{G_{eff}\left(1 + j\omega \frac{C_{th}}{G_{eff}}\right)} \tag{2.21}$$

Equation (2.21) in magnitude is expressed as

$$\Delta T_{ac} = \frac{\eta P}{G_{eff}\sqrt{1 + (\omega \tau_{eff})^2}} \tag{2.22}$$

where $\tau_{eff} = \frac{C_{th}}{G_{eff}}$ is called the thermal time constant or thermal response time of the microbolometer, C_{th} is thermal mass of the device and G_{eff} is effective thermal conductance

Hence the values of thermal mass or heat capacity and thermal conductance are associated with microbolometers and determine the response time. Microbolometers or thermal detectors are typically slower responding devices because there thermal mass must experience a rise and fall in temperature, which is a slow process. Obviously, we want the largest temperature change per unit radiant power, which means a small thermal mass or well-isolated detector. In this case, the heat will not dissipate fast and therefore decay time is longer.

2.3.2 Microbolometer Materials

The microbolometer fabricated for this dissertation is semiconducting YBaCuO. Several stable phases are present in YBaCuO. The most widely used phase is called 123 phase, $YBa_2Cu_3O_{6+x}$. $YBa_2Cu_3O_{6+x}$ changes its conduction properties from a metallic ($0.5<x<1$) to a semiconducting ($0.3<x<0.5$) and to an insulating ($x<0.3$) by decreasing its O_2 molar content.[31,32,33] The semiconducting (oxygen-depleted) phase is generally used at room temperature as an uncooled IR detector. It has relatively high TCR, typically greater than -3 %/K at 290 K, relatively low 1/f-noise[10,34,35] and can be deposited by rf magnetron sputtering at ambient temperature from a single composite target.[32] Almasri et al.[36] reported the development of self-supporting semiconducting yttrium barium copper oxide (YBaCuO) microbolometers with low thermal mass.

YBaCuO microbolometer focal plane arrays with a noise equivalent temperature difference less than 100 mK have been demonstrated.[37] Besides lower operating cost and weight of the semiconducting YBaCuO due to lack of cooling cryogens, they have intrinsically better compatibility with the existing silicon-based processing and fabrication technologies. Ambient temperature deposition techniques are used for amorphous semiconducting YBaCuO since it does not require epitaxial growth as it is a mixed phase oxide. This makes the IR detectors built using semiconducting YBaCuO materials post CMOS compatible, enabling the IR sensitive pixels to be built on top of silicon-based readout circuitry for monolithic focal plane arrays and IR cameras.

The main characteristics of superconducting YBaCuO bolometers are that they operate near 90 K, where cooling is relatively inexpensive compared to liquid-helium cooled devices. These detectors come up with detectivity $D^* \sim 10^{10}$ cm $\sqrt{Hz}/W$ as they require epitaxial growth.

The thermal detectors are used commercially as thermal imagers.[25] The thermal imager system's function is to produce a picture that is map of temperature differences related to spatial flux and emissivity differences across an extended target.

VO_x is another thermistor material used extensively for development of bolometric detectors for thermal imaging.[38,39,40,41,42,43] Best known vanadium oxides are V_2O_3 and VO_2. They exhibit temperature induced crystallographic transformation with a reversible phase transformation from semiconductor (low-temperature) to metal (high-temperature). This results in material resistivity to diminish by two to three orders of magnitude. Thin films VO_2 are deposited by reactive sputtering system. It has a TCR of

-2 %/K at room temperature and a low 1/f noise. The deposition of VO_x results in high IR absorption.[44,45,46,47] The fabrication of microbolometers with VO_x is expensive because of narrow stability range of oxide. VO_x is a mixed phase oxide. Uncooled infrared microbolometer cameras based upon vanadium oxide[48] and amorphous silicon are currently commercially available.

Amorphous silicon (a:Si) is also used as a bolometric material.[49,50,51] It has a TCR of -2.8 %/K at room temperature.[52] The fabrication of a:Si employs high temperature annealing process to meet its high doping requirements. This is a disadvantage since it loses compatibility with post-CMOS. The flicker noise 1/f can be reduced from high temperature annealing process.

Poly-Si is another IR material. It is highly doped with arsenic, phosphorous or boron with high temperature annealing cyclic process. It obtains a stable physical structure[53,54] with a TCR of 1-2 %/K.

There is another bolometric material know as poly-Si-Ge alloy. Its electrical properties are similar to those of poly-Si and it is post-CMOS compatible. It has a TCR of -2 %/K including high 1/f noise. Reduced pressure chemical vapor deposition technique is used at temperature 600-700 ^{0}C for the material deposition.[55,56] It involves moderate doping of boron using ion implantation accompanied by high temperature annealing process.

2.3.3 Microbolometer Noise

Microbolometer noise is the random fluctuation in electrical output from detector. In order to determine the detectivity of the microbolometer detector, it is

necessary to define a noise mechanism. That is noise is the important parameter to determine the performance of the microbolometer. Different noise mechanisms of importance for assessing the ultimate performance of microbolometers include Johnson noise and 1/f-noise (which are called thermometer noise), the temperature fluctuation noise and the background noise.

Johnson noise also called as Nyquist noise is due to the thermal fluctuation caused by the charge carriers. The Johnson noise is inherent in the microbolometer and cannot be avoided. The Johnson noise voltage across a resistance R at temperature T is given by

$$\Delta V_j = \sqrt{4k_B TR\Delta f} \tag{2.23}$$

where k_B is the Boltzmann's constant and Δf is the frequency bandwidth over which noise is measured.

1/f-noise also called flicker noise is strong function of frequency and is observed at low frequencies . It mainly occurs due to surface-state traps that cause current flow to be interrupted by variations in the trapping time constant. It is always present because of the presence of the dc-bias current. The flicker noise power is approximately inversely proportional to the frequency[57]. It is given by

$$\Delta V_{1/f} = \sqrt{\frac{\alpha_H V_{dc}^2 \Delta f}{Nf}} \tag{2.24}$$

where α_H is the Hooge's coefficient, V_{dc} is the dc bias voltage due to dc-bias current across the microbolometer, Δf is the noise frequency bandwidth assumed small, N is the number of fluctuators in the sample and is volume dependent, and f is the input signal

optical modulation frequency. The factor α_H/N is determined empirically.

The temperature fluctuation noise arises from temperature fluctuations in the microbolometer detector. These fluctuations are caused by heat conductance variations between the detector and the surrounding substrate with which the detector element is in thermal contact. It is given by

$$\Delta V_{tf} = \frac{R_v \sqrt{4k_B T^2 G_{th} \Delta f}}{\eta} \tag{2.25}$$

where R_v is the voltage responsivity of the microbolometer detector, G_{th} is the thermal conductance and η is the optical absorption efficiency of the microbolometer material.

The background noise results from the radiative heat exchange between the microbolometer detector at temperature T and the surrounding environment at temperature T_b. It is given as

$$\Delta V_{bg} = \frac{R_v \sqrt{4k_B T^2 G_{rad} \Delta f}}{\eta} \tag{2.26}$$

where G_{rad} is the radiative conductance and is given as

$$G_{rad} = 4A_d \varepsilon \sigma_e (T^3 + T_b{}^3) \tag{2.27}$$

The total noise voltage is given by the sum of the squares of each noise contributions and is given by

$$\Delta V_n = \sqrt{\Delta V_J{}^2 + \Delta V_{1/f}^2 + \Delta V_{tf}^2 + \Delta V_{bg}^2} \tag{2.28}$$

2.3.4 Microbolometer Figures of Merit

Temperature Coefficient of Resistance (TCR) – It is the rate of change of resistance with respect to the change in temperature. The resistance decreases with increase in temperature.

$$TCR = \alpha = \frac{1}{R}\frac{dR}{dT} \tag{2.29}$$

Responsivity (R_v) - The responsivity of a detector is defined as the amount of output per watt of radiant optical power input. It is the ratio of voltage output to input light flux. The voltage responsivity of a microbolometer is given by[58]

$$R_V = \frac{I_b R \alpha \eta}{G_{eff}\sqrt{\left(1 + \omega^2 \tau_{th}^{\ 2}\right)}} \tag{2.30}$$

where I_b is the bias current, R is the bolometer resistance, α is the temperature coefficient of resistance, η is the absorptivity, G_{eff} is the effective thermal conductance, ω is the radiation modulation frequency, τ_{th} is the thermal time constant.

The thermal time constant $\tau_{th} = C_{th}/G_{eff}$, where C_{th} is thermal mass of the device. A low thermal mass allows for a short response time or time constant.

$$G_{eff} = G_{th} + G_{rad} - \alpha P_I \tag{2.31}$$

where G_{th} is the thermal conductance due to the microbolometer supporting structure and surrounding atmosphere, if any; G_{rad} is the radiative conductance and P_I is the power dissipated due to current biasing.

Detectivity (D^*) – The specific detectivity of an IR detector is the area normalized ratio of responsivity to the noise.

$$D^* = \frac{R_V \sqrt{A_d \Delta f}}{\Delta V_n} \tag{2.32}$$

where A_d is the area of the detector, Δf is the electrical bandwidth and ΔV_n is the total noise voltage measured over the bandwidth Δf.

Noise Equivalent Power (NEP) – is the rms incident radiant power necessary to produce a signal-to-noise ratio (SNR) equal to one. NEP is a minimum detectable power.

$$NEP = \frac{\Delta V_n}{R_V} \tag{2.33}$$

2.4 Conclusions

This chapter presents an introduction of infrared detector types, basic functionality of microbolometer, microbolometer materials, microbolometer noise, and microbolometer figures of merit.

The two main types of infrared detectors are discussed and compared: photon detectors and thermal detectors. Photon detectors have higher performance with large detectivities and fast response time but incur more system cost and the complexity of device because of cryocooling, making them applicable only in the highest performance military or civilian IR cameras. Thermal detectors do not require cryogenic cooling which provides substantial reduction in system cost, weight, power consumption and mission time. The major advantage of thermal detectors is that they can operate at room

temperature. However, sensitivity is lower and the response time is longer than for photon detectors. Tables 2.1 shows the comparison of the general properties of photon detectors and thermal detectors.

Table 2.1 Comparison of the general properties of photon and thermal detectors

	Photon Detector	Thermal Detector
Response time	Fast	Slow
Spectral responsivity	Narrow and selective	Wide and flat
Sensitivity	High	Low
Operating temperature	Cryogenic	Room
Cost	Expensive	Economical
System requirement	Cooling System	Temperature drift compensation
Crosstalk	High	Low
Noise	Low	High

The basic functionality of microbolometers is discussed including different materials used as detectors, various types of noise that exist in the microbolometer and finally the microbolometer figures of merit. The figures of merit includes temperature coefficient of resistance, responsivity, detectivity and noise equivalent power.

CHAPTER 3

CCBDI READOUT CIRCUIT

3.1 Introduction

The electronic chip used to multiplex or read out the signals from the detector element is called readout integrated circuit (ROIC). In other words, a readout circuit is designed to measure the resistance change caused by the incident IR radiation on the microbolometer. This dissertation presents the design and fabrication of readout integrated circuit using CCBDI (Constant Current Buffered Direct Injection) design technique in AMI 1.5µm double-poly-double-metal n-well 2.5V CMOS technology with the YBaCuO microbolometer pixel size of 31x31 μm^2. The CCBDI readout circuit is designed considering a few major factors, which include working with a traditional frame rate of 30 Hz and as a novel approach is designed to improve the performance of uncooled IR cameras by a higher frame rate of 200 Hz for a 640x480 array for faster thermal imaging in commercial, military and biomedical applications, and working out the design compatibility with the semiconducting YBaCuO microbolometer pixel array.

The semiconducting YBaCuO (Yttrium Barium Copper Oxide) microbolometers based on self-supporting structure are on-chip fabricated and integrated for the first time as a novelty with the CCBDI readout circuit. The design to produce the required features is implemented using the 18-µm-long electrode arm geometry of the YBaCuO microbolometer, which provides a higher frame rate of 200 Hz and hence meets the

design compatibility requirement for the faster 200 Hz frame rate by CCBDI readout circuit. The lower thermal conductance of the microbolometers to the substrate provides good sensitivity for the infrared detection. The 75-μm-long electrode arm geometry of the YBaCuO microbolometer is designed to achieve a traditional 30 Hz frame rate. The CMOS readout circuits were fabricated through the MOSIS foundry service.[59]

CCBDI readout circuit provides advantages of high linearity and uniformity, low offset error. The constant current (CC) configuration incorporated with buffered direct injection (BDI) structure (discussed in 1.3.1) provides maximum sensitivity at a bias current and has a great potential in the application of large uncooled bolometric focal plane arrays (FPAs).[60,61] The CCBDI readout is a better performance circuit as compared to other designs due to increase in the injection efficiency of the CCBDI amplifier and the stable detector bias control. The input impedance can be decreased by a factor of CCBDI amplifier gain due to the negative feedback structure. Hence, the injection efficiency is increased to near unity. CCBDI structure increases the stability of detector bias control due to the virtual short property of gain-stage. The CCBDI is suitable for those applications which demand high readout performance and can afford additional complexity in circuit, chip area and power dissipation. CCBDI readout circuit senses the signal from the YBaCuO microbolometer array and multiplex the readout to a common output using row and column shift registers. The CCBDI amplifier outputs the detector voltage with respect to a fixed YBaCuO reference resistor voltage. The reference resistor suppresses the background current and provides temperature drift compensation

3.2 CCBDI Amplifier

3.2.1 Constant Current (CC) Configuration

The bias current I_B is applied to the YBaCuO microbolometer detector "R_{dt}" to generate voltage V_{dt} at the input of amplifier in the constant current (CC) configuration as shown in Fig. 3.1. If one node of the R_{dt} is connected to a fixed YBaCuO reference voltage V_{ref}, then the resistance variation of the detector can be sensed by the amplifier at output node voltage V_{out}. The YBaCuO reference resistor "R_{ref}" is provided to suppress any background current and to provide temperature drift compensation. Temperature drift compensation is achieved when the energy falling on the YBaCuO microbolometer due to variations in environmental temperature is compensated by the corresponding variations of the same on the YBaCuO reference resistor.

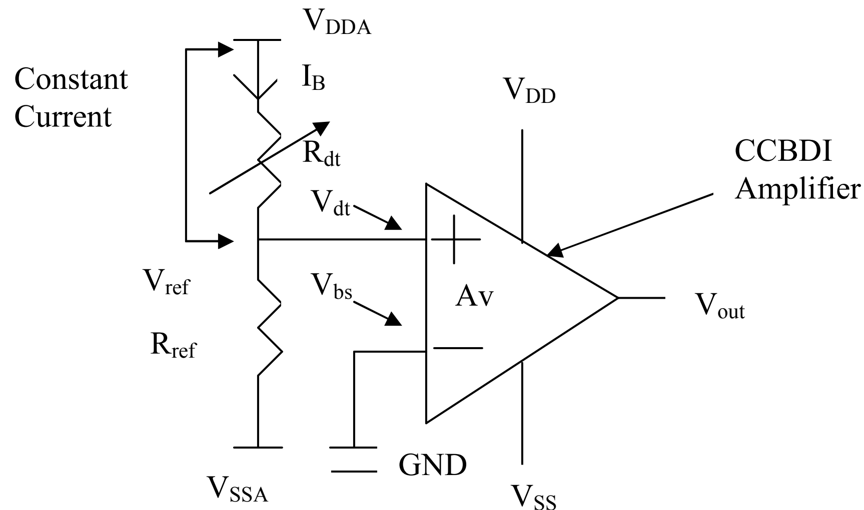

Figure 3.1 Constant Current (CC) Configuration of the CCBDI amplifier.

Constant current configuration provides the maximum sensitivity at the same bias current. The readout voltage difference is directly proportional to the resistance

difference so that linearity is high. The output of CC configuration is a voltage signal. Hence a transconductance amplifier is needed to convert the voltage signal into current. The schematic of the CCBDI Amplifier shown in Fig. 3.2 comprises simple differential-input-to-single-output amplifier as the transconductance amplifier GM AMP in Constant Current configuration and an operational amplifier OP AMP for Buffered Direct Injection.

GM AMP consists of 5 MOSFETs M1-M5 in differential-input-to-single-output configuration. OP AMP which is a complementary circuit to GMAMP has 5 MOSFETs M6-M10. The difference voltage ($V_{dt} - V_{bs}$) is amplified by the GM AMP and generates an output current.

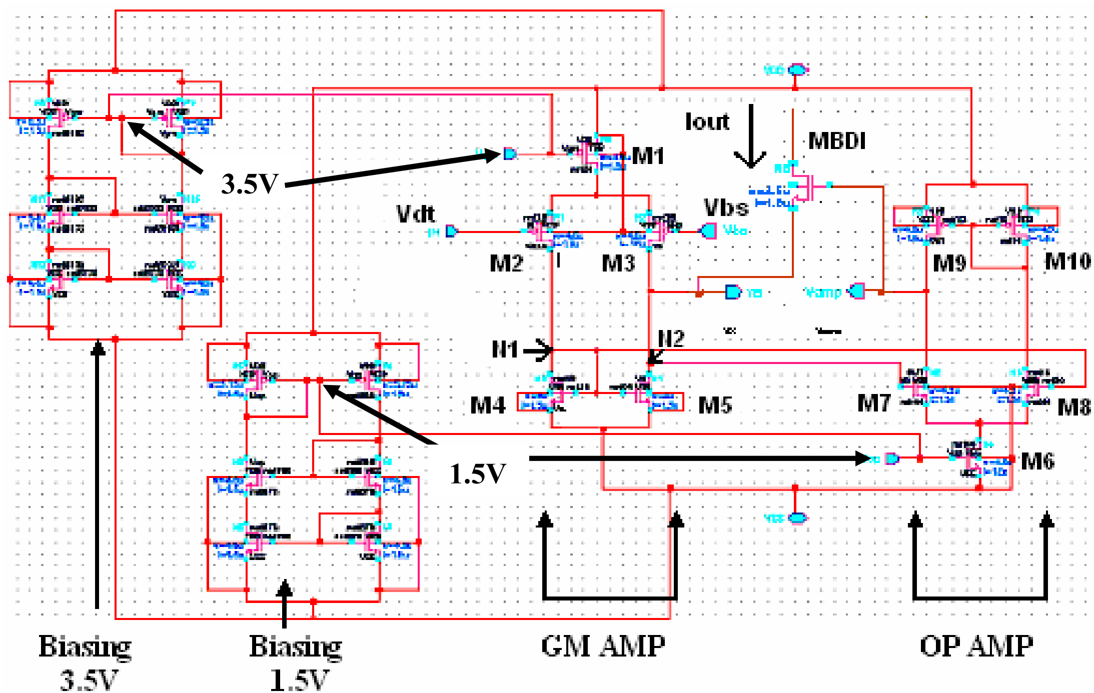

Figure 3.2 Schematic of the CCBDI Amplifier with biasing circuitry.

The OP AMP with negative feedback performs buffered direct injection providing lower output resistance for the output current of the GM AMP.

Table 3.1 shows the CCBDI Amplifier transistors channel width and length for AMI 1.5 µm technology. Biasing of the CCBDI amplifier is shown in Table 3.2.

Table 3.1 CCBDI Amplifier transistors sizes

DEVICE	TYPE	W(µm)	L(µm)
M1	PMOS	4.5	1.5
M2	PMOS	4.5	1.5
M3	PMOS	4.5	1.5
M4	NMOS	8	1.5
M5	NMOS	8	1.5
M6	NMOS	4.5	1.5
M7	NMOS	4.5	1.5
M8	NMOS	4.5	1.5
M9	PMOS	4.5	1.5
M10	PMOS	4.5	1.5

Table 3.2 Biasing of the CCBDI Amplifier

	POWER SUPPLIES	GM AMP	OP AMP
BIASING	V_{DD}=2.5V,V_{SS}=-2.5V	Biasing circuit used	Biasing circuit used

The CCBDI Amplifier Gain (Av) is calculated from the combination of the transconductance amplifier GM AMP gain ($Av_1 = g_{m1}.R_{out1}$) and the operational amplifier OP AMP gain ($Av_2 = g_{m2}.R_{out2}$). Where, g_{m1} and g_{m2} are the transconductance of MOSFETs M1 and M6 respectively given by

$$g_m = \frac{\partial I_D}{\partial V_{GS}} = \sqrt{2k_{n,p}\left(\frac{W}{L}\right)\frac{I_D}{2}} \tag{3.1}$$

where $k_{n,p}$ are the process parameters of NMOS and PMOS devices calculated as k_n of 70.84×10^{-6}A/V^2 and k_p of 25.94×10^{-6}A/V^2 values and I_D is the drain current of M1 and

M6. R_{out1} and R_{out2} are the corresponding output resistance of GM AMP (involving M2 and M4) and OP AMP (involving M8 and M10).

$$R_{out1} = \frac{1}{g_{ds2} + g_{ds4}} \; , R_{out2} = \frac{1}{g_{ds8} + g_{ds10}} \tag{3.2}$$

$$g_{ds} = \frac{\partial I_D}{\partial V_{DS}} = \frac{\lambda I_D}{2} \tag{3.3}$$

where $\lambda = 1/V_A$, V_A is the early voltage for MOSFETs.

Using MathCAD calculations, Av_1 is 9.28 and Av_2 is 17.59. Hence, the CCBDI Amplifier Gain Av, given by $Av_1 * Av_2$, is 163.19 (44.25 dB). A 0.39 μA of current is drawn from the CCBDI circuit with power dissipation of 1.95 μW.

3.2.2 AC and DC Analysis

Fig. 3.3 and Fig. 3.4 shows that the cadence simulations are performed with

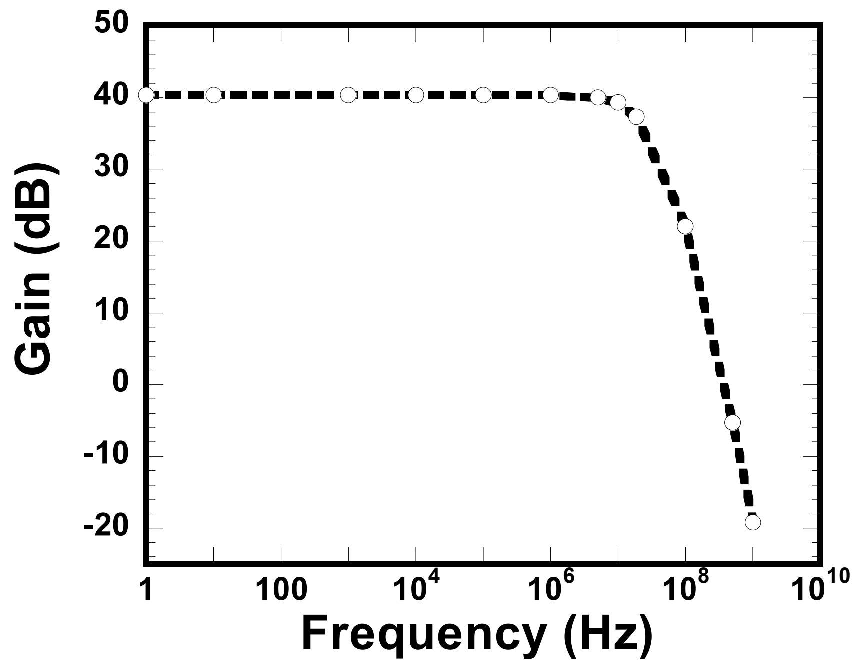

Figure 3.3 AC analysis of the CCBDI Amplifier.

model parameters taken from MOSIS's[59] T59L run for CCBDI amplifier's ac and dc analysis respectively. The ac analysis of the CCBDI amplifier describing the gain in dB versus frequency provides the performance analysis as shown in Table 3.3.

Table 3.3 Performance analysis of the CCBDI Amplifier

Low Frequency Gain	40 dB
Unity-gain Frequency	357 MHz
3-dB Frequency	18.7 MHz
Response Time	0.45 ns
DC offset	32 mV

The high frequency behavior of the amplifier plays a critical role as the gain begins to drop. The unity-gain frequency is the small-signal bandwidth of 357 MHz and the 3-dB frequency, $f_{3\text{-dB}}$ is obtained as 18.7 MHz for the CCBDI amplifier. The response time is calculated as 0.45 ns. The dc analysis of the CCBDI amplifier showing an inverting transfer characteristic offers a very low dc offset of 32 mV and hence

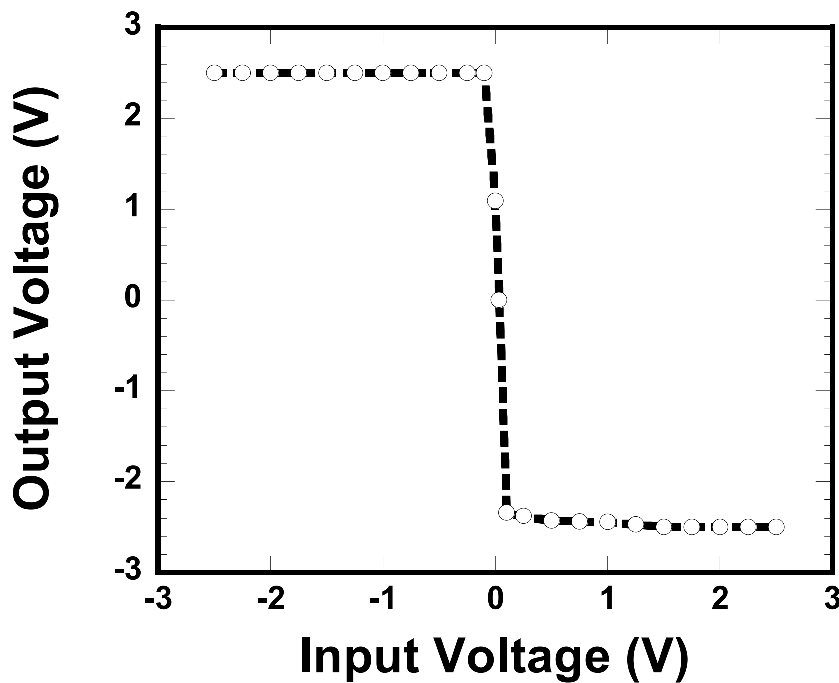

Figure 3.4 DC analysis of the CCBDI Amplifier.

provides a good output linear response.

3.3 Unitcell CCBDI Readout Circuit

The Unitcell determines a single YBaCuO microbolometer pixel with the cell size of 31x31 μm^2. The output of the Unitcell readout circuit is a single readout voltage obtained from the electrical characteristic of the single microbolometer pixel. The microbolometer is substituted with a resistance of an expected value in the schematic for simulation purpose. Fig. 3.5 shows the schematic and layout of the Unitcell CCBDI readout circuit presenting its functional unit blocks.

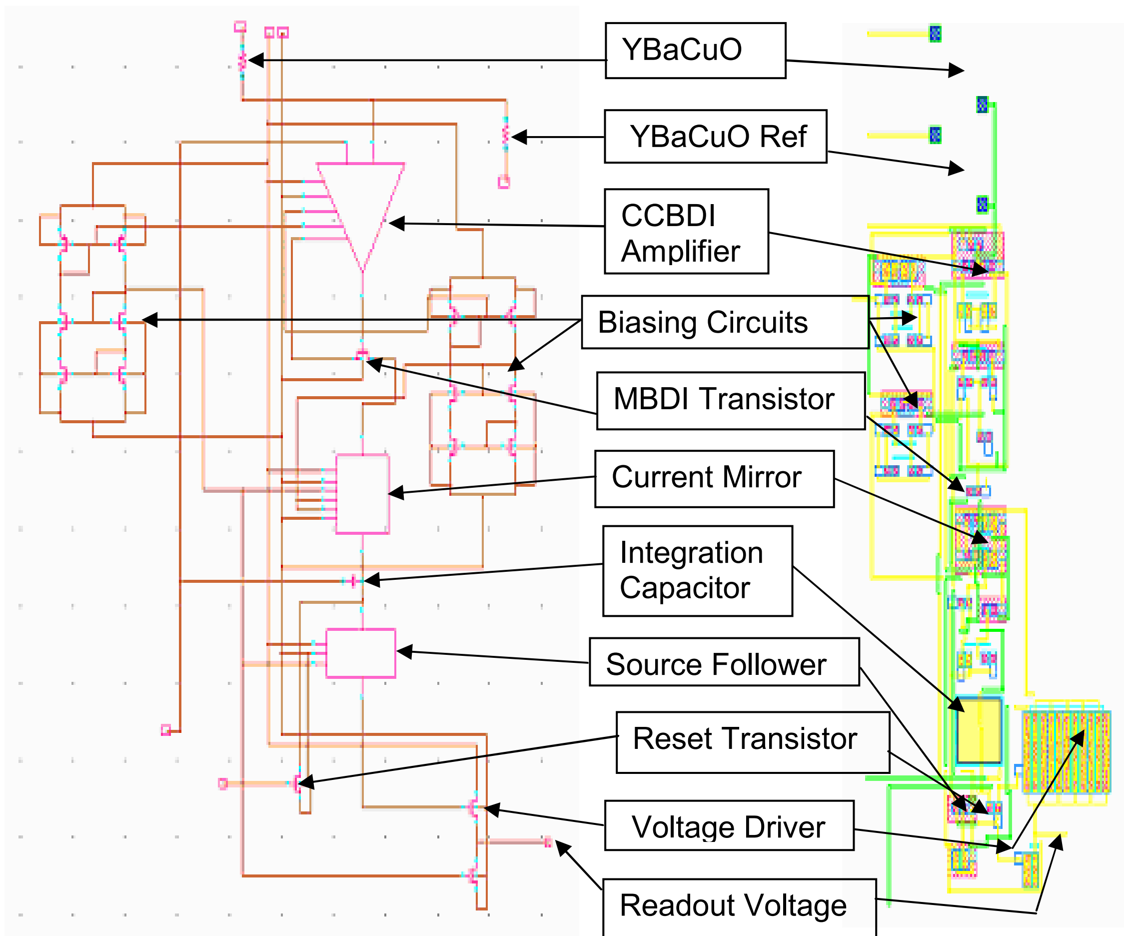

Figure 3.5 Schematic and layout of the Unitcell CCBDI readout circuit.

3.3.1 Functional Unit Blocks

The Unitcell CCBDI readout circuit is designed with the following functional unit blocks:

A. YBaCuO microbolometer and YBaCuO reference resistor in Constant Current (CC) configuration
B. CCBDI Amplifier
C. MBDI Transistor
D. Current Mirror
E. Integration Capacitor and Reset Transistor
F. Source Follower
G. Voltage Driver
H. Biasing Circuits

YBaCuO microbolometer and YBaCuO reference resistor in Constant Current (CC) configuration and CCBDI Amplifier are discussed previously in section 3.2.

C. MBDI Transistor

The two inputs to the OP AMP are connected to the GM AMP nodes N1 and N2 and the output of OP AMP is the input to MBDI Transistor as shown in Fig. 3.6. MBDI transistor forms a negative feedback path to CCBDI Amplifier. The nodes N1 and N2 are short due to the MBDI transistor and OPAMP connection. This makes the GM AMP perfectly symmetrical between left half M2, M4 and right half M3, M5 and hence causes improvement in the linearity and offset of CCBDI readout circuit. The negative feedback OP AMP with MBDI transistor does buffered direct injection and hence

providing a lower output resistance to the output current of GM AMP. BDI increases the stability of detector bias control due to the virtual short property of gain-stage (Av).[2] The MBDI is suitable for those applications which demand high readout performance and can afford additional complexity in circuit, chip area and power dissipation.

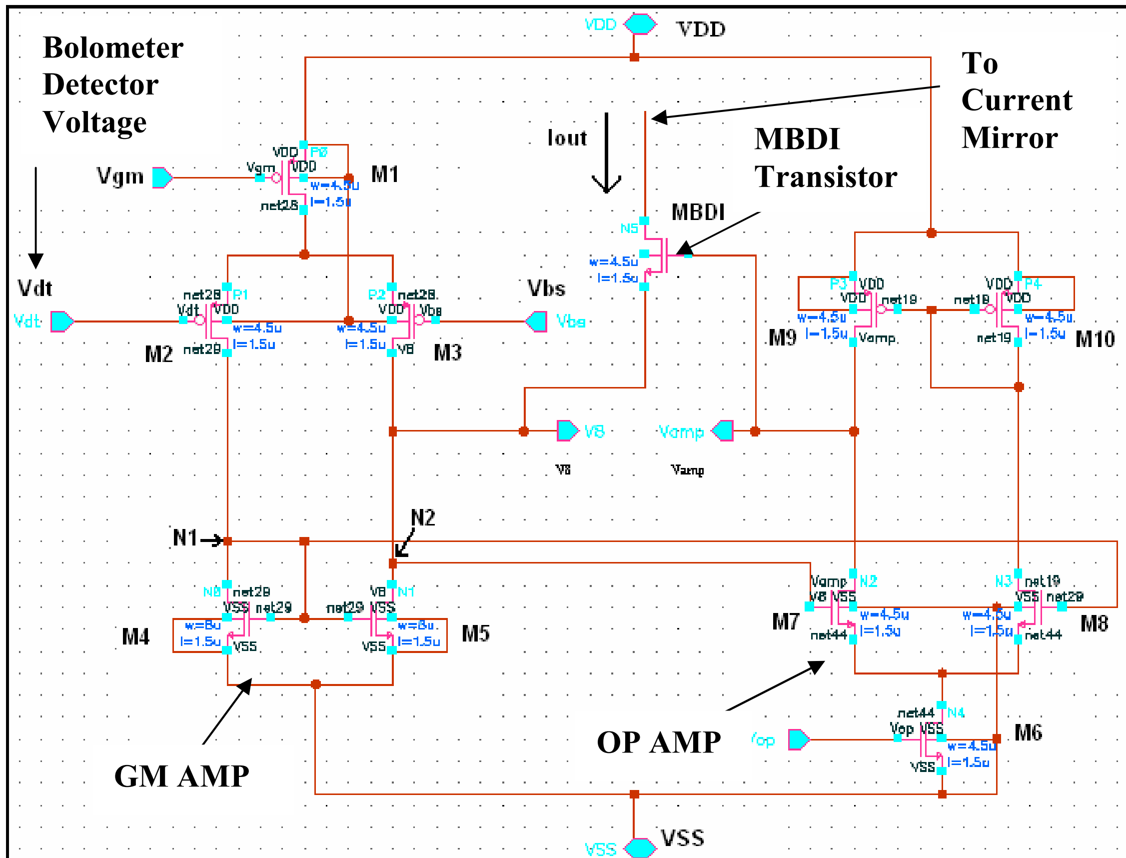

Figure 3.6 Schematic of the MBDI transistor and CCBDI Amplifier.

D. Current Mirror

Current Mirror comprises 4 MOSFETs. It changes the direction of the signal current and keeps the CCBDI stages away from the integration capacitor to increase the voltage swing. Hence provide more stable readout signal. The background suppression circuit also has 4 MOSFETs. It improves the poor uniformity of the current source which is caused by process variations in large chip area. The current source suppresses

the background signal. The readout circuit design underwent certain optimization involving an increase in the width of MOSFETS M1-M4. Increasing the widths of MOSFETS in current mirror carries out the advantages of faster charging/rise time of ~50ns as compared to previous design and hence faster readout output voltage response.

E. Integration Capacitor and Reset Transistor

After the amplification by the CCBDI amplifier, the detector current is further integrated on the integration capacitor C_{INT} which can be reset by the NMOS reset transistor. C_{INT} is 1pF. Fig 3.7 below shows the transient analysis of the integration capacitor and the reset transistor. The integration time of the readout circuit is determined by the saturation frequency of the integration capacitor C_{INT} and the microbolometer detector sensitivity. In Fig. 3.7, the integration time is approximately 17.4 ns.

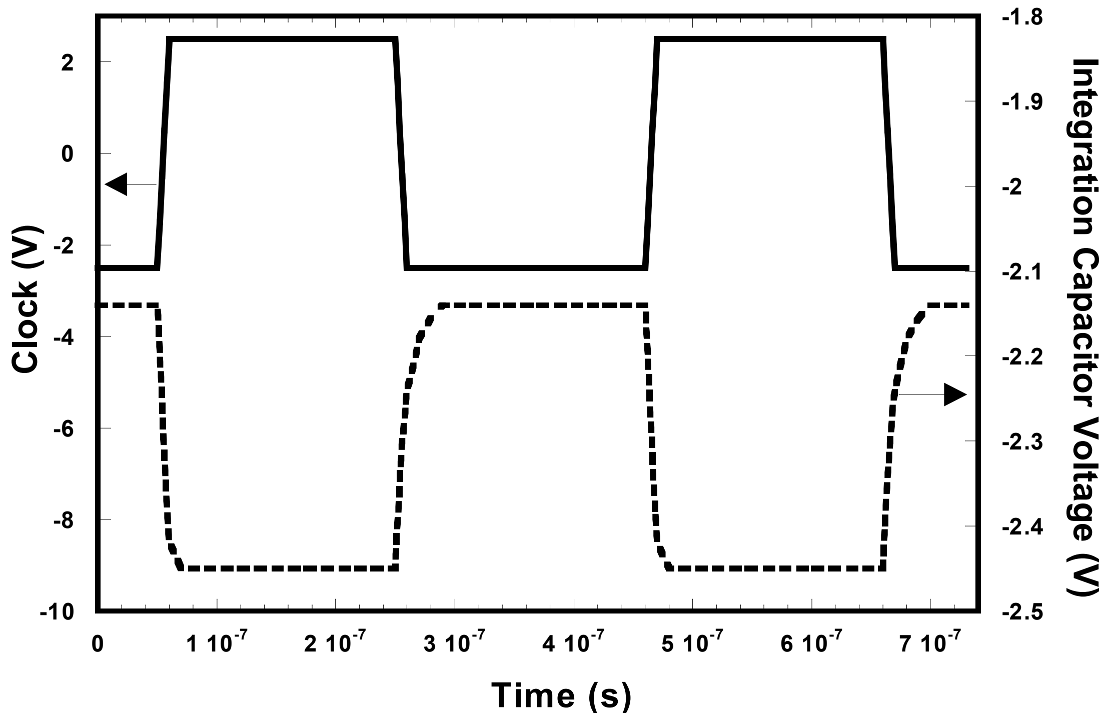

Figure 3.7 Transient analysis of the integration capacitor and reset transistor/clock.

The reset transistor performs the non-reset-to-zero operation to reset the integration capacitor. It also avoids the unstable current from the background suppression circuit. A clock pulse of +2.5 V to -2.5 V is used as an input to reset transistor.

F. Source Follower

Source follower acts as a voltage buffer to drive the load with negligible loss of signal level. It sends the voltage on the integration capacitor to the voltage driver. The source follower performs the level shift of integration capacitor voltage.

G. Voltage Driver

Voltage Driver is the output stage of CCBDI readout circuit for driving 30pF load. The voltage driver prevents any damage occurring to the readout circuit by dumping the excessive charge or current coming from large capacitive loads of bonding pads to the ground. It also allows the impedance matching to the transmission lines.

H. Biasing Circuits

Two types of voltage biasing circuits are designed to obtain following voltages for biasing CCBDI amplifier appropriately as shown in Fig. 3.2.

a) 3.5V to bias the GM AMP, b) 1.5V to bias the OP AMP.

The biasing circuits are designed from current source using active loads. By selecting the appropriate widths of active load transistors, the corresponding 3.5 V and 1.5 V of bias occur at the gate node of active load and are used to bias the GM AMP and OP AMP of the CCBDI amplifier respectively. A 103 μA of current is drawn from the 3.5V biasing circuit with power dissipation of 0.51 mW. 79 μA of current is drawn from the1.5V biasing circuit with power dissipation of 0.39 mW.

3.3.2 DC and Transient Analysis

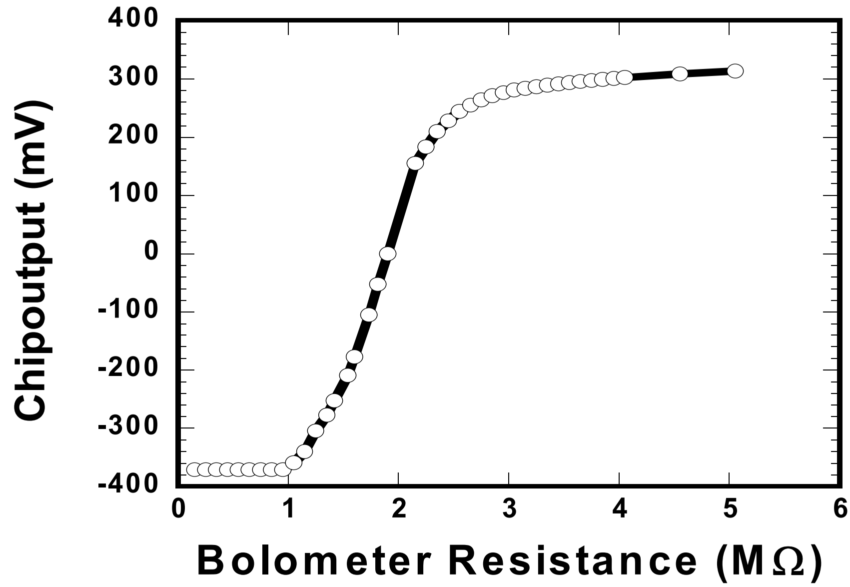

Figure 3.8 DC analysis of the Unitcell CCBDI readout circuit.

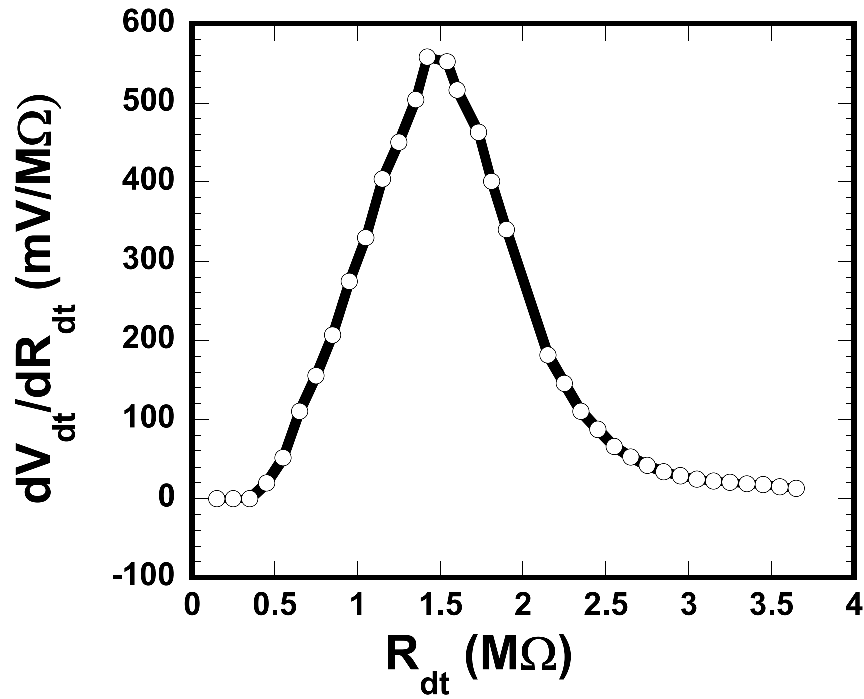

Figure 3.9 Plot of dV_{dt}/dR_{dt} versus bolometer resistance R_{dt} of the Unitcell CCBDI readout circuit.

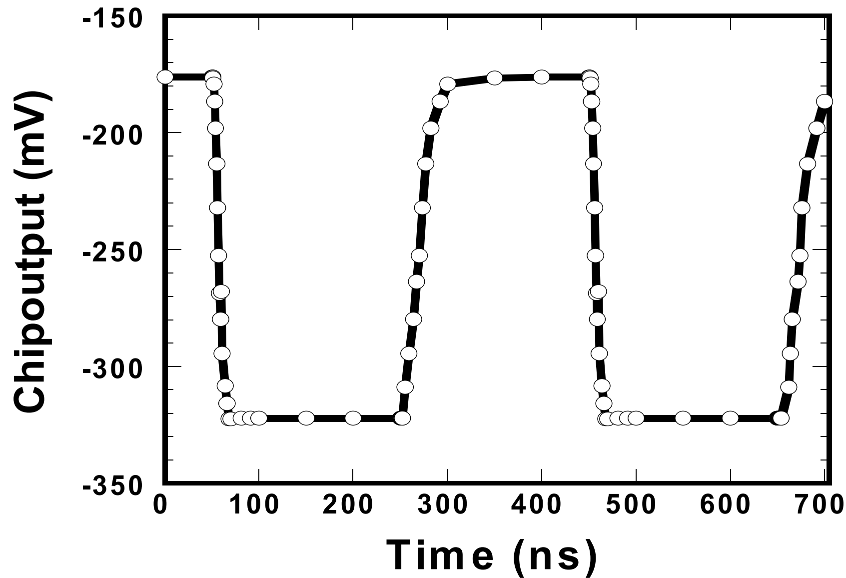

Figure 3.10 Transient analysis of the Unitcell CCBDI readout circuit for R_{dt} = 1.58 MΩ and R_{ref} = 1 MΩ.

Fig. 3.8 shows the dc analysis of the Unitcell CCBDI readout circuit plotting chipoutput (readout voltage) versus bolometer resistance R_{dt}. DC analysis of the Unitcell CCBDI readout circuit confirms the readout voltage of -176.17 mV for YBaCuO microbolometer R_{dt} of 1.58 MΩ and YBaCuO reference resistor R_{ref} of 1 MΩ. The higher the rate of change of chipoutput or readout voltage with respect to change in the bolometer resistance the better is the slope of the linear region in the dc analysis and thus result in the improvements in the sensitivity of the CCBDI readout circuit.

Fig. 3.9 shows the plot of dV_{dt}/dR_{dt} versus bolometer resistance R_{dt} of the Unitcell CCBDI readout circuit to determine the sensitivity of the CCBDI readout circuit.

Transient analysis (Fig. 3.10) confirms the readout voltage of -176.16 mV for YBaCuO microbolometer R_{dt} of 1.58 MΩ and YBaCuO reference resistor Rref of 1

MΩ. The readout voltage values from dc and transient analysis are matched at fixed R_{dt} and R_{ref}.

3.4 4x4 Array CCBDI Readout Circuit

The 4x4 array determines the 16 YBaCuO microbolometer pixels focal plane array. The output of the 4x4 array readout circuit is 16 readout voltages obtained from the electrical characteristic of the 16 YBaCuO microbolometer pixels. The microbolometers are substituted with resistance of an expected value in the schematic for simulation purpose. Fig. 3.11 shows the schematic and layout of the 4x4 array CCBDI readout circuit presenting its functional unit blocks.

3.4.1 Functional Unit Blocks

The 4x4 array CCBDI readout circuit is designed with the following functional unit blocks:

A. 4x4 Array

B. Row Shift Register

C. Column Shift Register

D. 4 CCBDI Amplifiers

E. 4 MBDI Transistors

F. 4 Current Mirrors

G. 4 Integration Capacitors and Reset Transistors

H. 4 Source Followers

I. Voltage Driver

J. Biasing Circuits

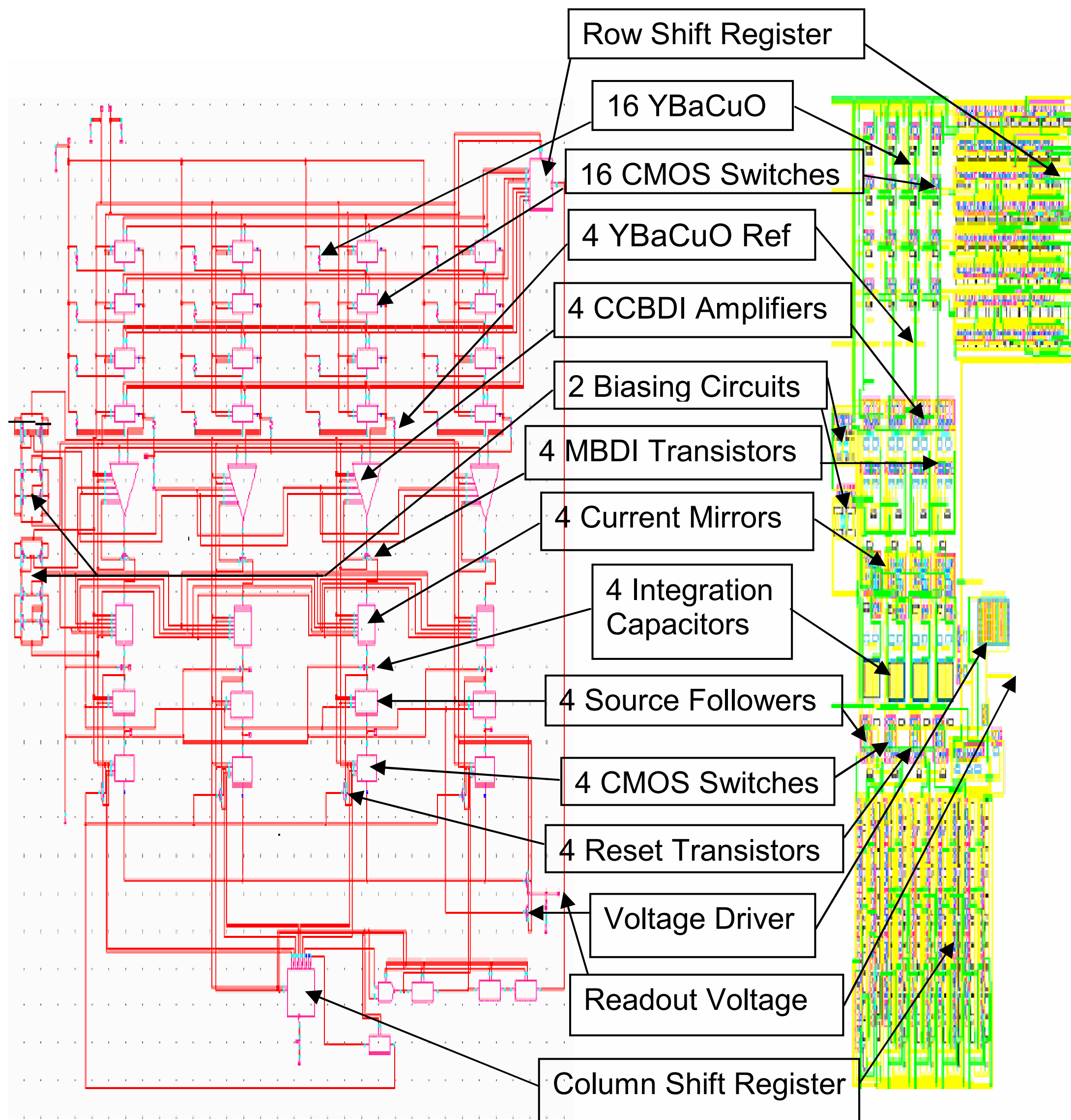

Figure 3.11 Schematic and layout of the 4x4 array CCBDI readout circuit.

A. 4x4 Array

4x4 Array constitutes the 16 YBaCuO microbolometers, 4 YBaCuO reference resistors and 16 CMOS switches. 16 YBaCuO microbolometers and 4 YBaCuO reference resistors are in CC configuration. After applying a bias current, single

YBaCuO microbolometer pixel generates a voltage V_{dt} with respect to the YBaCuO reference voltage V_{ref} in CC (Constant Current) configuration (Fig. 3.1). The V_{dt} - V_{bs} is detected as V_{out} by the CCBDI amplifier. A CMOS Switch is a parallel combination of PMOS and NMOS transistors. When PMOS and NMOS are turned on using chip-select-bar and chip-select signals respectively, CMOS Switch passes the input signal to the output.

B. Row Shift Register

4-bit Row Shift Register comprises 1 D-Flip Flop with Preset and 3 D-Flip Flop with Clear. Preset and Clear keep the starting state of DFF as 1 bit so that 1 bit is rotated in the "1000, 0100, 0010, 0001" fashion. Row shift register selects the Row 1 during "1000", Row2 during "0100", Row3 during "0010" and Row4 during "0001" in the 4x4 array readout circuit.

C. Column Shift Register

Similarly, the 4-bit Column Shift Register consists of 1 D-Flip Flop with Preset and 3 D-Flip Flops with Clear. Preset and Clear keeps the starting state of DFF as 1 bit so that 1 bit is rotated in the "1000, 0100, 0010, 0001" fashion. Column shift register selects the Column1 during "1000", Column2 during "0100", Column3 during "0010" and Column4 during "0001", in the 4x4 array readout circuit.

D. CCBDI Amplifier

The YBaCuO voltage V_{dt} and the V_{bs} are the inputs to the CCBDI amplifier (Fig. 3.2). The CCBDI current output is derived from the product of differential input (V_{dt} - V_{bs}) with CCBDI Amplifier Gain (Av). The incident radiation on the detector

causes V_{dt} smaller than V_{bs} and hence I_{out} is positive with the inward flow. The voltage V_{bs} suppresses the background DC signal and provides temperature compensation.

The MBDI Transistors, Current Mirrors, Integration Capacitors and Reset Transistors, Source Followers, Voltage Driver and Biasing Circuits are discussed previously in the section 3.3.1.

3.4.2 DC and Transient Analysis

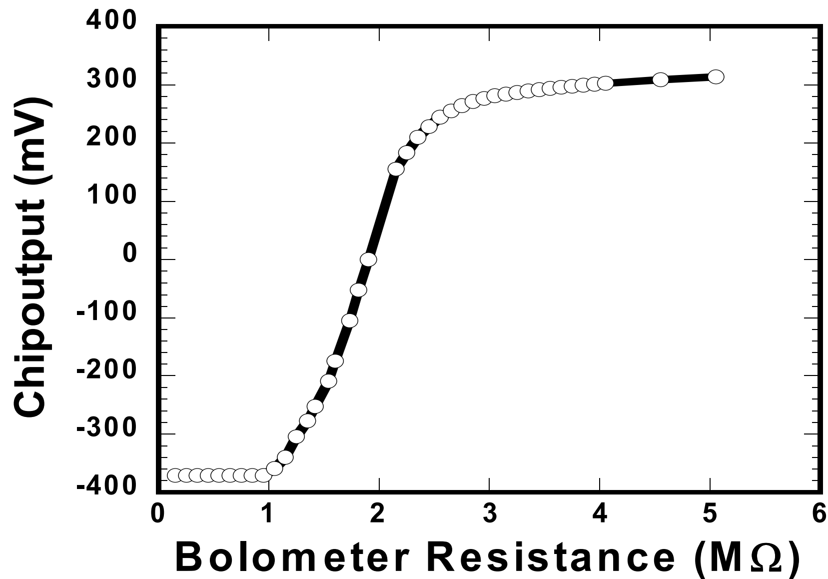

Figure 3.12 DC analysis of the 4x4 array CCBDI readout circuit.

Fig. 3.12 shows the dc analysis of the 4x4 array CCBDI readout circuit plotting chipoutput (readout voltage) versus bolometer resistance R_{dt}. DC analysis of 4x4 array CCBDI readout circuit confirms the readout voltage of -174.45 mV for YBaCuO microbolometer R_{dt} of 1.58 MΩ and YBaCuO reference resistor R_{ref} of 1 MΩ.

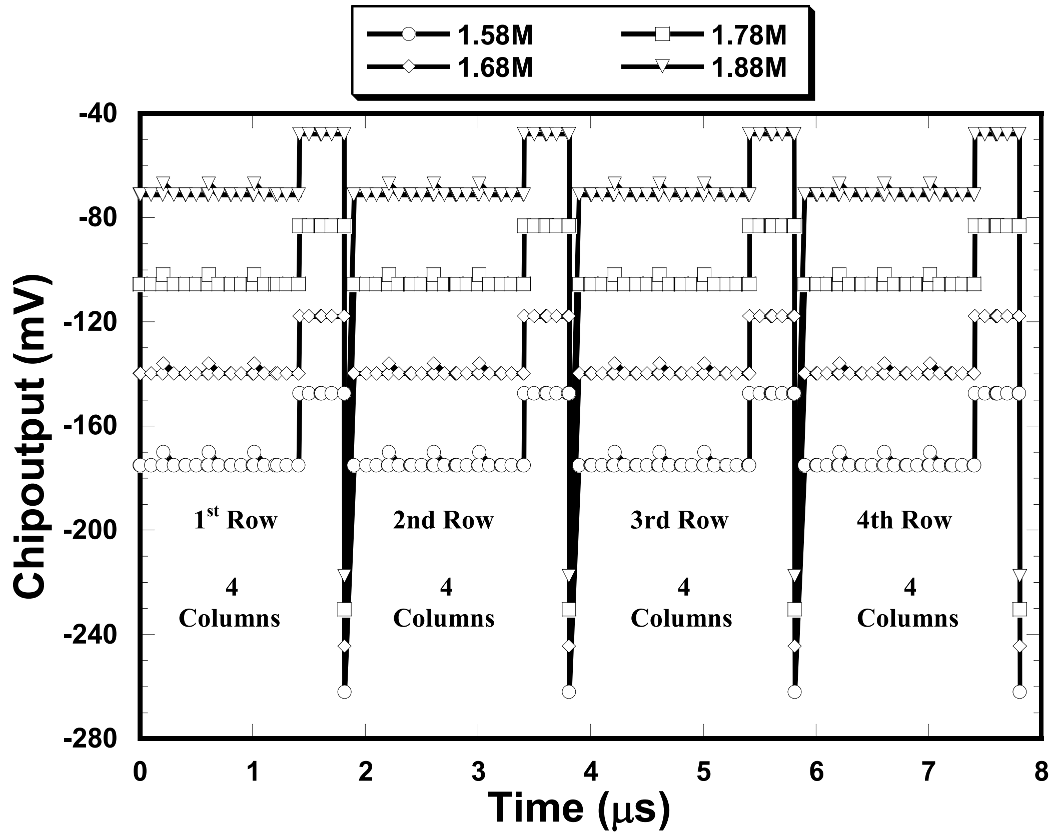

Figure 3.13 Transient analysis of the 4x4 array CCBDI readout circuit for R_{dt}=1.58 MΩ, 1.68 MΩ, 1.78 MΩ, 1.88 MΩ and R_{ref} = 1 MΩ.

Transient analysis (Fig. 3.13) confirms the readout voltage of -174.931 mV, -139.7 mV, -105.5 mV, -71.15 mV for YBaCuO microbolometer R_{dt} of 1.58 MΩ, 1.68 MΩ, 1.78 MΩ, 1.88 MΩ respectively and YBaCuO reference resistor R_{ref} of 1 MΩ. The readout voltage values from DC and transient analysis are matched at fixed R_{dt} and R_{ref}. From the transient analysis of the 4x4 array, the integration time per microbolometer pixel is measured as 15.6 ns. For the 640x480 array then, the readout time for 307200 pixels is 4.79 ms, and this translates to a frame rate of 208 Hz.

103 μA of current is drawn from the 3.5V biasing circuit with power dissipation of 0.51 mW. 79 μA of current is drawn from the 1.5V biasing circuit with power dissipation of 0.39 mW. 0.39 μA of current is drawn from the CCBDI circuit with power dissipation of 1.95 μW. The current signal undergoes CCBDI amplification and integration and is then reset by a reset transistor. For 640x480 CCBDI focal plane array, the power dissipation calculated for the bolometers and reference resistors is 1.92 mW, for the 3.5 V and 1.5 V biasing circuits is 576 mW and for the CCBDI amplifier is 1.25 mW. The overall power dissipation calculated for 640x480 CCBDI array is 579.17 mW.

Layout Design rule check is performed in the cadence for the Unitcell and a 4x4 array CCBDI readout circuits using Diva and Dracula design kit available respectively through NSCU and MOSIS.[59] LVS (Layout versus Schematic) is performed using Dracula design kit available through MOSIS. After debugging, the layout design rule check and LVS confirmed zero errors.

3.5 Conclusions

This chapter provides a detailed description of CCBDI readout circuits comprising of CCBDI amplifier, the Unitcell and a 4x4 array CCBDI readout circuits

The Constant Current (CC) configuration is discussed to describe the schematic of the CCBDI amplifier. The ac and dc analysis is also shown to achieve performance analysis of the CCBDI amplifier.

The functional unit blocks are discussed for the Unitcell CCBDI readout circuit. The dc and transient analysis are performed for the characterization of the Unitcell CCBDI readout circuit.

Similarly, the functional unit blocks are discussed for the 4x4 array CCBDI readout circuit. The dc and transient analysis are performed for the characterization of the 4x4 array CCBDI readout circuit.

CHAPTER 4

CMOS TEST CIRCUITS

4.1 Characterization

To verify the YBaCuO microbolometer fabrication process is CMOS compatible, test circuits that were easily characterized were incorporated into the die and characterized before and after microbolometer fabrication. The test circuits include CCBDI amplifier circuit, NMOS, PMOS transistors, CMOS inverters, micromachined microbolometers. Circuit measurements are performed using micromanipulator probe station on the MOSIS fabricated readout circuit die.

4.1.1 CCBDI Amplifier

The dc transfer characteristic presenting the output voltage versus input voltage plot for the CCBDI amplifier measured before and after microbolometer fabrication is shown in Fig. 4.1. The CCBDI amplifier represents a more complicated circuit comprising of several transistors. The CCBDI amplifier shows a negligible difference in the dc transfer characteristic measured before and after fabrication.

The waveforms are captured using Agilent Infinium Oscilloscope 1GHz, 4 Gsal/s. A Leader LFG-1300S is used as function generator. We can see that the curve is saturating after a high gain in the linear region. The DC Gain was measured to be 53.2.

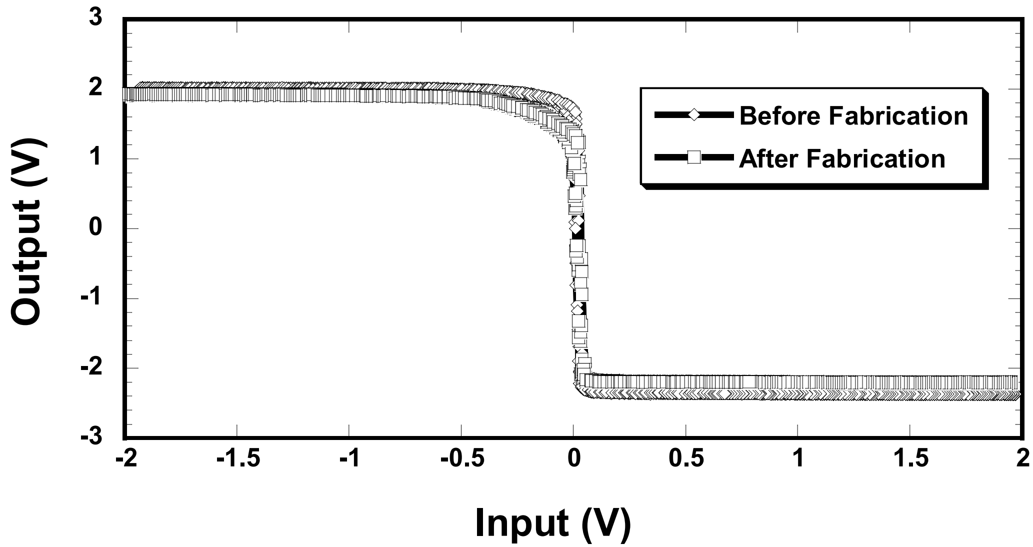

Figure 4.1 DC transfer characteristic of the CCBDI Amplifier before and after fabrication.

4.1.2 CMOS Inverter

The dc transfer characteristic presenting the output voltage versus input voltage plot for the CMOS inverter measured before and after microbolometer fabrication is shown in Fig. 4.2.

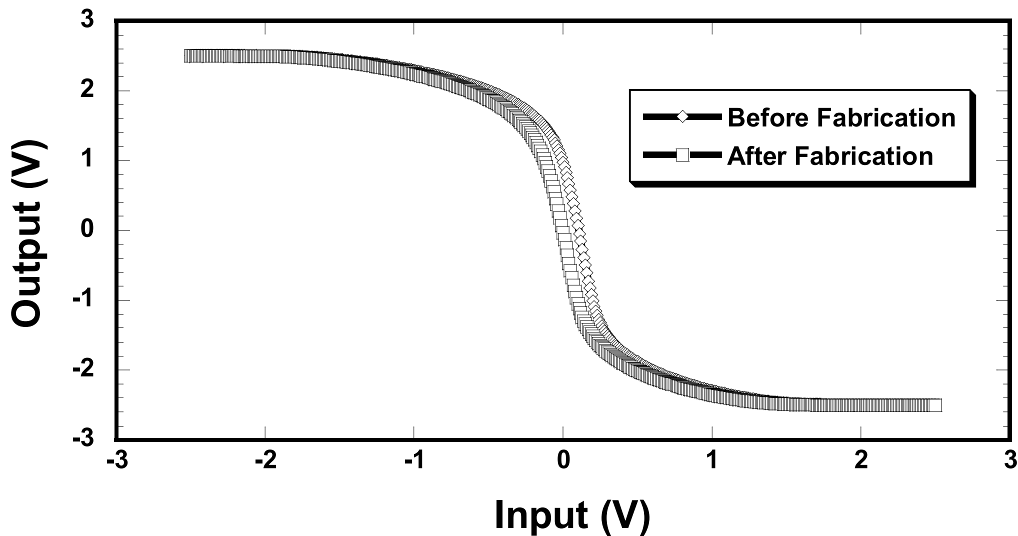

Figure 4.2 DC transfer characteristic of the CMOS inverter before and after fabrication.

There is negligible change appeared in the dc transfer characteristic of inverter before and after fabrication (Fig. 4.2). There is some offset visible in the transfer characteristic of the inverter which is due to the fact that hole mobility is significantly lower than electron mobility (because of higher effective mass of hole than that of electron) while keeping the W/L ratios same for NMOS and PMOS transistors.

4.1.3 NMOS and PMOS Transistors

The current-voltage characteristics of the NMOS and PMOS test transistors were measured before and after fabrication. Presented in Fig. 4.3 is the drain-to-source current I_{DS} versus drain-to-source voltage V_{DS} characteristics for different gate-to-source voltage V_{GS} values of three NMOS measured before and after fabrication.

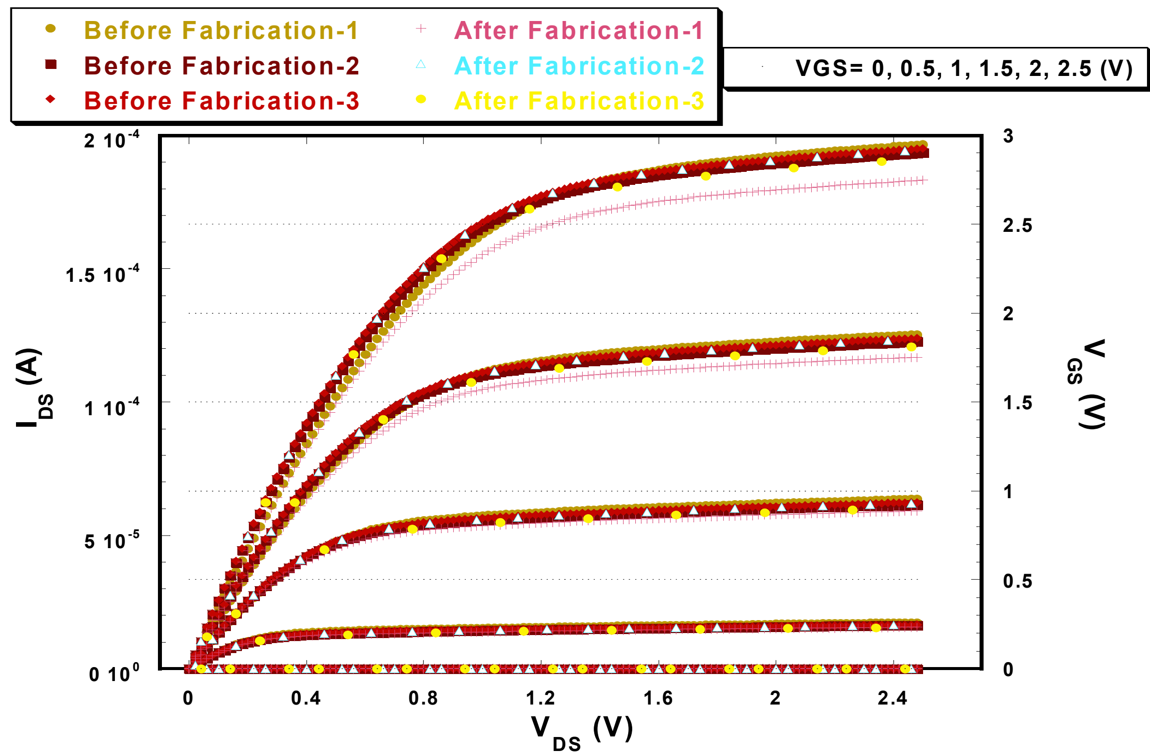

Figure 4.3 Current-voltage characteristic of three NMOS transistors before and after fabrication.

Fig. 4.4 shows the drain-to-source current I_{DS} versus drain-to-source voltage V_{DS} characteristics for different gate-to-source voltage V_{GS} values of three PMOS measured before and after fabrication.

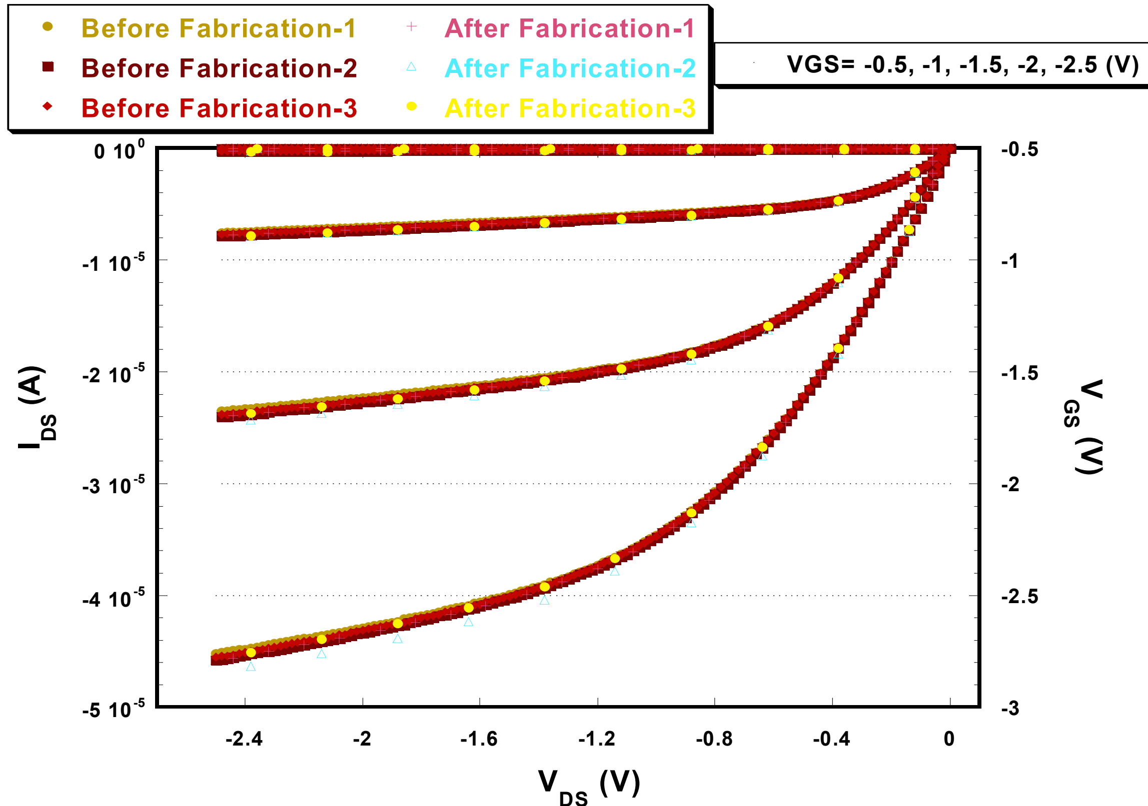

Figure 4.4 Current-voltage characteristic of three PMOS transistors before and after fabrication.

The results show minimal variation from transistor to transistor and no visible difference before and after fabrication, indicating no change in the threshold voltage or drain saturation current of NMOS and PMOS transistors.

4.1.4 Micromachined Microbolometers

The die contained several test microbolometers structures that were not integrated with the readout circuit. These test microbolometers were fabricated and

bonded for their characterization showing that they are functioning microbolometers matching the requirements of the design. The area of the test microbolometers was 31x31 μm^2. Fig. 4.5 shows the IV characteristic of four micromachined YBaCuO test microbolometers for a 75-μm-long electrode arm geometry.

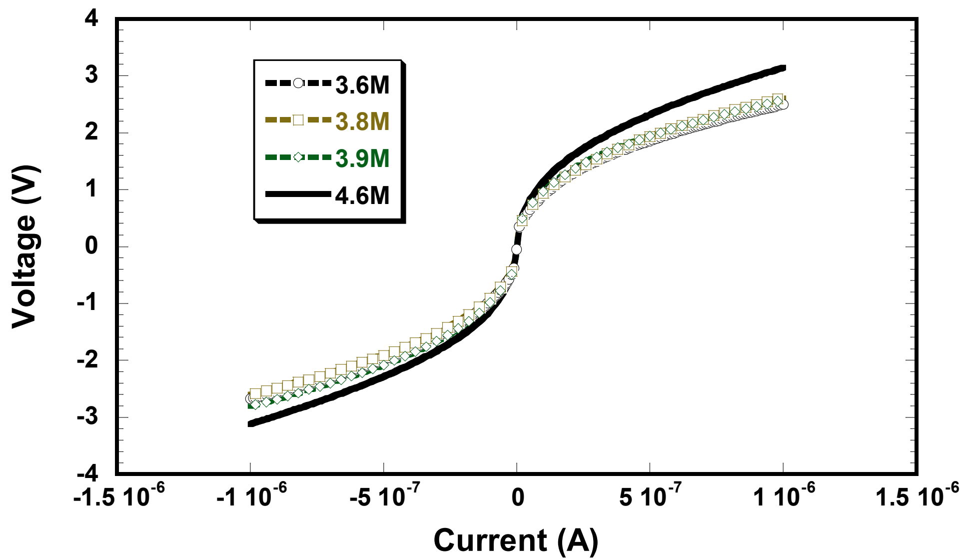

Figure 4.5 Current-voltage characteristic of four micromachined YBaCuO test microbolometers for a 75-μm-long electrode arm geometry.

The heating effect attributes to the non-linearity in the IV characteristic of 3.6 MΩ, 3.8 MΩ, 3.9 MΩ and 4 MΩ test microbolometers. There is a marginal change appeared in the IV characteristics of the microbolometers due to the different resistance values. The measured value of effective thermal conductance is 1.37x10^{-7} W/K which is close to the theoretical value of 3.66x10^{-7} W/K. The device was kept in vacuum for the measurement and the calculation is described in section 6.5. The measured value of the thermal conductance G_{th} is 1.01x10^{-7} W/K which is also close to the theoretical value of

$2.92 x 10^{-7}$ W/K. The design value is in close agreement with the measured value for the 75-µm-long electrode arm geometry for a 30 Hz frame rate.

4.2 Conclusions

This chapter presents the characterization of test circuits including CCBDI Amplifier, CMOS Inverter, NMOS, PMOS Transistors, and Micromachined Microbolometers fabricated on the die in order to verify the YBaCuO microbolometer fabrication process is CMOS compatible.

The CCBDI amplifier shows a negligible difference in the dc transfer characteristic measured before and after fabrication.

There is negligible change found out in the dc transfer characteristic of CMOS inverter before and after fabrication.

There is minimal variation from transistor to transistor and no visible difference before and after fabrication, indicating no change in the threshold voltage or drain saturation current of NMOS and PMOS transistors.

The heating effect attributes to the non-linearity in the IV characteristic of four test microbolometers. There is a marginal change appeared in the IV characteristics of the microbolometers due to the different resistance values.

CHAPTER 5

MICROBOLOMETER DESIGN AND FABRICATION

5.1 Introduction

This dissertation presents the design and fabrication of micromachined YBaCuO microbolometers, an entirely self-supporting structure. The characteristics of the microbolometer are determined by the properties of materials used along with the dimensions of thin films. Surface micromachining has been employed to fabricate YBaCuO microbolometers on CCBDI readout circuits. Surface micromachining enables the fabrication of microbolometers by stacking and patterning thin films on the die integrated with CCBDI readout circuitry and wiring. Surface micromachining is advantageous over bulk micromachining since bulk micromachining involves etching a large single crystal substrate, where structures are bigger due to angling, hence causes wastage of silicon real estate. The fabrication technique also allows for control over microbolometer response time and detectivity. Higher sensitivity is obtained by further increasing the thermal isolation, resulting in increased responsivity.

Surface micromachining utilizes a sacrificial layer to suspend the microbolometer thermometer above the substrate by its electrode arms for thermal isolation.[62, 63, 64] A polyimide sacrificial mesa formed by HD Microsystems PI2737 was used to suspend the YBaCuO thermometer above the substrate. No supporting membrane or encapsulation was used in this self-supporting structure. This represents a

significant improvement in state-of-art of microbolometer fabrication by eliminating the thermal mass associated with supporting membrane. Also, this structure is not affected by the warping problems associated with stress imbalances in multilayer microbolometer structures that utilize a supporting membrane such as Si_3N_4. It means that being a self-supporting detector the thermal mass is low, which in turn can provide a faster thermal time constant for the same degree of thermal isolation. Alternatively, the lower thermal mass can be used to achieve increased thermal isolation while maintaining the same thermal time constant and frame rate.

The self-supporting YBaCuO microbolometers are designed, fabricated and on-chip integrated for the first time with a CCBDI readout circuit in AMI 1.5 μm double-poly-double-metal nwell 2.5V CMOS technology.

5.2 Design and Fabrication

The self-supporting semiconducting-YBaCuO microbolometers with the cell size of 31x31 μm^2 are fabricated on the top of CCBDI readout circuitry using cleanroom facility in NanoFab center at the University of Texas Arlington. The YBaCuO microbolometers (Fig. 5.1) were designed with two different electrode arm geometries to provide thermal isolation from the substrate. This was achieved by changing only one mask, which was used to pattern the sacrificial polyimide PI2737. One electrode arm geometry was designed to obtain a relatively fast 200 Hz frame rate (Fig. 5.1b) while maintaining a detectivity of 10^8 $cmHz^{1/2}/W$. The other electrode arm geometry was designed to achieve a detectivity of 10^9 $cmHz^{1/2}/W$ while maintaining a traditional 30 Hz frame rate (Fig. 5.1c).

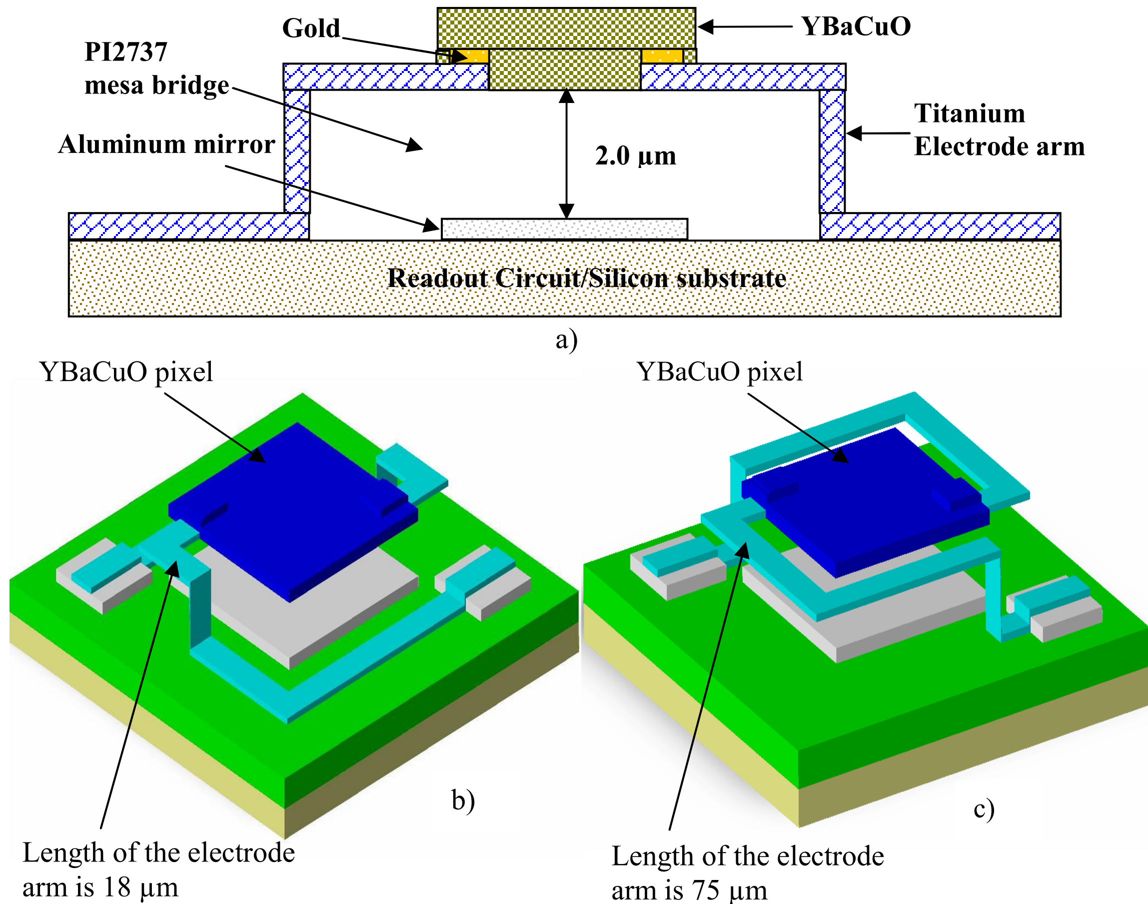

Figure 5.1 (a) Cross-sectional view of a YBaCuO microbolometer. CoventorWare® model of the micromachined microbolometers showing (b) the 18-µm-long electrode arm geometry for a 200 Hz frame rate and (c) the 75-µm-long electrode arm geometry for a 30 Hz frame rate.

The MOSIS foundry service was used to fabricate the readout circuits, providing the circuits as unplanarized die. The CMOS compatible YBaCuO microbolometer fabrication process presented in this dissertation could also be used to fabricate YBaCuO microbolometer on the full silicon wafers. The YBaCuO microbolometers were fabricated on the CMOS die with the CCBDI readout circuitry to form focal plane arrays using a surface micromachining technique. The CMOS readout circuit was fabricated with 8x8 μm^2 glass cuts to facilitate the electrical connection between the readout circuitry, the YBaCuO microbolometers and the YBaCuO reference resistors.

Prior to the deposition of the aluminum mirror, titanium, gold, and YBaCuO, the standard photolithography process involved six basic steps as follows:

1) Spin coating the negative photoresist NR7-1500P at 3000 rpm for 40 seconds in order to achieve a resist film of 140-160 nm thick.
2) Pre-baking the photoresist at 150 ^{0}C on a hot plate for 60 seconds.
3) Exposing the photoresist under the mask for 25 seconds (aluminum mirror, and titanium) and 20 seconds (gold and YBaCuO). Lesser time is used in the exposure for gold and YBaCuO to protect the undercut through UV (Ultraviolet) light due to overexposing. Hence 20 seconds is chosen for best possible patterning results.
4) Post-baking the photoresist at 120 ^{0}C on a hot plate for 60 seconds.
5) Developing the unexposed (other than yellow light) pattern with negative resist developer RD6 and DI (Deionized water) with 3:1 ratio (90ml:30ml) for 80-90

seconds for aluminum mirror, 5-9 minutes for titanium, 50 seconds for gold and 50 seconds for YBaCuO.

6) Blow drying the wafer with N_2.

The standard photolithography process for PI2737 polyimide sacrificial layer involved the following eight steps.

1) Spin coating the polyimide PI2727 at 2200 rpm for 30 seconds in order to achieve a PI2737 film of 3-4 μm thick.
2) Pre-baking the polyimide PI2727 at 65 ^{0}C on a hot plate for 3 minutes and then hard-baking at 95 ^{0}C on a hot plate for 3 minutes.
3) Exposing the polyimide PI2727 under the mask for 25 seconds.
4) Developing the unexposed pattern using following procedure in four separate beakers:

   i) Develop in 100 % DE 9040 developer for 14 seconds, ii) Develop in 50 % DE 9040 + 50 % RI 9080 rinse for 14 seconds, iii) Rinse in 100 % RI 9080 for 15 seconds, iv) Again, rinse in 100 % RI 9080 for 15 seconds.
5) Blow drying the wafer with N_2.
6) Checking under the microscope for quality of develop.
7) Soft-baking the wafer at 100 ^{0}C on a hot plate for 2 minutes.
8) Loading the wafer in the oven for curing, first raising the oven temperature from 25 ^{0}C to 300 ^{0}C in 75 minutes, then keeping at 300 ^{0}C for 4 hours and finally decreasing the oven temperature from 300 ^{0}C to 25 ^{0}C in 75 minutes. Thus, providing the cured polyimide PI2737 thickness of around 2 μm.

The microbolometer fabrication process started with bonding the CMOS readout die on a silicon carrier wafer (Fig. 5.2a) using polyimide PI2555. The fabrication steps involved the deposition of the aluminum mirror (step 1), PI2737 polyimide sacrificial layer spin-coating (step 2), titanium deposition (step 3), gold deposition (step 4), YBaCuO deposition (step 5) and finally polyimide ashing (step 6) to obtain the suspended bridge structure. A turbo-pumped rf sputter system was used for all sputter depositions using 3-inch targets.

At first, the aluminum (Al) mirror (Fig. 5.2b) was deposited by thermal evaporation to obtain 400 nm of thickness and patterned by liftoff, to form an optically resonant cavity with the suspended YBaCuO thermometer. The cavity height was designed to be 2 μm, at approximately λ/4 wavelength, to increase absorption in the 8-14 μm atmospheric transmission window (Fig. 2.2). The aluminum was also patterned to partially fill the glass cuts in the readout die and help with the electrical connection between the readout circuit and the microbolometers. Next, the sacrificial polyimide layer (HD Microsystems PI2737) was spin coated and patterned using negative lithography (Fig. 5.2c). The polyimide was cured at 275 ^{0}C for curing up to 4 hours. The PI2737 polyimide layer thickness, around 2 μm, formed the polyimide mesa bridge to determine the distance between the YBaCuO and aluminum mirror. The 100-nm-thick or 200-nm-thick titanium (Ti) was sputtered onto the die and patterned by liftoff to form electrode arms that support the YBaCuO thermometer above the substrate. One of two electrode arm geometries investigated was selected by the sacrificial polyimide pattern. The 200-nm-thick and 18-μm-long electrode arm was designed to achieve a

relatively fast 200 Hz frame rate (Fig. 5.1b). Similarly, the 100-nm-thick and 75-µm-long electrode arm was designed to achieve a traditional 30 Hz frame rate (Fig. 5.1c). The titanium (Fig. 5.2d) was deposited by rf magnetron sputtering at 150W in pure argon environment at 10 mTorr pressure. The total time spent in sputtering was 47 minutes and 30 seconds to get 200-nm-thick Ti. This shows that the Ti deposition rate was approximately 0.07 nm/s. The 75-µm-long arm has lower thermal conductance than 18-µm-long electrode arm. This results in higher detectivity for 30 Hz frame rate microbolometers than that of 200 Hz frame rate microbolometers. The titanium electrode arms hold the YBaCuO thermometer above the substrate to achieve thermal isolation. The titanium has low thermal conductivity compared to other materials as Au or Al. Nickel chromium also has a low thermal conductivity and could be used. The low thermal conductance of the electrode arms minimizes the heat transfer from the YBaCuO thermometer to the substrate and resulting in high responsivity. Next, a 40-nm-thick gold film was deposited and patterned by liftoff to form an ohmic contact between Ti arms and the YBaCuO thermometer (Fig. 5.3a). The gold (Au) was sputtered at 100W in pure argon environment at 10 mTorr pressure. The total time spent in sputtering was 2 minutes and 35 seconds to obtain 40-nm-thick gold film. This shows that the Au deposition rate was approximately 0.26 nm/s. Au forms a good electrical contact with semiconducting YBaCuO. Then the 400-nm-thick YBaCuO (Fig. 5.3b) was deposited by rf magnetron sputtering at 75W in pure argon environment at 10 mTorr pressure. The YBaCuO thermometer was patterned by liftoff. The total time spent in sputtering was 3 hours and 19 minutes to obtain 400-nm-thick YBaCuO. This

shows that the YBaCuO deposition rate was approximately 0.033 nm/s. Finally, the sacrificial polyimide layer (Fig.5.3c) was removed by ashing in an oxygen plasma for approximately 21 hours at 150W plasma in pure oxygen environment at 1 mbar pressure. The removal of the PI2737 sacrificial polyimide layer created an approximately 2 µm microcavity between the YBaCuO thermometer and the aluminum mirror. After ashing the sacrificial polyimide, the self-supporting YBaCuO pixel is suspended by titanium arms providing thermal isolation from the substrate.

This completed the microbolometer fabrication process. Scanning electron microscope (SEM) images of fabricated self-supporting-YBaCuO microbolometers for the 75-µm-long electrode arm geometry for a 30 Hz frame rate with a pixel size of 31x31 μm^2 are shown in Fig. 5.4, which includes a portion of a 4x4 microbolometer pixel array with CCBDI readout circuit (Fig. 5.4a) and the closer view of the same (Fig. 5.4b).

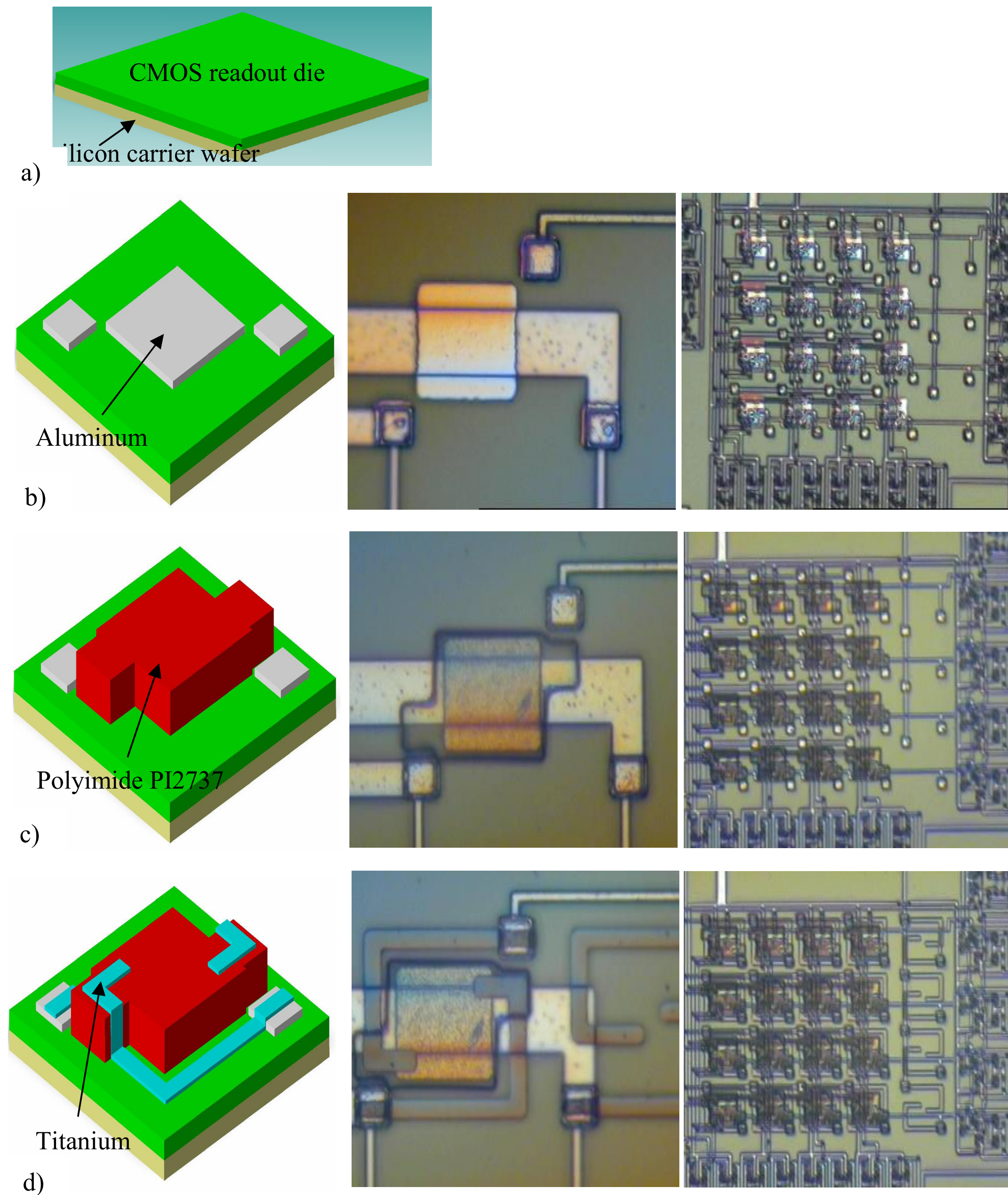

Figure 5.2 (a) Fabrication started with the CMOS readout die bonded to silicon carrier wafer. (b) Aluminum deposition. Shown in a CoventorWare® schematic, a Unitcell, and a 4x4 array integrated with the CCBDI readout circuitry. (c) Sacrificial polyimide PI2737 coating and patterning for a 200 Hz frame rate shown for the same series of photos. (d) Titanium deposition and patterning to form the 18-µm-long electrode arms with the same series of photos.

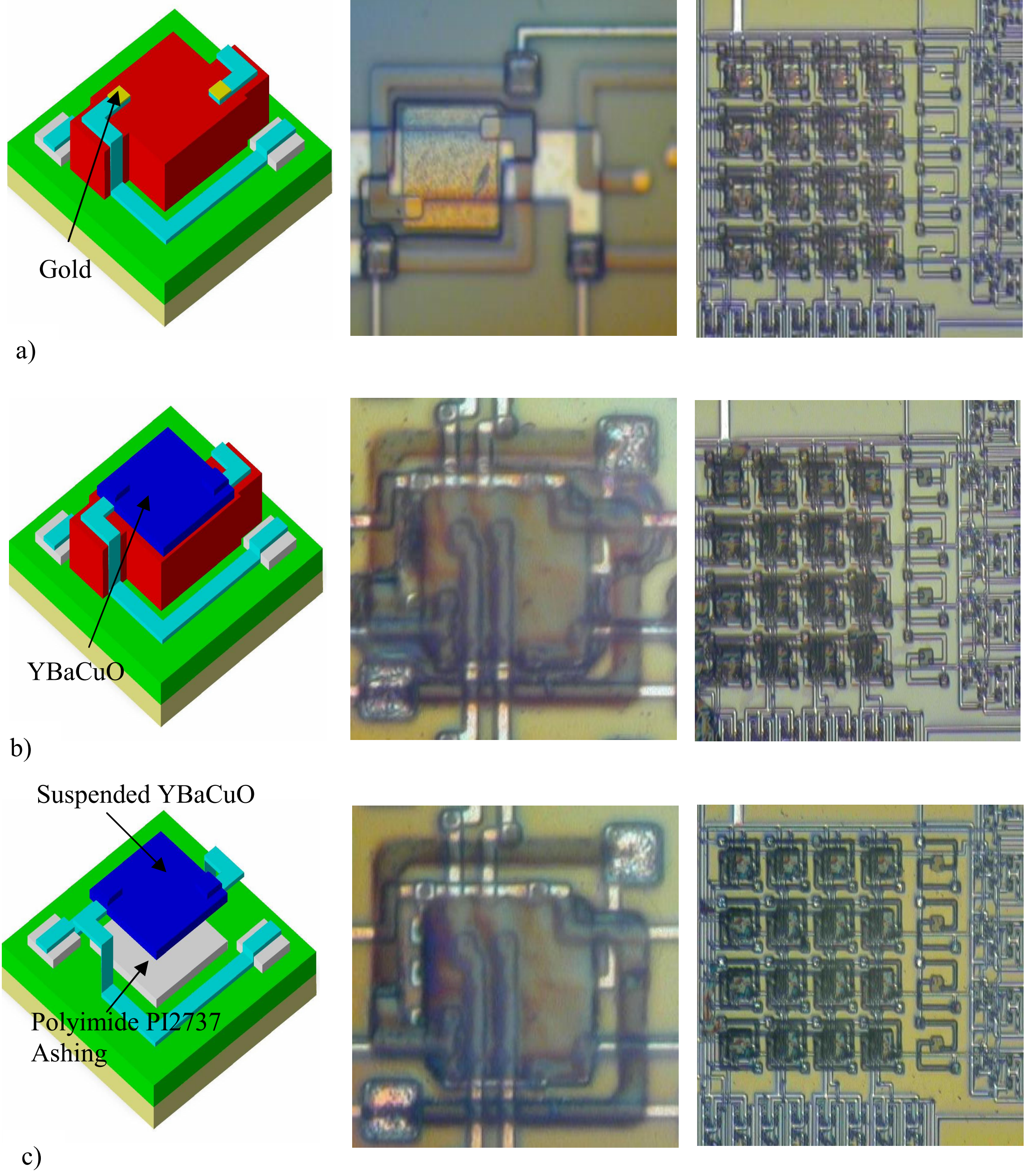

Figure 5.3 Microbolometer fabrication continued using a Coventorware® schematic, image of a Unitcell, and a 4x4 array integrated with the CCBDI readout circuitry. (a) Gold contact deposition and patterning. (b) YBaCuO thermometer deposition and patterning. (c) Sacrificial polyimide PI2737 ashing to complete the microbolometer fabrication process.

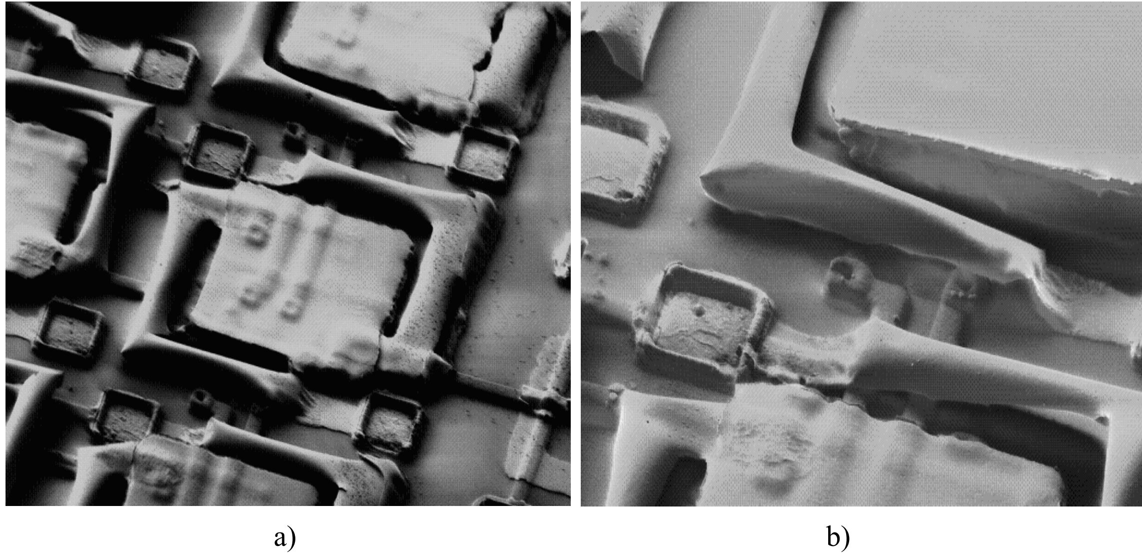

a) b)

Figure 5.4 SEM micrograph of fabricated YBaCuO microbolometers for the 75-μm long electrode arm geometry for a 30 Hz frame rate with pixel size of 31x31 μm^2 (a) a portion of 4x4 microbolometer pixel array with the CCBDI readout circuit. (b) Closer view of the 4x4 array.

5.3 Conclusions

The chapter has explained the design and fabrication process involved in the development of micromachined microbolometer integrated on top of the CCBDI readout circuit. The self-supporting YBaCuO microbolometers are designed, fabricated and on-chip integrated for the first time with a CCBDI readout circuit.

The YBaCuO microbolometers were designed with two different electrode arm geometries to provide the thermal isolation from the substrate. One electrode arm geometry was designed to obtain a relatively fast 200 Hz frame rate while maintaining a detectivity of 10^8 $cmHz^{1/2}/W$. The other electrode arm geometry was designed to achieve a detectivity of 10^9 $cmHz^{1/2}/W$ while maintaining a traditional 30 Hz frame rate.

CHAPTER 6

MICROBOLOMETER CHARACTERIZATION

6.1 Introduction

This chapter describes the electrical and optical characterization of the microbolometer performed in the microsensors lab. The die contained several test microbolometers structures that were not integrated with the readout circuit. The area of the test microbolometers was 31x31 μm^2. The test YBaCuO microbolometers were fabricated concurrently with the Unitcell and a 4x4 array microbolometer pixels on the same die. In other words, these test microbolometers are replica of microbolometer pixels which are integrated with the Unitcell and a 4x4 array CCBDI readout circuits. The test microbolometers were wire bonded and mounted in vacuum inside a cryostat and characterized to measure temperature dependent resistance (R(T)), temperature coefficient of resistance (TCR), activation energy (E_a), current-voltage (IV) characteristic and thermal conductance (G_{th}).

In the later part of this chapter, the optical response involving responsivity (R_v) and detectivity (D*) measurements of the self-supporting YBaCuO micromachined microbolometer detector array integrated with CCBDI readout circuit are discussed and analyzed. Fig. 6.1 shows the test YBaCuO microbolometers with the pixel size of 31x31 μm^2 fabricated for characterization. One die is fabricated with the 75-µm-long electrode

arm geometry for a 30 Hz frame rate (6.1a) and the other die is fabricated with the 18-µm-long electrode arm geometry for a 200 Hz frame rate (Fig. 6.1b).

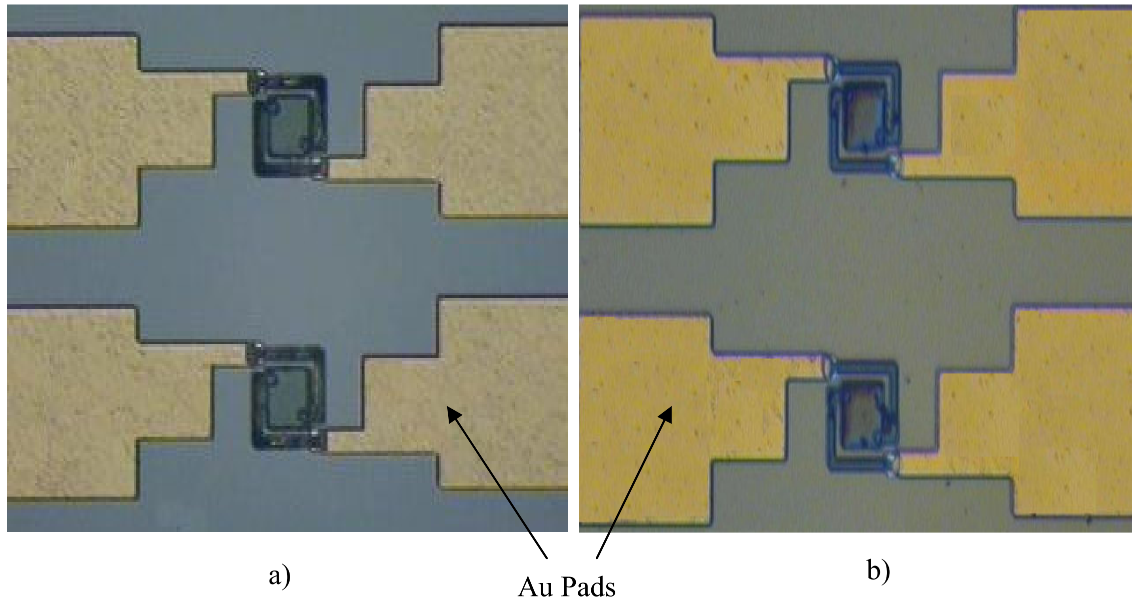

Figure 6.1 Test YBaCuO micromachined microbolometers with pixel size of 31x31 μm^2 for characterization. (a) the 75-µm-long electrode arm geometry for a 30 Hz frame rate. (b) the 18-µm-long electrode arm geometry for a 200 Hz frame rate.

6.2 Temperature Dependent Resistance (R (T)) and Temperature Coefficient of Resistance (TCR)

The temperature dependent resistance R (T) and temperature coefficient of resistance TCR versus temperature measurements were performed on the 31x31 μm^2 test YBaCuO micromachined microbolometer. The electrical resistance of the test bolometer (Fig. 6.1a) was 3.6 MΩ at 295 K. The test bolometer under observation was kept in the cryostat at 10mT. A Lakeshore DRC-91C Temperature controller with the combination of Leybold RW3 closed cycle refrigerator/cryogenic cooler was used to control the temperature of the test microbolometer. The temperature controller has four

wires connection to the sensor diode or temperature sensor attached to the stage on which test bolometer (Device Under Test) rests. These four wires are basically two heater output wires and two sensor input wires. The two heater output wires are heating filaments that heat the test bolometer from 295 K to 325 K. The length of wire from the temperature controller corresponds to 25 Ω resistance to achieve maximum power output. The two sensor input wires connect to the sensor diode for temperature display on the controller. The cooler keeps the temperature below room temperature from 295 K to 200 K.

Fig. 6.2 demonstrates the measurement set up for R (T) and TCR versus temperature showing three HP34401A multimeters. One multimeter was used as an ohmmeter to provide a fixed dc bias current across a 200 KΩ (R_2) input resistance, and the other two measured the voltages across 10 KΩ (R_1) series resistance and the input resistance (R_2). The vacuum in the cryostat was created by the mechanical pump.

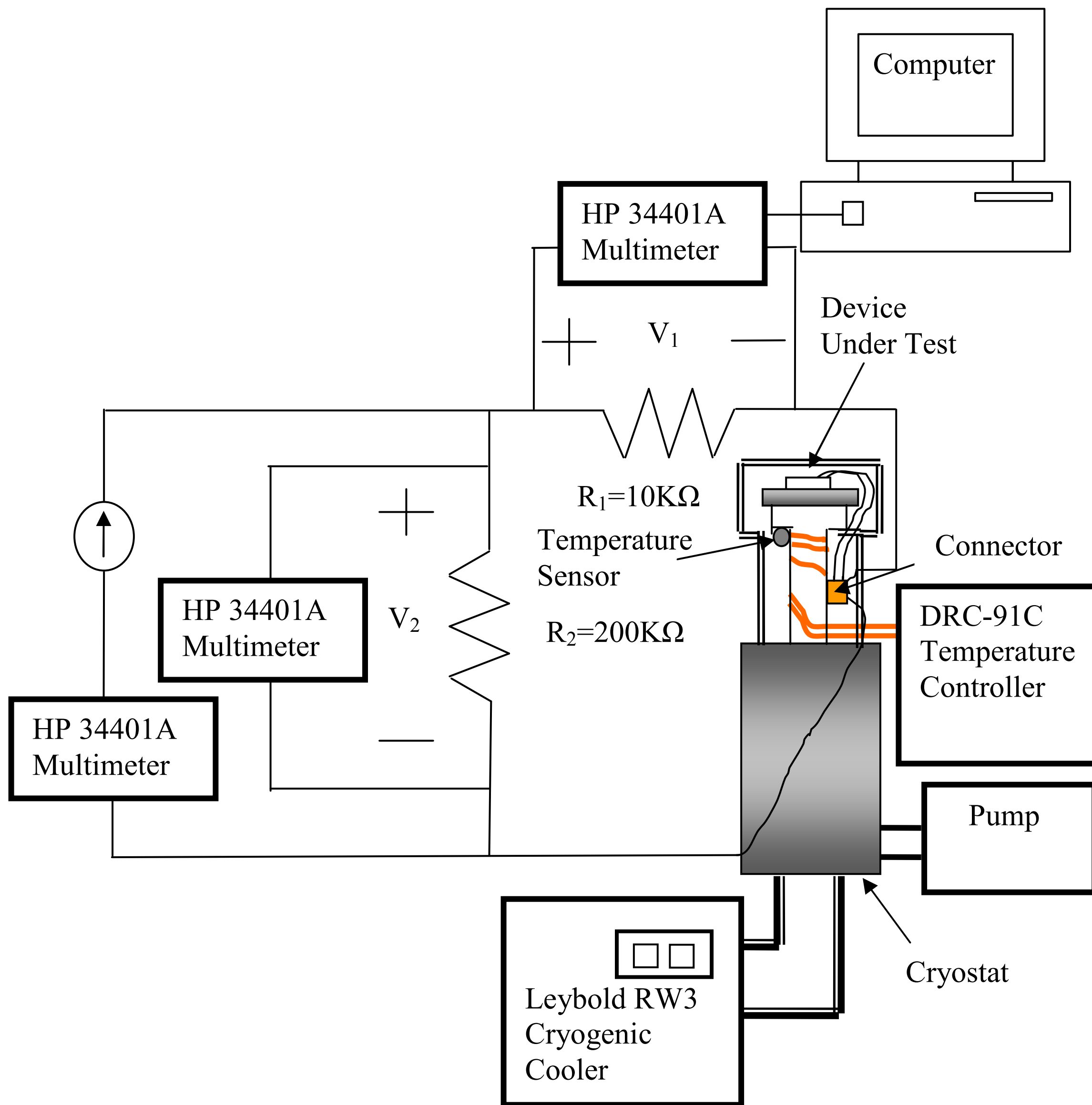

Figure 6.2 Measurement set up for temperature dependent resistance R (T) and temperature coefficient of resistance TCR versus temperature.

The resistance versus temperature characteristic and the calculated TCR are shown in Fig. 6.3 (electrode arms based on 30 Hz frame rate) and Fig. 6.4 (electrode arms based on 200 Hz frame rate). The resistance versus temperature characteristic obeys the Arrhenius relation given by

$$TCR = \alpha = -\frac{E_a}{k_B T^2} \tag{6.1}$$

where E_a is the activation energy and T is the microbolometer temperature.

The measured TCR is -3.16 %/K at room temperature (295 K) for the 75-µm-long electrode arm geometry for a 30 Hz frame rate. This agrees with the value measured by Almasri et al.[36]

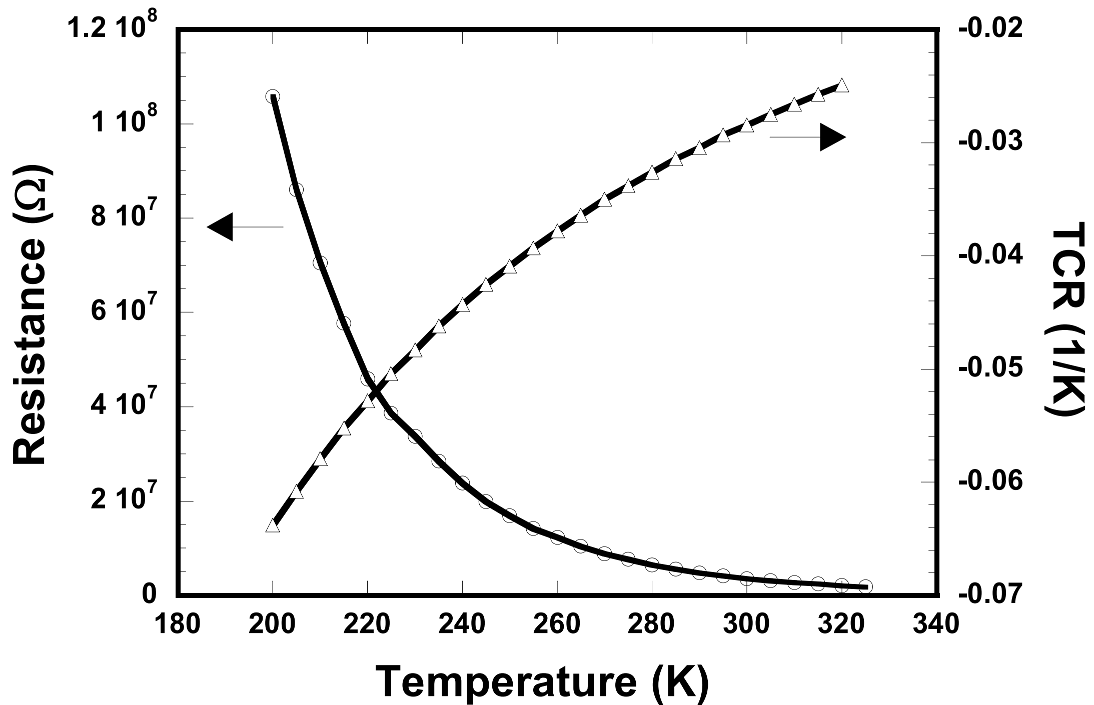

Figure 6.3 Resistance R (T) and TCR versus temperature range of 200 K to 325 K for the 75-µm-long electrode arm geometry for a 30 Hz frame rate.

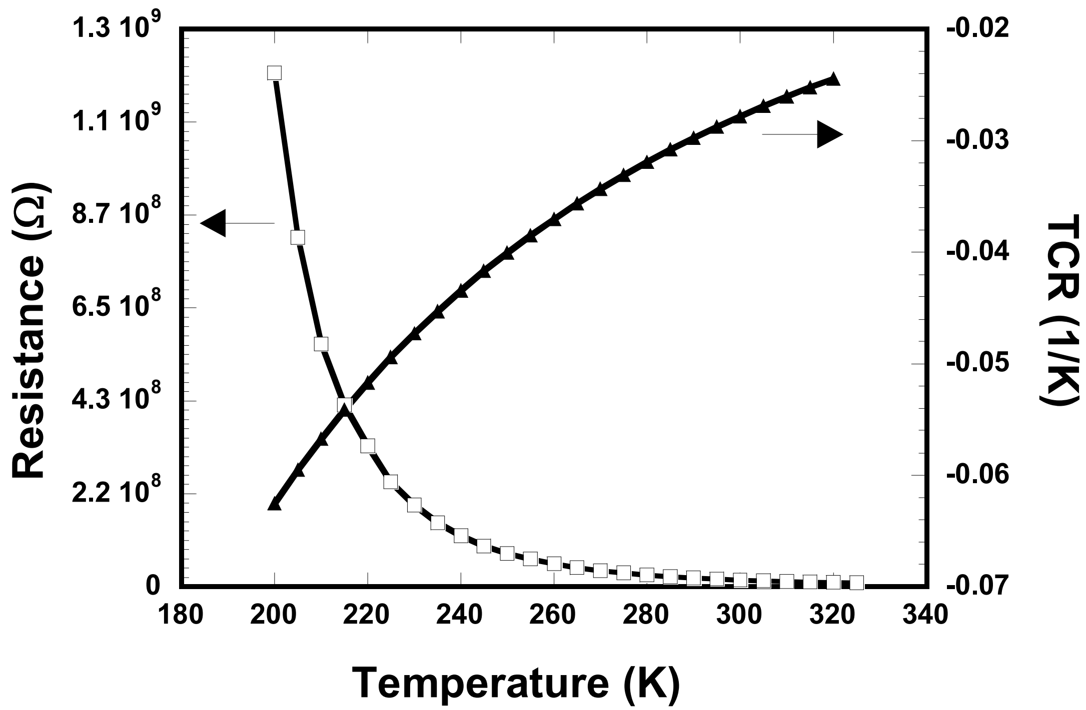

Figure 6.4 Resistance R (T) and TCR versus temperature range of 200 K to 325 K for the 18-μm-long electrode arm geometry for a 200 Hz frame rate.

The measured TCR is -2.9 %/K at room temperature (295 K) for the 18-μm-long electrode arm geometry for a 200 Hz frame rate.

6.3 Activation Energy (E_a)

The plot shows natural logarithm of microbolometer Resistance versus $1/k_BT$ where slope (Fig. 6.5) provides the value of activation energy (E_a) of 0.216eV of the YBaCuO microbolometer (electrode arms based on 30 Hz frame rate), and (Fig. 6.6) provides the value of activation energy (E_a) of 0.215eV of the YBaCuO microbolometer (electrode arms based on 200 Hz frame rate). The activation energy corresponds to the

energy between fixed state Fermi glass and the valence band which involves movement of holes to the valence band in p-type carrier semiconducting YBaCuO.

$$R(T) = R_0 \exp\left(\frac{E_a}{k_B T}\right) \tag{6.2}$$

$$\ln R(T) = \ln R_0 + \frac{E_a}{k_B T} \tag{6.3}$$

where k_B is the Boltzmann's constant, R_o is the resistance at infinite temperature obtained from intercept.

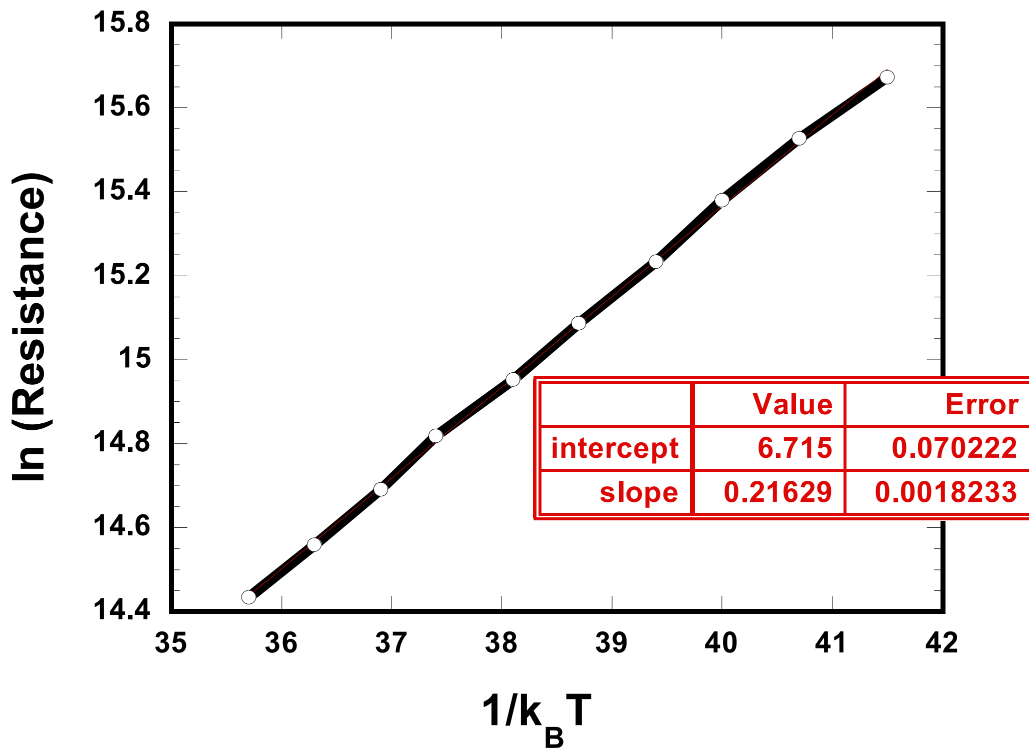

Figure 6.5 Plot of ln (Resistance) versus $1/k_B T$ plot showing activation energy (E_a) for the 75-µm-long electrode arm geometry for a 30 Hz frame rate.

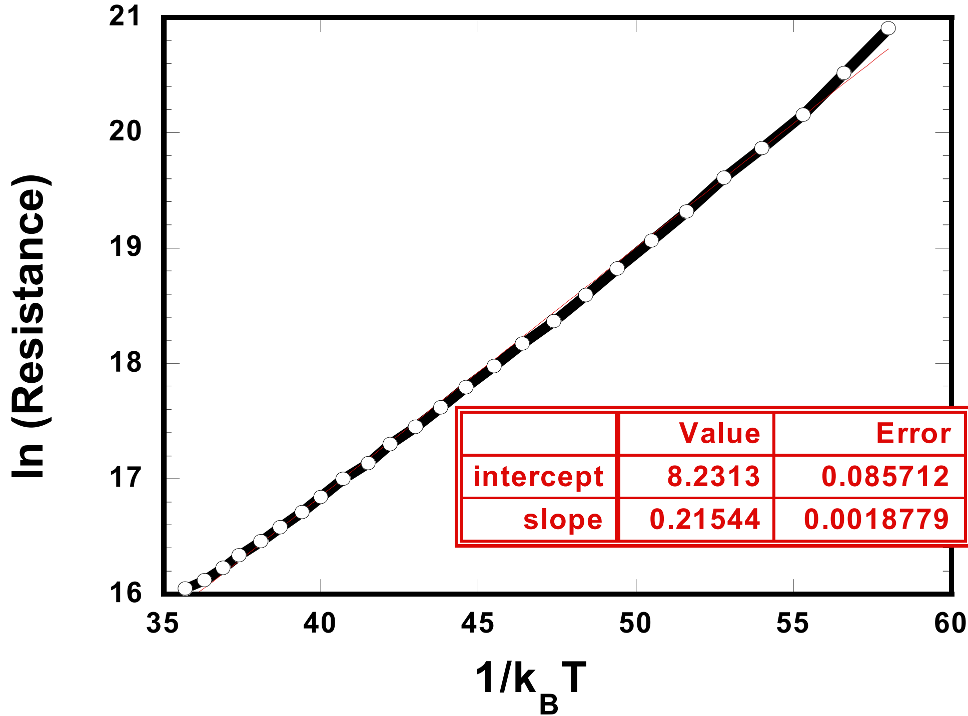

Figure 6.6 Plot of ln (Resistance) versus $1/k_BT$ plot showing activation energy (E_a) for the 18-µm-long electrode arm geometry for a 200 Hz frame rate.

6.4 Current-Voltage (IV) Characteristic

The current-voltage (IV) characteristics were measured to determine the thermal conductance G_{th} to the substrate. The IV characteristic of the YBaCuO microbolometer is presented in Fig. 6.7 (electrode arms based on 30 Hz frame rate) and in Fig. 6.8 (electrode arms based on 200 Hz frame rate). The non-linearity in the IV characteristic of test YBaCuO thermometer is attributed to the heating affect from the power loss caused by current biasing. The IV curve measured for the test microbolometer with electrode arms based on 200 Hz frame rate from Fig. 6.8 shows higher non-linearity as compared to that of electrode arms based on 30 Hz frame rate because of its much higher value of fabricated microbolometer resistance.

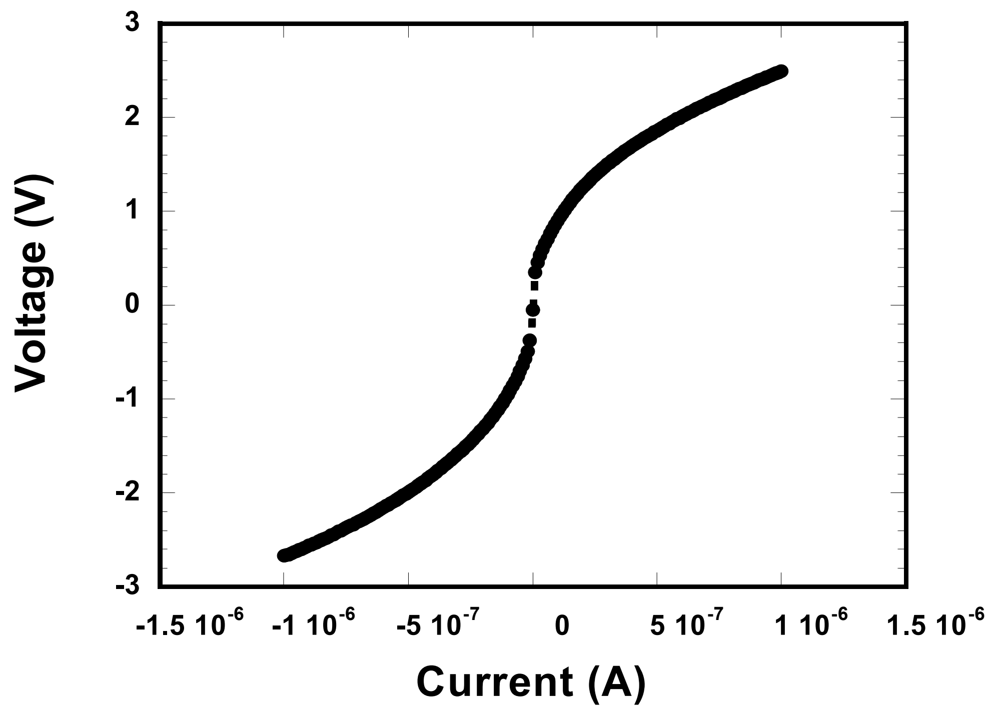

Figure 6.7 IV characteristic of test YBaCuO microbolometer for a 75-µm-long electrode arm geometry for a 30 Hz frame rate.

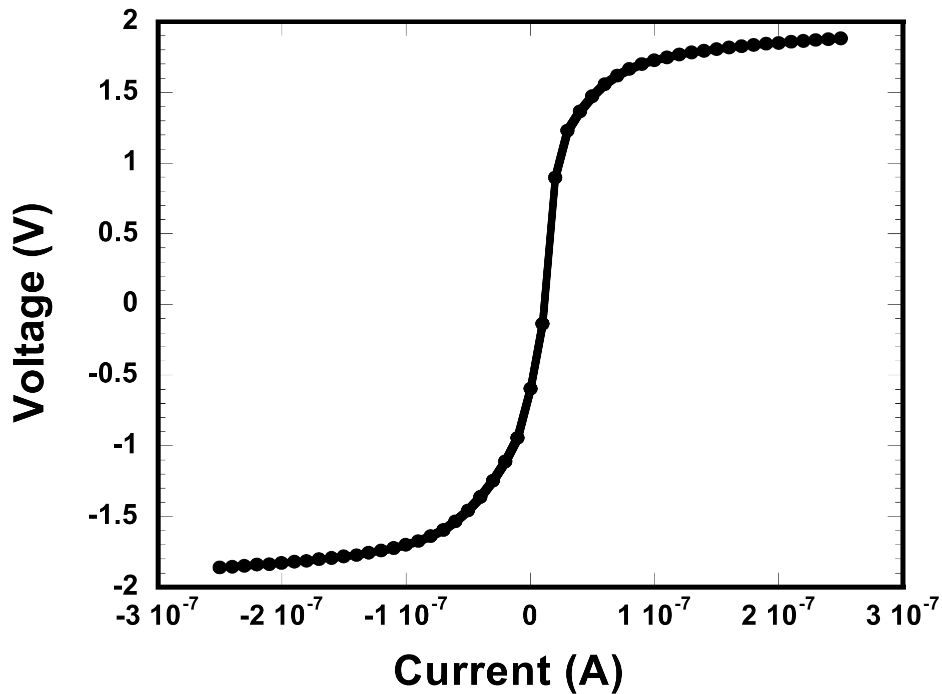

Figure 6.8 IV characteristic of test YBaCuO microbolometer for a 18-µm-long electrode arm geometry for a 200 Hz frame rate.

6.5 Thermal Conductance (G_{th})

The effective thermal conductance of the detector was calculated using following equations:

$$G_{eff} = G_{th} + G_{rad} - \alpha P_I \tag{6.4}$$

$$\Delta T = \frac{P_I}{G_{eff}} \tag{6.5}$$

where ΔT is the temperature differential due to the power loss caused by current biasing and hence dissipating heat. Also $\Delta T = T - T_o$ can be calculated at each bias point, where $T_o \approx 295$ K.

T is obtained from equation (7) and given as:

$$T = \frac{E_a}{k_B \ln\left(\frac{R}{R_o}\right)} \tag{6.6}$$

where R_o is the resistance at infinite temperature obtained from intercept from Fig. 6.5 and Fig. 6.6.

Substituting the values obtained for ΔT at each bias point and that of P_I obtained as in Fig. 6.9 (electrode arms based on 30 Hz frame rate) and in Fig. 6.10 (electrode arms based on 200 Hz frame rate) into the following equation to obtain G_{eff}:

$$G_{eff} = \frac{P_I}{\Delta T} \tag{6.7}$$

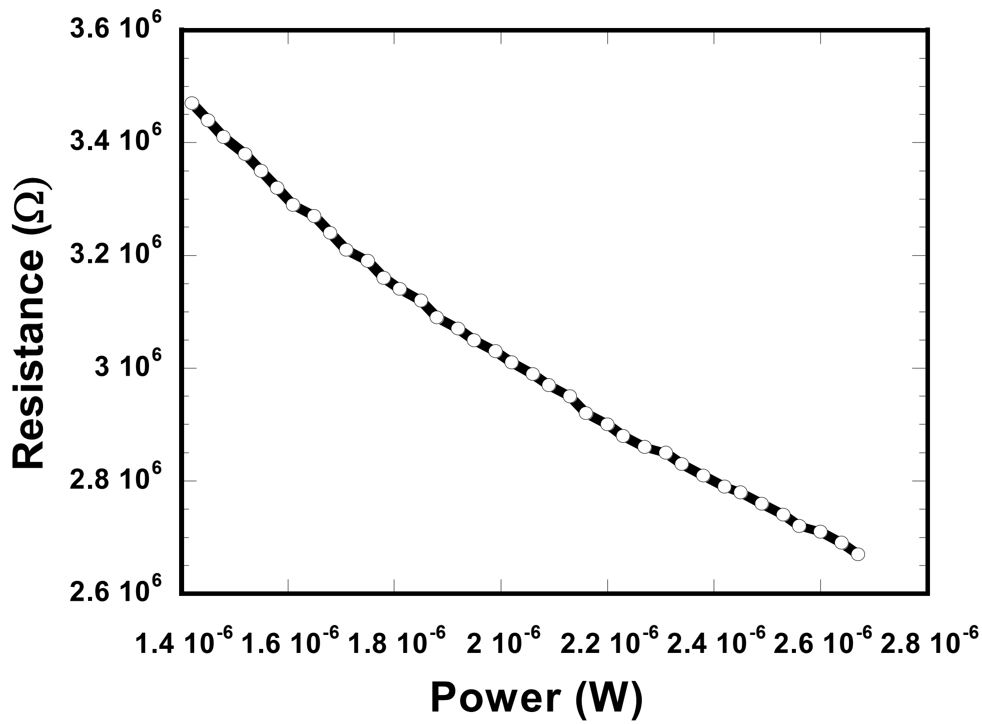

Figure 6.9 Resistance versus Power plot of test bolometer to find effective thermal conductance G_{eff} for the 75-µm-long electrode arm geometry for a 30 Hz frame rate.

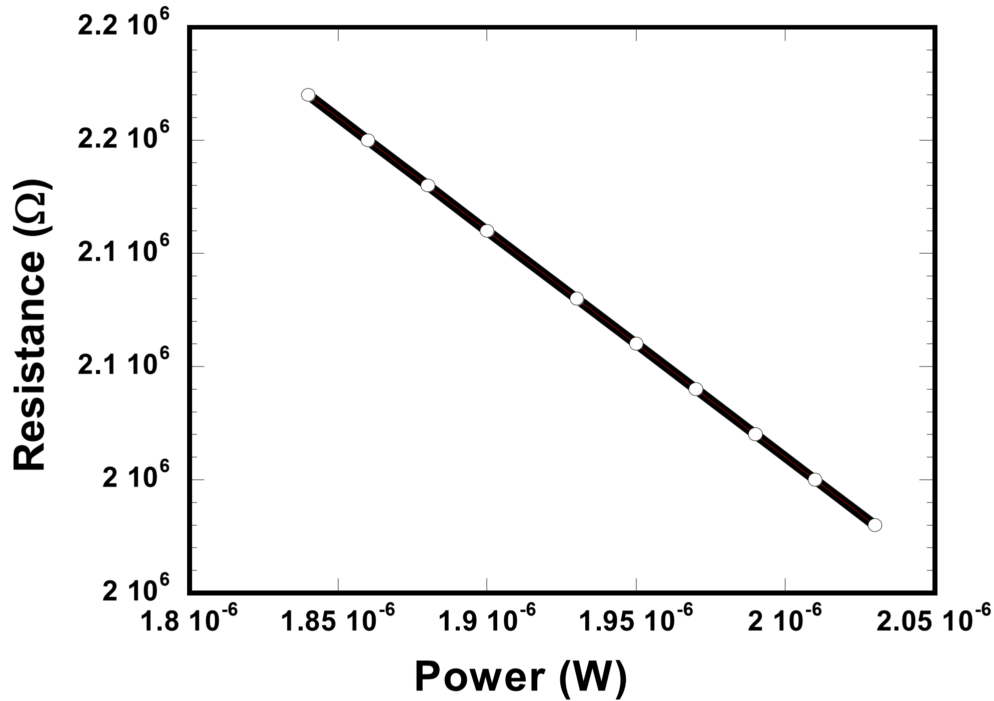

Figure 6.10 Resistance versus Power plot of test bolometer to find effective thermal conductance G_{eff} for the 18-µm-long electrode arm geometry for a 200 Hz frame rate.

From Fig. 6.9, for the 75-µm-long electrode arm geometry for a 30 Hz frame rate, the measured value of effective thermal conductance is 1.37×10^{-7} W/K which is close to the theoretical value of $G_{eff} = 3.66 \times 10^{-7}$ W/K. The thermal conductance G_{th} is calculated from the following equation

$$G_{th} = G_{eff} - G_{rad} + \alpha P_I \tag{6.8}$$

The measured value of the thermal conductance G_{th} is 1.01×10^{-7} W/K which is also close to the theoretical value of 2.92×10^{-7} W/K. The design value is in close agreement with the measured value for the 75-µm-long electrode arm geometry for a 30 Hz frame rate. In this case, the fabricated test microbolometer resistance was obtained as 3.6 MΩ as compared to the expected value of 1 MΩ microbolometer resistance.

From Fig. 6.10, for the 18-µm-long electrode arm geometry for a 200 Hz frame rate, the measured value of effective thermal conductance is 1.2×10^{-7} W/K which is significantly low as compared to the theoretical value of 2.51×10^{-6} W/K. The measured value of the thermal conductance G_{th} is 1.07×10^{-7} W/K which is significantly low as compared to the theoretical value of 2.43×10^{-6} W/K. In this case, the fabricated test microbolometer resistance was obtained as 20.1 MΩ as compared to the expected value of 1 MΩ microbolometer resistance.

6.6 Responsivity (R_v), Detectivity (D*) and Thermal Time Constant (τ_{th})

The optical response involved responsivity (R_v) and detectivity (D*) measurements of the self-supporting semiconducting YBaCuO microbolometer detector array using an IR Blackbody as the broadband IR emitting source. As mentioned earlier, the YBaCuO microbolometers based on self-supporting structure were integrated with CMOS readout circuit using CCBDI (Constant Current Buffered Direct Injection) design technique in AMI 1.5 μm double-poly-double-metal n-well 2.5V CMOS technology.

The fabricated die is first bonded inside the package of 0.5x0.5 cm^2 (Fig. 6.11) comprising self-supporting YBaCuO microbolometers fabricated and integrated with CCBDI readout circuitry and test circuits.

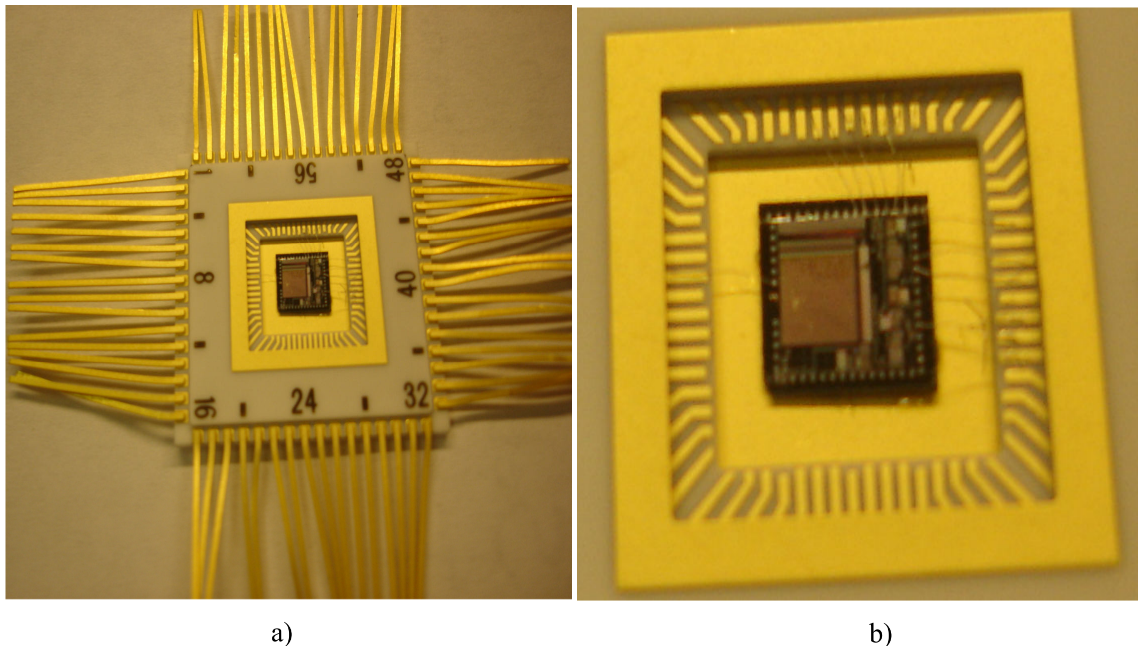

a) b)

Figure 6.11 (a) Bonded packaged die of 0.5x0.5 cm^2 comprising self-supporting YBaCuO microbolometers fabricated and integrated with the CCBDI readout circuitry and test circuits. (b) Closer view of the bonded packaged die.

The Unitcell and a 4x4 microbolometer pixel array with pixel size of 31x31 μm^2, as bonded packaged die, mounted inside the cryostat was illuminated using an IR blackbody source with ZnSe (zinc-selenide) window. The frequency chopper was used to modulate the infrared incident on the microbolometer array. A bias box comprising of biasing circuit was used to bias the microbolometer detector and microbolometer reference detector with ±1V respectively and the rest of the readout circuit was biased separately with ±2.5V supply voltages. Also 2.5V was used to bias the clock. Preamplifier was used with appropriate gain to amplify the signal response from the microbolometer at a chopped frequency. HP 3562A dynamic signal analyzer was used for capturing the data. Vacuum in the cryostat was 10 mT. Distance between infrared blackbody source and frequency chopper was kept at 3.5 inches, while the distance between frequency chopper and detector was 5 inches. Fig. 6.12 shows the measurement set up for responsivity and detectivity versus chopper frequency.

The reason of using ZnSe window is that ZnSe is a clear yellow polycrystalline material with a grain size of approximately 70 µm, transmits IR radiation in the range 0.5-15 µm and it is essentially free of extrinsic impurity absorptions, providing extremely low bulk losses.[65]

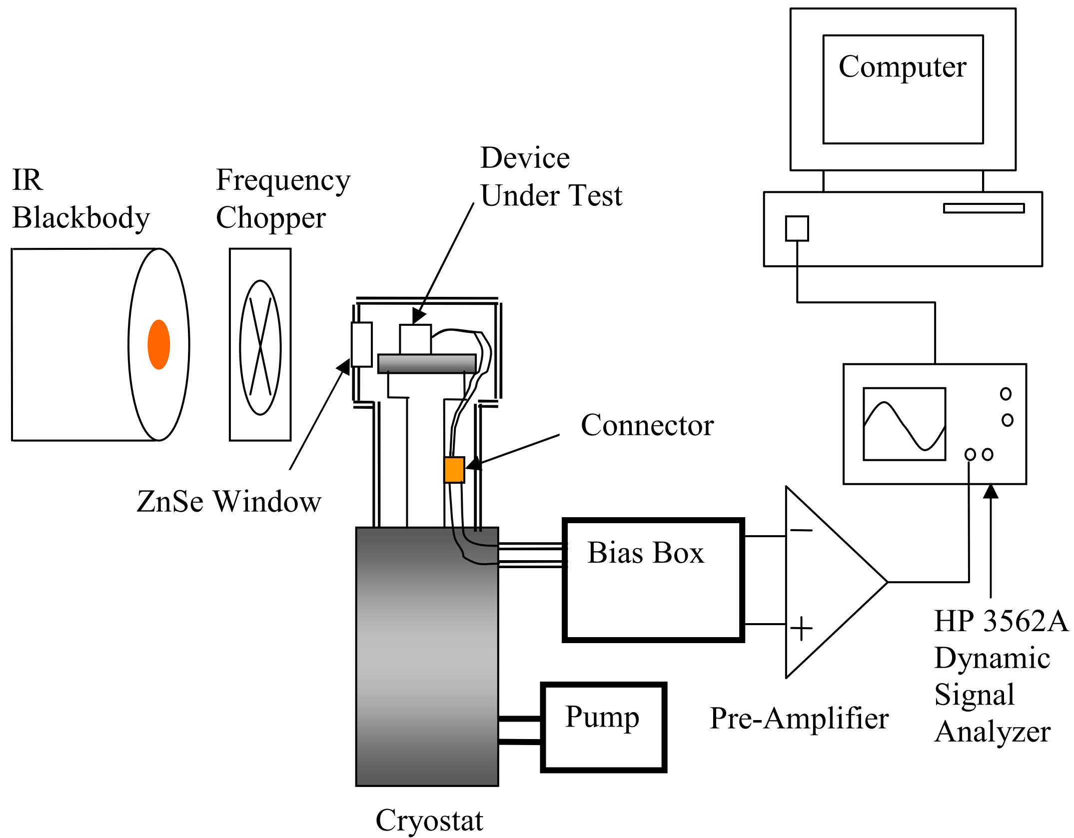

Figure 6.12 Measurement set up for responsivity (R_v) and detectivity (D*) versus chopper frequency.

Three different devices as shown below are characterized for responsivity and detectivity measurement of YBaCuO microbolometers from the Unitcell and a 4x4 array CCBDI readout circuit for a 200 Hz frame with the 18-µm-long electrode arm geometry. The preamplifier gain that amplified the signal response from the microbolometer at a chopped frequency has been nullified in all final results.

A. Device # 1

- DEVICE200A1 for the 4x4 array for a 200Hz frame rate

B. Device # 2

- DEVICE200A2 for the 4x4 array for a 200Hz frame rate
- DEVICE200UC2 for the Unitcell for a 200Hz frame rate

C. Device # 3

- DEVICE30A3 for the 4x4 array for a 30Hz frame rate
- DEVICE30UC3 for the Unitcell for a 30Hz frame rate

A. Device # 1

The incident power on the YBaCuO microbolometer detector was calibrated using Oriel 70124 Pyroelectric detector in similar measurement set up for twenty two different signal responses over chopper frequency range of 1 to 550 Hz (Fig. 6.13).

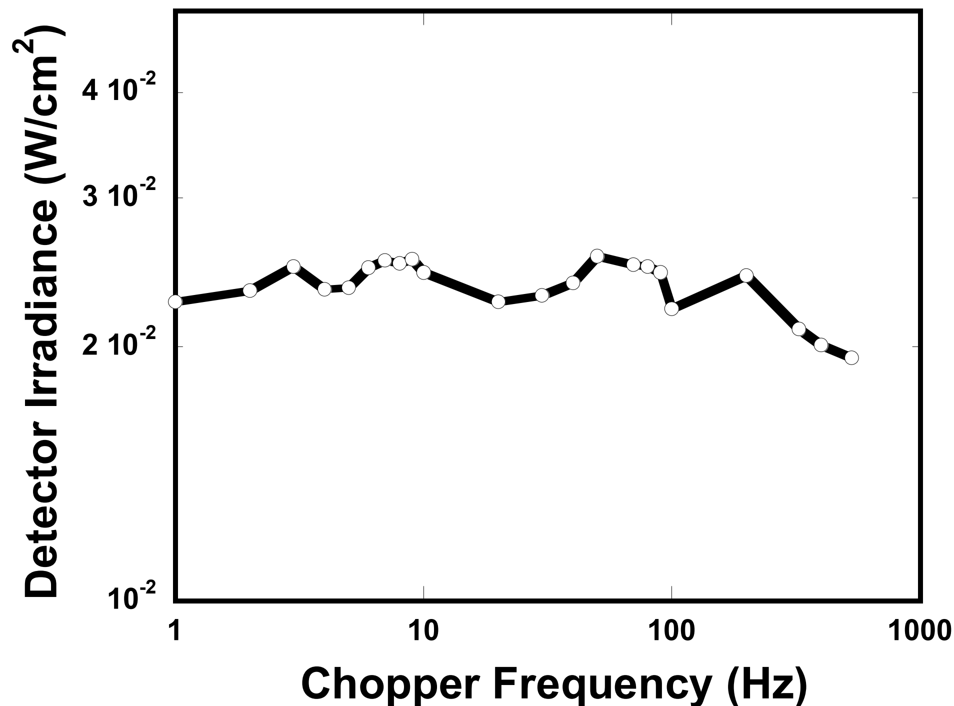

Figure 6.13 Detector irradiance versus chopper frequency using Pyroelectric detector.

The Pyroelectric detector had specification of 5 mm diameter with responsivity of 1000 V/W.

Fig. 6.14 shows the dc transfer characteristic of a single YBaCuO microbolometer pixel for the measured and simulated output from row 1 and column 1 of the 4x4 array CCBDI readout circuit for a 200 Hz frame rate of the DEVICE200A1. Without using IR blackbody source, the supply voltages were biased as VDD = +2.5 V and VSS = -2.5 V and VDDA biased with constant +0.5 V, while VSSA is swept from -2.4 V to +1 V to obtain the dc transfer characteristic. The clock for row and column shift registers to select a single microbolometer pixel from the 4x4 array was biased with -2.5 V.

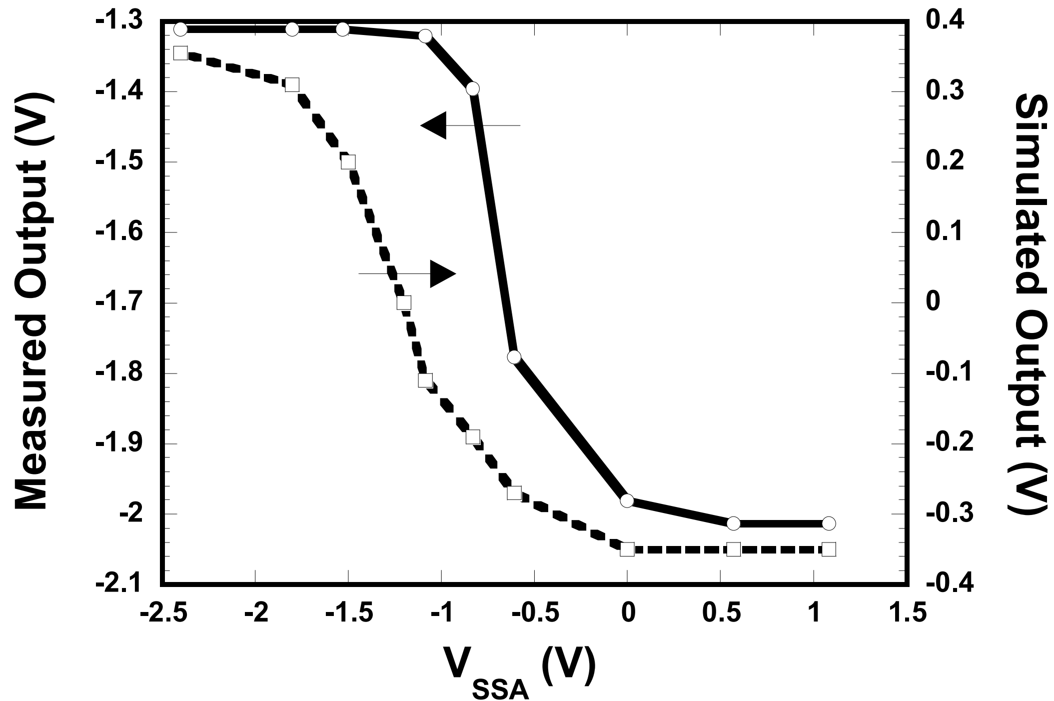

Figure 6.14 DC transfer characteristic of a single YBaCuO microbolometer pixel with V_{DDA} = +0.5 V for the measured and simulated output from row 1 column 1 of the 4x4 array CCBDI readout circuit for a 200 Hz frame rate of the DEVICE200A1.

Fig. 6.14 shows that the dc offset is present in the dc transfer characteristic of the single YBaCuO microbolometer pixel owing to the after fabrication affect on the CCBDI amplifier transfer characteristic. In the linear range of the dc characteristic where at a V_{SSA} voltage, the output voltage of the YBaCuO microbolometer is high. Thus by biasing the microbolometer detector and reference microbolometer detector as V_{DDA} = +0.5 V and V_{SSA} = -0.5 V, the higher responsivity and detectivity can be achieved.

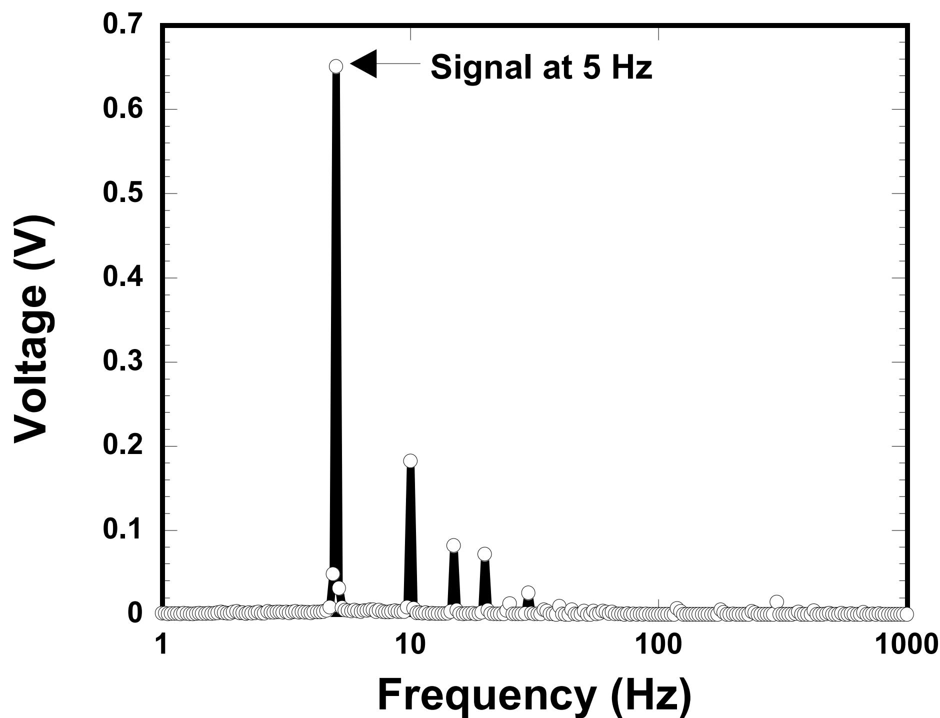

Figure 6.15 Output voltage signal response versus frequency of IR radiation chopped at 5 Hz of a single YBaCuO microbolometer pixel from row 1 column 1 of the 4x4 array CCBDI readout circuit for a 200 Hz frame rate of the DEVICE200A1.

In this particular case of biasing the 4x4 microbolometer pixel array using the bias box, the microbolometer detector and reference microbolometer detector were biased as V_{DDA}= +1 V and V_{SSA} = -1 V respectively and supply voltages were biased as

V_{DD} = +2.5 V and V_{SS} = -2.5 V. The clock for row and column shift registers to select single pixel from row 1 and column 1 of the 4x4 array was biased with 2.5 V. Fig. 6.15 and Fig. 6.16 respectively show the output voltage and noise voltage response versus frequency of IR radiation chopped at 5 Hz of a single YBaCuO microbolometer pixel from row 1 and column 1 of the 4x4 array CCBDI readout circuit for a 200 Hz frame rate of the DEVICE200A1.

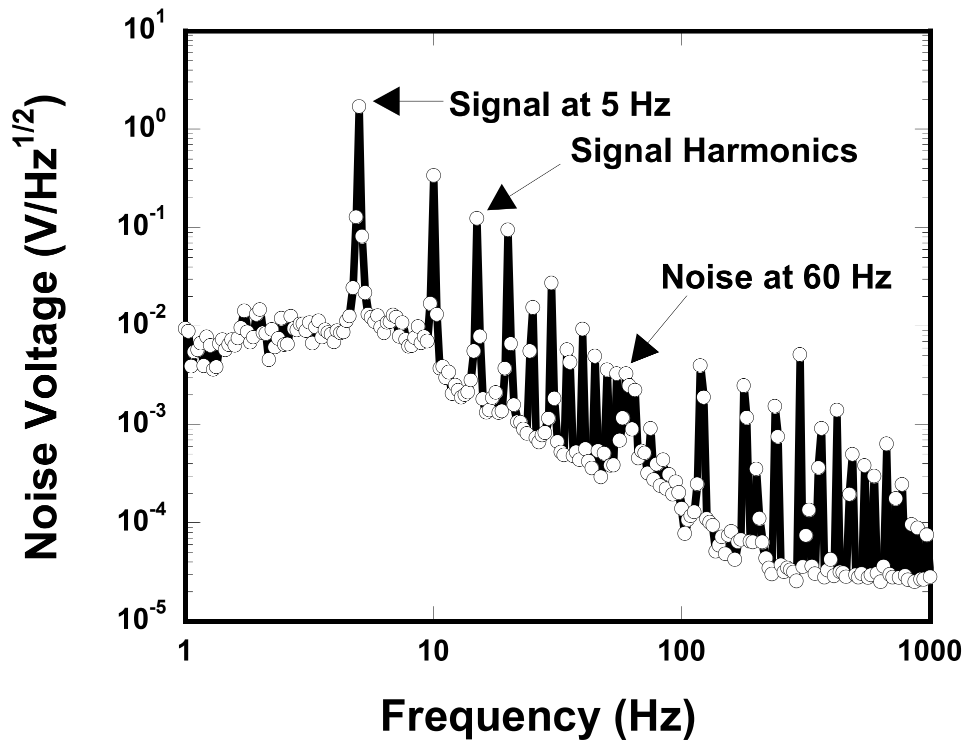

Figure 6.16 Noise voltage signal response versus frequency of IR radiation chopped at 5 Hz of a single YBaCuO microbolometer pixel from row 1 column 1 of the 4x4 array CCBDI readout circuit for a 200 Hz frame rate of the DEVICE200A1.

In responsivity and detectivity measurements, the attenuation of ZnSe window is taken into consideration. The responsivity measurements were taken first with ZnSe window in vacuum, then second measurement involved ZnSe window in air and the

final measurement was no ZnSe window in air. The transmittance ratio due to the loss accrued through ZnSe window was multiplied with the incident power of YBaCuO. This results in decrease in the detector irradiance (Fig. 6.13) by the transmittance ratio and hence further results in increase in responsivity and detectivity. Fig. 6.17 shows responsivity and detectivity response versus chopper frequency for twenty two different signal responses over chopper frequency range of 1 to 550 Hz biased as V_{DDA} = +1 V, V_{SSA} = -1 V of a single YBaCuO microbolometer pixel from row 1 column 1 of the 4x4 array CCBDI readout circuit for a 200 Hz frame rate of the DEVICE200A1.

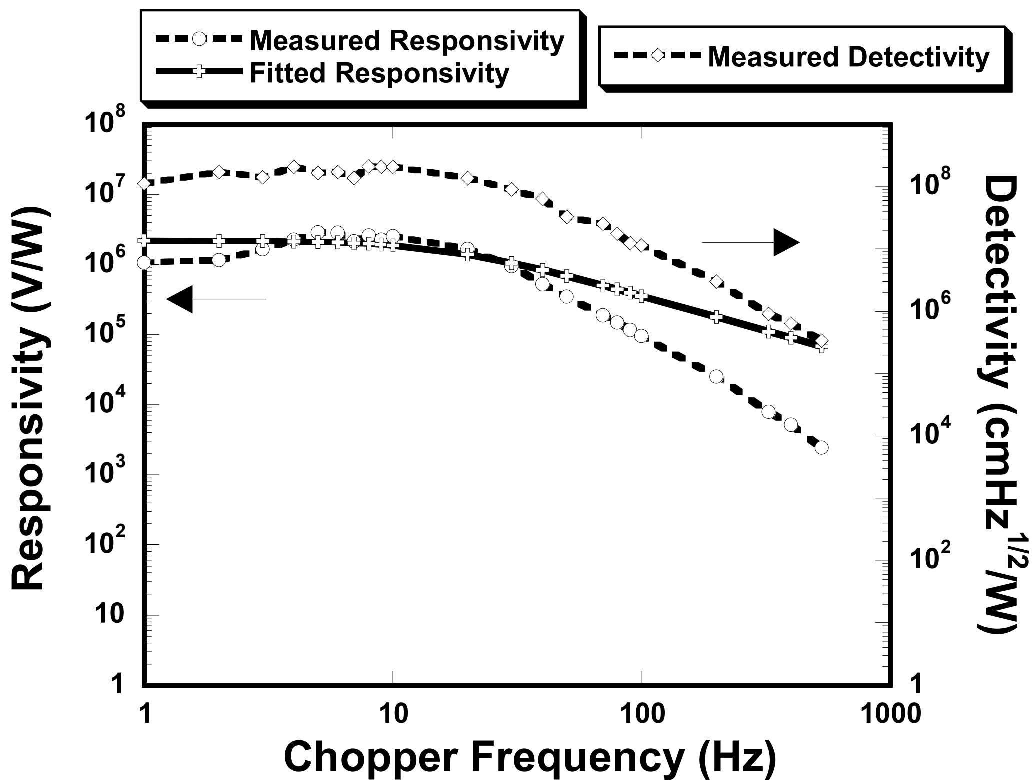

Figure 6.17 Responsivity and Detectivity versus chopper frequency biased as V_{DDA} = +1 V, V_{SSA} = -1 V of a single YBaCuO microbolometer pixel from row 1 column 1 of the 4x4 array CCBDI readout circuit for a 200 Hz frame rate of the DEVICE200A1.

From Fig. 6.17, the maximum responsivity of 2.88×10^6 V/W and maximum detectivity of 2.12×10^8 cmHz$^{1/2}$/W are measured versus chopper frequency of a single YBaCuO microbolometer pixel from row 1 column 1 of the 4x4 array CCBDI readout circuit (microbolometer pixel size of 31x31 μm^2) for a 200 Hz frame rate with the 18-μm-long electrode arm geometry of the DEVICE200A1. Fig. 6.17 also shows the fitted responsivity which is obtained from least square fitting (equation 6.9) in excel using the solver. The maximum fitted responsivity of 2.2×10^6 V/W is obtained. The thermal time constant τ_{th} is obtained as 9.73 ms. The design thermal time constant is 0.42 ms.

$$R_V(f) = \frac{R_{\max}}{\sqrt{\left(1+\omega^2 \tau_{th}{}^2\right)}} \tag{6.9}$$

Next, a long pass filter LP-2500 transmitting IR radiation in the range 2.5-15 μm was used to measure responsivity and detectivity. Fig. 6.18 shows responsivity and detectivity response versus chopper frequency using LP-2500 for thirteen different signal responses over chopper frequency range of 1 to 100 Hz biased as V_{DDA} = +1 V, V_{SSA} = -1 V of a single YBaCuO microbolometer pixel from row 1 column 1 of the 4x4 array CCBDI readout circuit for a 200 Hz frame rate of the DEVICE200A1. The incident power on the YBaCuO microbolometer with LP-2500 was calibrated using Oriel 70124 Pyroelectric detector. The signal appeared to be saturated at higher frequencies because the YBaCuO microbolometer voltage V_{dt} as an input to the CCBDI amplifier lies in the saturation region of the dc transfer characteristic. This results in low readout voltage at the output and hence the preamplifier could not capture peak voltage at higher frequencies. Therefore, the plot shows responsivity and detectivity until 100

Hz range. The maximum responsivity of 1.62×10^5 V/W and maximum detectivity of 3.51×10^7 cmHz$^{1/2}$/W are measured versus chopper frequency using LP-2500 of a single YBaCuO microbolometer pixel from row 1 column 1 of the 4x4 array CCBDI readout circuit for a 200 Hz frame rate with the 18-μm-long electrode arm geometry of the DEVICE200A1. Fig. 6.18 also shows the fitted responsivity which is obtained from least square fitting in excel using the solver. The maximum fitted responsivity of 1.04×10^5 V/W is obtained. The thermal time constant τ_{th} is obtained as 10 ms. The design thermal time constant is 0.42 ms.

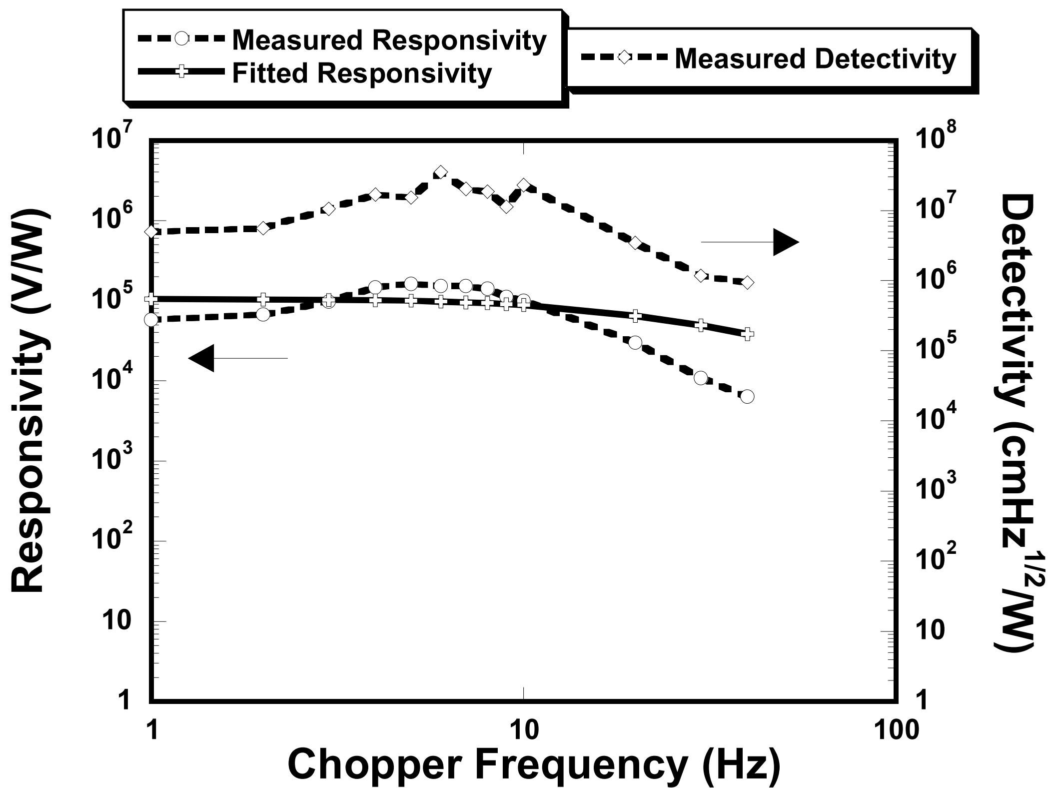

Figure 6.18 Responsivity and Detectivity versus chopper frequency using LP-2500 biased as V_{DDA} = +1 V, V_{SSA} = -1 V of a single YBaCuO microbolometer pixel from row 1 column 1 of the 4x4 array CCBDI readout circuit for a 200 Hz frame rate of the DEVICE200A1.

From the optical response measurement of a single YBaCuO microbolometer pixel from the 4x4 array CCBDI readout circuit for a 200 Hz frame rate with the 18-μm-long electrode arm geometry of the DEVICE200A1, there exists noticeable difference in the responsivity and detectivity values between using ZnSe window and LP-2500 filter. The apparent short wavelength response of the readout lies in the fact that ZnSe window transmits IR radiation in the 0.5-15 μm range, which includes visible light and hence resulting in photoresponse in silicon substrate causing additional signal. Whereas LP-2500 filter transmits only IR radiation in the 2.5-15 μm range and hence gives the short wavelength response of readout. Therefore, it is necessary to consider optical response measurements using LP-2500 filter only.

B. Device # 2

In this particular case of biasing the 4x4 microbolometer pixel array using the bias box, the microbolometer detector and microbolometer reference detector were biased as V_{DDA}= +1 V and V_{SSA} = -1 V and also in second case as V_{DDA}= +0.5 V and V_{SSA} = -0.5 V respectively and supply voltages were biased as V_{DD} = +2.5 V and V_{SS} = -2.5 V. The clock for row and column shift registers to select single pixel from row 1 and column 1 of the 4x4 array was biased with 2.5 V.

Fig. 6.19 shows responsivity and detectivity response versus chopper frequency using LP-2500 biased as V_{DDA}= +1 V and V_{SSA} = -1 V (shown as 1V), and V_{DDA}= +0.5 V and V_{SSA} = -0.5 V (shown as 0.5V) of a single YBaCuO microbolometer pixel from row 1 column 1 of the 4x4 array CCBDI readout circuit for a 200 Hz frame rate of the DEVICE200A2. The incident power on the YBaCuO microbolometer with LP-2500

was calibrated using Oriel 70124 Pyroelectric detector. The maximum responsivity of 6.75×10^4 V/W and maximum detectivity of 6.3×10^6 cmHz$^{1/2}$/W are measured versus chopper frequency using LP-2500 biased as V_{DDA}= +1 V and V_{SSA} = -1 V. The maximum responsivity of 6.18×10^4 V/W and maximum detectivity of 5.56×10^6 cmHz$^{1/2}$/W are measured versus chopper frequency using LP-2500 biased as V_{DDA}= +0.5 V and V_{SSA} = -0.5 V of a single YBaCuO microbolometer pixel from the 4x4 array CCBDI readout circuit for a 200 Hz frame rate with the 18-µm-long electrode arm geometry of the DEVICE200A2.

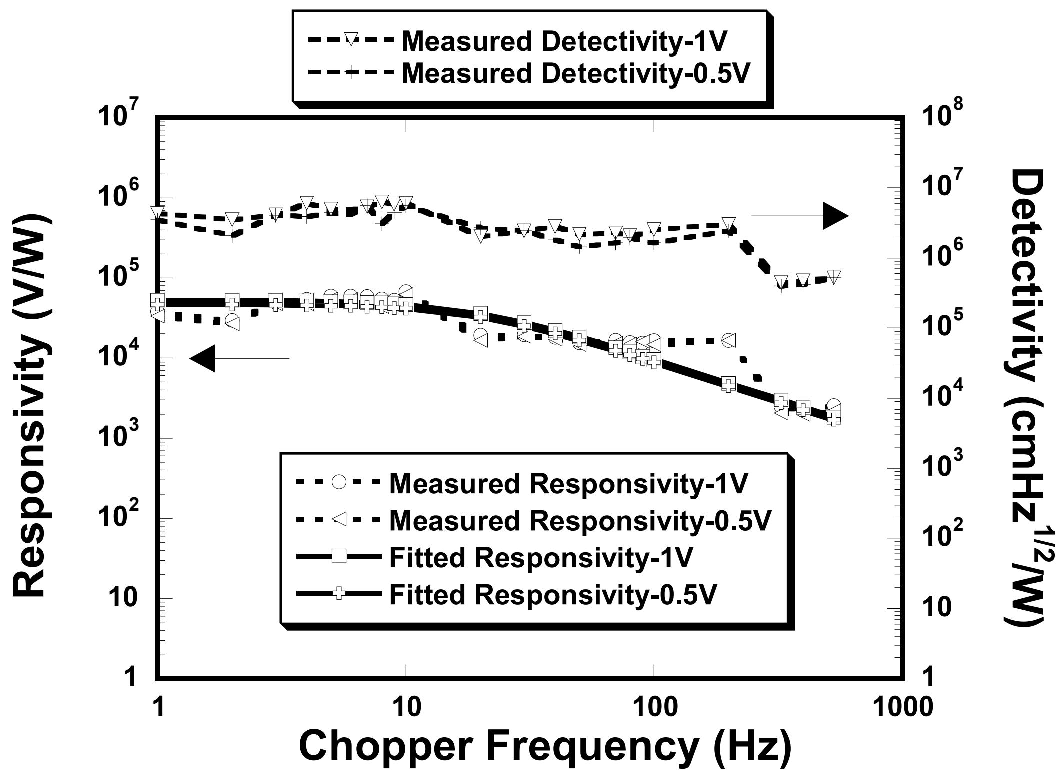

Figure 6.19 Responsivity and Detectivity versus chopper frequency using LP-2500 biased as V_{DDA} = +1 V, V_{SSA} = -1 V (shown as 1V), and V_{DDA} = +0.5 V, V_{SSA} = -0.5 (shown as 0.5V) of a single YBaCuO microbolometer pixel from row 1 column 1 of the 4x4 array CCBDI readout circuit for a 200 Hz frame rate of the DEVICE200A2.

Fig. 6.19 also shows the fitted responsivity which is obtained from least square fitting in excel using the solver. For V_{DDA}= +1 V and V_{SSA} = -1 V biasing (shown as 1V), the maximum fitted responsivity of 5.33x10^4 V/W is obtained. The thermal time constant τ_{th} is obtained as 8.7 ms. For V_{DDA}= +0.5 V and V_{SSA} = -0.5 V biasing (shown as 0.5V), the maximum fitted responsivity of 4.68x10^4 V/W is obtained. The thermal time constant τ_{th} is obtained as 8.28 ms. The design thermal time constant is 0.42 ms.

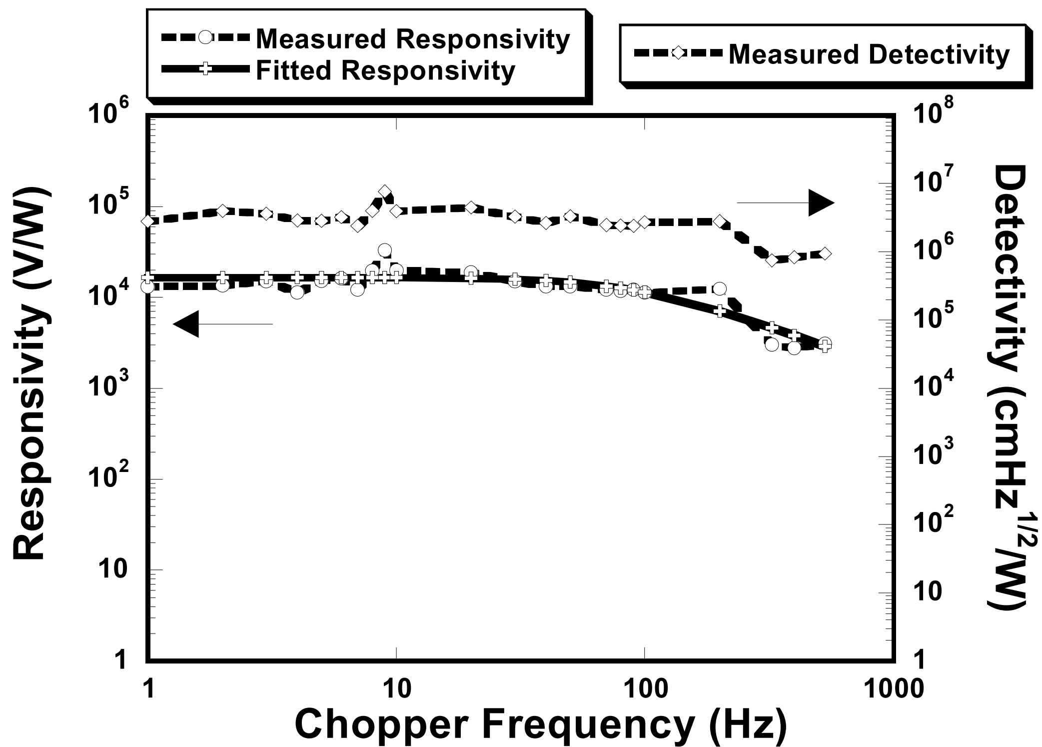

Figure 6.20 Responsivity and Detectivity versus chopper frequency using LP-2500 biased as V_{DDA} = +1 V, V_{SSA} = -1 V of a single YBaCuO microbolometer pixel from the Unitcell CCBDI readout circuit for a 200 Hz frame rate of the DEVICE200UC2.

Fig. 6.20 shows responsivity and detectivity response versus chopper frequency using LP-2500 biased as V_{DDA} = +1V, V_{SSA} = -1V of a single YBaCuO microbolometer

pixel from the Unitcell CCBDI readout circuit for a 200 Hz frame rate of the DEVICE200UC2. The maximum responsivity of 3.3×10^4 V/W and maximum detectivity of 7.69×10^6 cmHz$^{1/2}$/W are measured versus chopper frequency using LP-2500 of a single YBaCuO microbolometer pixel from the Unitcell CCBDI readout circuit for a 200 Hz frame rate with the 18-μm-long electrode arm geometry of the DEVICE200UC2. The maximum fitted responsivity of 1.66×10^4 V/W is obtained. The thermal time constant τ_{th} is 1.69 ms. The design thermal time constant is 0.42 ms.

C. Device # 3

Device # 3 is characterized for responsivity and detectivity measurement of YBaCuO microbolometers using LP-2500 from the Unitcell and a 4x4 array CCBDI readout circuit for a 30 Hz frame with the 75-μm-long electrode arm geometry. The preamplifier gain that amplified the signal response from the microbolometer at a chopped frequency has been nullified in all the final results. The incident power on the YBaCuO microbolometer has been calibrated using Oriel 70124 Pyroelectric detector for twenty two different signal responses over chopper frequency range of 1 to 550 Hz.

In this particular case of biasing the 4x4 microbolometer pixel array using the bias box, the microbolometer detector and reference microbolometer detector were biased as V_{DDA}= +1 V and V_{SSA} = -1 V respectively and supply voltages were biased as V_{DD} = +2.5 V and V_{SS} = -2.5 V. The clock for row and column shift registers to select single pixel from row 1 and column 1 of the 4x4 array was biased with 2.5 V.

Fig. 6.21 shows responsivity and detectivity response versus chopper frequency using LP-2500 biased as V_{DDA} = +1 V, V_{SSA} = -1 V of a single YBaCuO pixel

microbolometer from row 1 column 1 of the 4x4 array CCBDI readout circuit for a 30 Hz frame rate of the DEVICE30A3. The maximum responsivity of 1.24×10^5 V/W and maximum detectivity of 1.03×10^7 cmHz$^{1/2}$/W are measured versus chopper frequency using LP-2500 of a single YBaCuO microbolometer pixel from row 1 column 1 of the 4x4 array CCBDI readout circuit for a 30 Hz frame rate with the 75-µm-long electrode arm geometry of the DEVICE30A3.

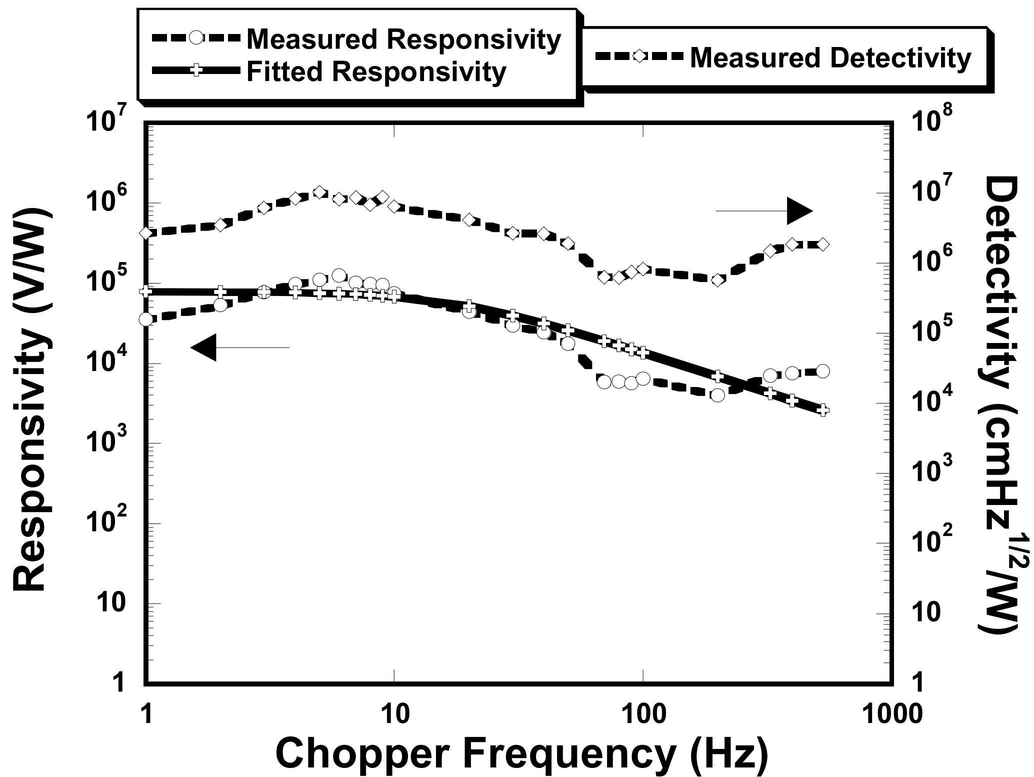

Figure 6.21 Responsivity and Detectivity versus chopper frequency using LP-2500 biased as V_{DDA} = +1 V, V_{SSA} = -1 V of a single YBaCuO microbolometer pixel from row 1 column 1 of the 4x4 array CCBDI readout circuit for a 30 Hz frame rate of the DEVICE30A3.

Fig. 6.21 also shows the fitted responsivity which is obtained from least square fitting in excel using the solver. The maximum fitted responsivity of 7.86×10^4 V/W is

obtained. The thermal time constant τ_{th} is obtained as 9.12 ms. The design thermal time constant is 2.95 ms.

Fig. 6.22 shows responsivity and detectivity response versus chopper frequency using LP-2500 of a single YBaCuO microbolometer pixel from the Unitcell CCBDI readout circuit for a 30 Hz frame rate of the DEVICE30UC3.

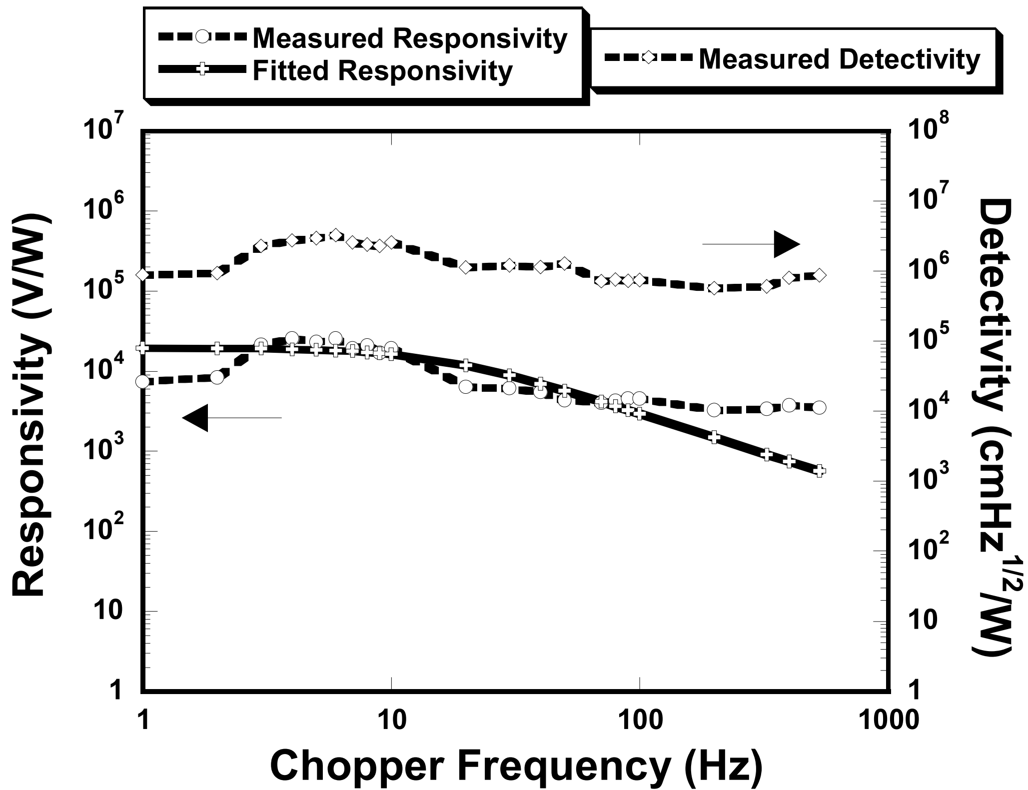

Figure 6.22 Responsivity and Detectivity versus chopper frequency using LP-2500 biased as V_{DDA} = +1 V, V_{SSA} = -1 V of a single YBaCuO microbolometer pixel from the Unitcell CCBDI readout circuit for a 30 Hz frame rate of the DEVICE30UC3.

The maximum responsivity of 2.56×10^4 V/W and maximum detectivity of 3.24×10^6 $cmHz^{1/2}/W$ are measured versus chopper frequency using LP-2500 of a single YBaCuO microbolometer pixel from the Unitcell CCBDI readout circuit for a 30 Hz

frame rate with the 75-μm-long electrode arm geometry of the DEVICE30UC3. The maximum fitted responsivity of 1.94x10^4 V/W is obtained. The thermal time constant τ_{th} is obtained as 10.4 ms. The design thermal time constant is 2.95 ms.

Now by biasing the microbolometer detector and microbolometer reference detector as V_{DDA} = +2.5 V and V_{SSA} = -0.5V, the higher responsivity and detectivity can be achieved.

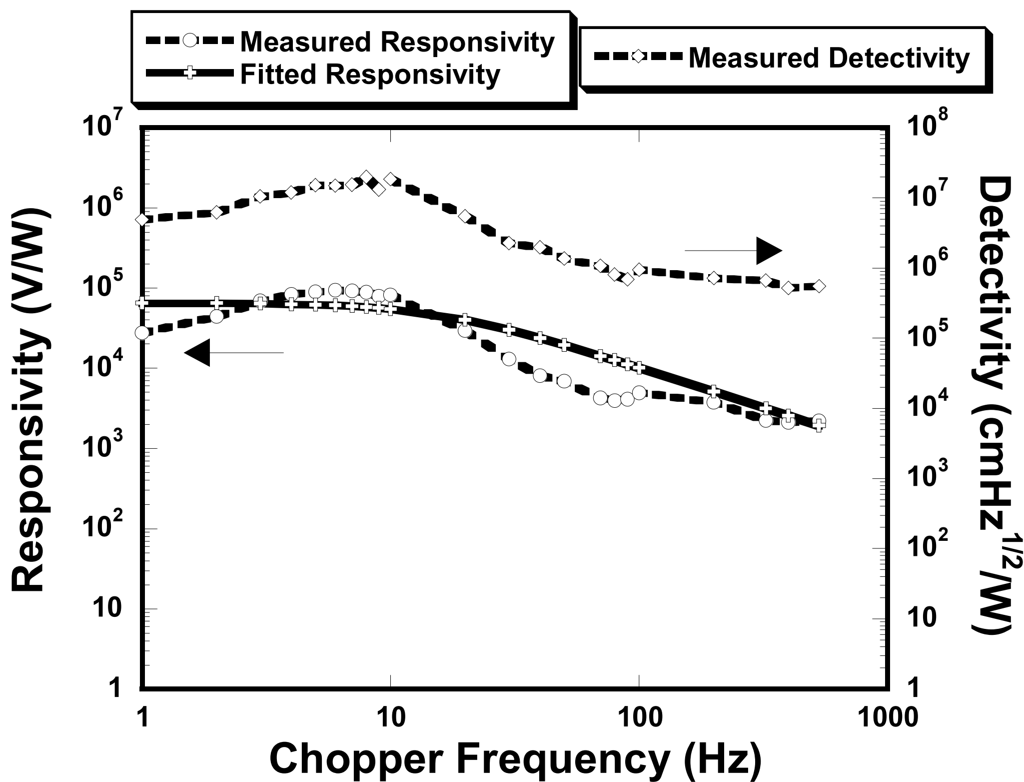

Figure 6.23 Responsivity and Detectivity versus chopper frequency using LP-2500 biased as V_{DDA} = +2.5 V, V_{SSA} = -0.5 V of a single YBaCuO microbolometer pixel from row 1 column 3 of the 4x4 array CCBDI readout circuit for 30 Hz frame rate of the DEVICE30A3.

Fig. 6.23 shows responsivity and detectivity response versus chopper frequency using LP-2500 biased as V_{DDA} = +2.5 V, V_{SSA} = -0.5 V of a single YBaCuO microbolometer pixel from row 1 column 3 of the 4x4 array CCBDI readout circuit for

a 30 Hz frame rate of the DEVICE30A3. The maximum responsivity of 9.48×10^4 V/W and maximum detectivity of 1.98×10^7 cmHz$^{1/2}$/W are measured versus chopper frequency using LP-2500 of a single YBaCuO microbolometer pixel from the 4x4 array CCBDI readout circuit for a 30 Hz frame rate with the 75-µm-long electrode arm geometry of the DEVICE30A3. The maximum fitted responsivity of 6.54×10^4 V/W is obtained. The thermal time constant τ_{th} is obtained as 10.2 ms. The design thermal time constant is 2.95 ms.

6.7 Conclusions

The chapter presents the microbolometer characterization for the fabricated self-supporting YBaCuO microbolometers as test microbolometers, and for the integrated CCBDI amplifier and microbolometer in the Unitcell and a 4x4 array CCBDI readout circuit. This includes the measurements of figures of merit, and optical and thermal characterization carried out in the microsensors laboratory at NanoFab Center.

The microbolometer characterization included the measurements of temperature dependent resistance R(T), temperature coefficient of resistance (TCR), activation energy (E_a), current-voltage (IV) characteristic, thermal conductance (G_{th}), responsivity (R_v), detectivity (D*) and thermal time constant (τ_{th}).

The characterization measurements of R(T), TCR, E_a, IV and G_{th} were performed on the YBaCuO test microbolometer pixel with the pixel size of 31x31 µm^2 for the 75-µm-long electrode arm geometry for a 30 Hz frame rate and for the 18-µm-long electrode arm geometry for a 200 Hz frame rate. The measured TCR was -3.16 %/K at 295K and measured value of thermal conductance G_{th} was 1.01×10^{-7} W/K for a

30Hz frame rate. And for a 200Hz frame rate, the measured TCR was -2.9 %/K at 295K and measured value of G_{th} was $1.07x10^{-7}$ W/K. These measured values confirm the high temperature coefficient resistance and low thermal conductance of semiconducting YBaCuO microbolometer, thus provide good thermal isolation from the substrate, which in turn offer higher sensitivity resulting in increased responsivity. Table 6.1 presents a summary of results for the two different electrode arm geometries.

Table 6.1 Summary of results for the two different electrode arm geometries.

Electrode arm geometry	75-µm-long for a 30 Hz frame rate	18-µm-long for a 200 Hz frame rate
Resistance at 295 K	3.6 MΩ	20.1 MΩ
TCR at 295 K	-3.16 %/K	-2.9 %/K
Activation Energy E_a	0.216 eV	0.215 eV
Thermal conductance G_{th}	$1.01x10^{-7}$ W/K	$1.07x10^{-7}$ W/K

The optical response involved responsivity (R_v) and detectivity (D*) measurements of the self-supporting semiconducting YBaCuO microbolometer detector array using an IR blackbody as the broadband IR emitting source. The YBaCuO microbolometers based on self-supporting structure were on-chip integrated with CMOS readout circuit using CCBDI design technique in AMI 1.5 µm double-poly-double-metal n-well 2.5V CMOS technology.

The maximum responsivity of $1.62x10^{5}$ V/W and maximum detectivity of $3.51x10^{7}$ $cmHz^{1/2}/W$ were measured using LP-2500 of a single YBaCuO microbolometer pixel from the 4x4 array CCBDI readout circuit for a 200 Hz frame rate

with the 18-µm-long electrode arm geometry of device. From least square fitting in excel using the solver, maximum fitted responsivity of 1.04×10^5 V/W and the thermal time constant of 10 ms were obtained. The design thermal time constant was 0.42 ms.

The maximum responsivity of 1.24×10^5 V/W and maximum detectivity of 1.03×10^7 $cmHz^{1/2}/W$ were measured using LP-2500 of a single YBaCuO microbolometer pixel from the 4x4 array CCBDI readout circuit for a 30 Hz frame rate with the 75-µm long electrode arm geometry of device. From least square fitting in excel using the solver, maximum fitted responsivity of 7.86×10^4 V/W and the thermal time constant of 9.12 ms were obtained. The design thermal time constant was 2.95 ms.

Tables 6.2, 6.3, 6.4 and 6.5 show a comparison of responsivity, detectivity and thermal time constant for the DEVICE200A1, DEVICE200A2, and DEVICE30A3 with their respective V_{DDA}, V_{SSA} biasing.

Table 6.2 Summary of results for the DEVICE200A1, DEVICE200A2, and DEVICE30A3 with V_{DDA}= +1 V, V_{SSA}= -1 V biasing

Name of Device (Frame rate)	DEVICE200A1 (200 Hz)	DEVICE200A2 (200 Hz)	DEVICE30A3 (30 Hz)
Measured $Responsivity_{max}$ (V/W) (V_{DDA}=+1 V,V_{SSA}=-1 V)	1.62×10^5 (4x4 array)	6.75×10^4 (4x4 array)	1.24×10^5 (4x4 array)
Fitted $Responsivity_{max}$ (V/W) (V_{DDA}=+1 V,V_{SSA}=-1 V)	1.04×10^5 V/W (4x4 array)	5.33×10^4 (4x4 array)	7.86×10^4 (4x4 array)
Measured $Detectivity_{max}$ ($cmHz^{1/2}/W$) (V_{DDA}=+1 V,V_{SSA}=-1 V)	3.51×10^7 (4x4 array)	6.3×10^6 (4x4 array)	1.03×10^7 (4x4 array)
Thermal time constant (ms) (V_{DDA}=+1 V,V_{SSA}=-1 V)	10 (4x4 array)	8.7 (4x4 array)	9.12 (4x4 array)

Table 6.3 Summary of results for the DEVICE200A2 with V_{DDA}= +0.5 V, V_{SSA}= -0.5 V biasing

Name of Device (Frame rate)	DEVICE200A2 (200 Hz)
Measured $Responsivity_{max}$ (V/W) (V_{DDA}=+0.5 V,V_{SSA}=-0.5 V)	6.18×10^4 (4x4 array)
Fitted $Responsivity_{max}$ (V/W) (V_{DDA}=+0.5 V,V_{SSA}=-0.5 V)	4.68×10^4 (4x4 array)
Measured $Detectivity_{max}$ ($cmHz^{1/2}/W$) (V_{DDA}=+0.5 V,V_{SSA}=-0.5 V)	5.56×10^6 (4x4 array)
Thermal time constant (ms) (V_{DDA}=+0.5 V,V_{SSA}=-0.5 V)	8.28 (4x4 array)

Table 6.4 Summary of results for the DEVICE200UC2 and DEVICE30UC3 with V_{DDA}= +1 V, V_{SSA}= -1 V biasing

Name of Device (Frame rate)	DEVICE200UC2 (200 Hz)	DEVICE30UC3 (30 Hz)
Measured $Responsivity_{max}$ (V/W) (V_{DDA}=+1 V,V_{SSA}=-1 V)	3.3×10^4 (Unitcell)	2.56×10^4 (Unitcell)
Fitted $Responsivity_{max}$ (V/W) (V_{DDA}=+1 V,V_{SSA}=-1 V)	1.66×10^4 (Unitcell)	1.94×10^4 (Unitcell)
Measured $Detectivity_{max}$ ($cmHz^{1/2}/W$) (V_{DDA}=+1 V,V_{SSA}=-1 V)	7.69×10^6 (Unitcell)	3.24×10^6 (Unitcell)
Thermal time constant (ms) (V_{DDA}=+1 V,V_{SSA}=-1 V)	1.69 (Unitcell)	10.4 (Unitcell)

Table 6.5 Summary of results for the DEVICE30UC3 with V_{DDA}= +2.5 V, V_{SSA}= -0.5 V biasing

Name of Device (Frame rate)	DEVICE30UC3 (30 Hz)
Measured $Responsivity_{max}$ (V/W) (V_{DDA}=+2.5 V,V_{SSA}=-0.5 V)	$9.48\text{x}10^4$ (4x4 array)
Fitted $Responsivity_{max}$ (V/W) (V_{DDA}=+2.5 V,V_{SSA}=-0.5 V)	$6.54\text{x}10^4$ (4x4 array)
Measured $Detectivity_{max}$ ($cmHz^{1/2}/W$) (V_{DDA}=+2.5 V,V_{SSA}=-0.5 V)	$1.98\text{x}10^7$ (4x4 array)
Thermal time constant (ms) (V_{DDA}=+2.5 V,V_{SSA}=-0.5 V)	10.2 (4x4 array)

From Tables 6.2 and 6.3, after observing the measured thermal time constant of 10 ms for the DEVICE200A1, and 8.7 ms, 8.28 ms for the DEVICE200A2 (with two different V_{DDA} and V_{SSA} biasing) for the 4x4 array for a 200 Hz frame rate, there is minute discrepancy in thermal time constant values. The fitted responsivity of $5.33\text{x}10^4$ V/W for the DEVICE200A2 is almost half of $1.04\text{x}10^5$ V/W for the DEVICE200A1. This is because the microbolometer fabrication process results in some differences in the thickness of thin films, YBaCuO material and polyimide sacrificial layer across the die of $0.5\text{x}0.5cm^2$ and also results in such fabrication differences for different devices like DEVICE200A1 (device # 1) and DEVICE200A2 (device # 2), both fabricated for the 18 μm electrode arm geometry for a 200 Hz frame rate. Therefore, it can result in some differences in their corresponding electrical and optical response including

thermal conductance, thermal mass, responsivity and detectivity, and thermal time constant values.

From Table 6.4, it is observed that between the measured thermal time constant of 1.69 ms for the DEVICE200UC2 (the Unitcell for a 200 Hz frame rate) and of 10.4 ms for the DEVICE30UC3 (the Unitcell for a 30 Hz frame rate) there is a proportionality factor of around 5, which correctly corresponds to that of the design thermal time constant of 0.42 ms for a 200 Hz frame rate and 2.95 ms for a 30 Hz frame rate. However, observing Table 6.2 and comparing likewise, it is found that between the measured thermal time constant of 8.7 ms for the DEVICE200A2 (the 4x4 array for a 200 Hz frame rate) and of 10.4 ms for the DEVICE30A3 (the 4x4 array for a 30 Hz frame rate), there is a significant difference in the proportionality factor. The obvious reason for this difference lies in the fact that the fitted responsivity value and their corresponding ratio of 5.33×10^4 V/W for the DEVICE200A2 and of 7.86×10^4 V/W for the DEVICE30A3 is quite high as compared to the fitted responsivity and their corresponding ratio of 1.66×10^4 V/W for the DEVICE200UC2 and of 1.94×10^4 V/W for the DEVICE30UC3. The higher responsivity values and the ratio between those of DEVICE200A2 and DEVICE30A3 means low thermal conductance and considering the same thermal mass, it results in higher values of thermal time constant and therefore causes significant difference in the proportionality factor between their measured thermal time constant values.

Table 6.6 presents the technical specifications of the three state-of-art uncooled VO_x microbolometer models made by DRS Infrared Technologies.[66]

Table 6.6 Technical specifications of the three DRS's VO_x microbolometer models

Technical Specifications	DRS's VO_x Models	U6000	U3000	M3500
Focal Plane Array	Array Size	640x480	320x240	320x240
	Detector Pitch (µm)	25.4x25.4	51x51	25.4x25.4
	Spectral Response (µm)	8-12	8-12	8-12
Video	Frame Rate (Hz)	30	60	60
Environmental	Operating Temperature (^{0}C)	-20 to +60	-20 to +60	-20 to +49

Table 6.7 presents the technical specifications of the DEVICE200A1, DEVICE200A2, and DEVICE30A3 fabricated for this dissertation research project comparing with Table 6.6.

Table 6.7 Technical specifications of the DEVICE200A1, DEVICE200A2 and DEVICE30A3

Technical Specifications		DEVICE 200A1	DEVICE 200A2	DEVICE 30A3
Focal Plane Array	Array Size	4x4	4x4	4x4
	Detector Pitch (µm)	31x31	31x31	31x31
	Spectral Response (µm)	2.5-15	2.5-15	2.5-15
Video	Frame Rate (Hz)	200	200	30
Environmental	Operating Temperature (^{0}C)	-73 to + 52	-73 to + 52	-73 to + 52

The comparison between Table 6.6 and Table 6.7 shows that with respect to the technical specifications of the state-of-art VO_x microbolometer models, this dissertation research project improves the performance of uncooled IR cameras by a higher frame rate of 200 Hz for a 640x480 array (extrapolated from the 4x4 array CCBDI readout circuit) for faster thermal imaging in commercial, military and biomedical applications as a novel approach for being designed, fabricated and on-chip integrated with the self-supporting semiconducting YBaCuO microbolometers.

CHAPTER 7

SUMMARY AND CONCLUSIONS

YBaCuO (Yttrium Barium Copper Oxide) microbolometers based on self-supporting structure have been designed, fabricated, on-chip integrated and characterized as a novelty with the Unitcell and a 4x4 array CCBDI (Constant Current Buffered Direct Injection) readout circuit in AMI 1.5 µm double-poly-double-metal n-well 2.5V CMOS technology. The CCBDI (Constant Current Buffered Direct Injection) readout circuit is designed to work with a traditional frame rate of 30 Hz and as a novel approach improves the performance of uncooled IR cameras by a higher frame rate of 200 Hz for a 640x480 array for faster thermal imaging in commercial, military and biomedical applications. The 18-µm-long electrode arm geometry of YBaCuO microbolometer provides a higher frame rate of 200 Hz and hence meets the design compatibility requirement for the faster 200 Hz frame rate by the CCBDI readout circuit. The self-supporting semiconducting YBaCuO micromachined microbolometers have found an attractive application for thermal detection. By not requiring cryogenic cooling, the self-supporting semiconducting YBaCuO microbolometers have emerged as an alternative to cryogenically cooled photon detectors for the infrared detection and thus resulting in substantial reduction in system cost, size, weight, power consumption and mission time. The lower thermal conductance of the microbolometers to the substrate provides good sensitivity for the infrared detection. The 75-µm-long electrode

arm geometry is designed to achieve a traditional 30 Hz frame rate. The CCBDI readout circuit offers advantages of high linearity and uniformity, low offset error, provides maximum sensitivity at a bias current and has a great potential in the application of large uncooled bolometer focal plane arrays. The CCBDI readout is a better performance circuit as compared to other designs due to increase in the injection efficiency of the CCBDI amplifier and the stable detector bias control. The merits of YBaCuO include relatively high temperature coefficient of resistance, relatively low 1/f-noise, the ease of fabrication by rf magnetron sputtering, room temperature operation and usage of micromachining technology. The self-supporting YBaCuO exhibit low thermal mass and hence provides low thermal time constant for the same degree of thermal isolation. The thermal isolation of the microbolometers was varied by designing two different electrode arm geometries.

The TCR of -3.16 %/K was measured at 295 K and the measured value of G_{th} was 1.01×10^{-7} W/K for a 30 Hz frame rate for a YBaCuO test microbolometer with the pixel size of 31x31 μm^2. Similarly, for a 200 Hz frame rate, the TCR of -2.9 %/K at 295 K and thermal conductance G_{th} of 1.07×10^{-7} W/K were measured. These measured values confirm the high temperature coefficient resistance and low thermal conductance of semiconducting YBaCuO microbolometer, thus confirm good thermal isolation from the substrate, which in turn provide higher sensitivity resulting in increased responsivity.

The optical response involved responsivity and detectivity measurements. The maximum responsivity of 1.62×10^{5} V/W and maximum detectivity of 3.51×10^{7}

cmHz$^{1/2}$/W were measured of a single YBaCuO microbolometer pixel (pixel size of 31x31 μm^2) from the 4x4 array CCBDI readout circuit for a 200 Hz frame rate. For the 30 Hz frame rate, the maximum responsivity of 1.24x10^5 V/W and maximum detectivity of 1.98x10^7 cmHz$^{1/2}$/W were measured of a single YBaCuO microbolometer pixel (pixel size of 31x31 μm^2) from the 4x4 array CCBDI readout circuit. These higher measured values of responsivity of a single YBaCuO microbolometer pixel from the 4x4 array CCBDI readout circuit for a faster frame rate of 200 Hz confirms higher sensitivity as a novel approach over that of a traditional 30 Hz frame.

The 18-μm-long electrode arm geometry provides a higher frame rate of 200 Hz over traditional 30 Hz frame rate and hence offers great potential for faster frame rate imaging in commercial, military and biomedical applications. The self-supporting semiconducting-YBaCuO based thermal detector using CCBDI readout circuit can be further enhanced with larger focal plane arrays (FPAs) for thermal imaging. Hence future research can focus on the improvement of the CCBDI readout circuit for higher frame rate with large FPAs resolution and applications for thermal imaging with smaller than 31 μm pitch design. Future work can also focus on a tradeoff that exists between the requirement of high readout performance and the capacity to afford additional circuit complexity, chip area and power dissipation. Future work will need timing circuitry to clock through one YBaCuO microbolometer pixel to another to obtain thermal image for each microbolometer pixel from the FPAs integrated with the CCBDI readout circuit.

REFERENCES

[1]. L. S. Johns, “Dual-use technology programs,” in Infrared Technology XX, Proc. SPIE 2269, 1994, pp.2-7.

[2]. C.-C. Hsieh, C.-Y. Wu, F.-W. Jih, and T.-P. Sun “Focal-Plane-Arrays and CMOS Readout Techniques of Infrared Imaging Systems”, IEEE Transactions on Circuits and Systems for Video Technology, Vol. 7, No. 4, August 1997.

[3]. http://www.nationalinfrared.com/image_browser2.php.

[4]. H. Jerominek, T. D. Pope, M. Renaud, N. R. Swart, F. Picard, M. Lehoux, S. Savard, G. Bilodeau, D. Audet “ 64x64, 128x128 and 240x320 pixel uncooled IR bolometric detector arrays” SPIE, vol. 3061.

[5]. P.W. Kruse, “A Comparison of the Limits to the performance of Thermal and Photon Detector Imaging Arrays,” Infrared Physics and Technology, vol. 36, p. 869, 1995.

[6]. J. F. Belcher, C. M. Hanson, H. R. Beratan, K. R. Udayakumar, K. L. Soch, “Uncooled Monolithic Ferroelectric IRFPA Technology,” SPIE, vol. 3436, p. 611, 1998.

[7]. B. Cole, R. Horning, B. Johnson, K. Nguyen, P. W. Kruse, and M. C. Foote, “High Performance Infrared Detector Array Using Thin Film Microstructures,” Proc Of 9th IEEE Int. Symp. on Application of Ferroelectric, p. 653, 1994.

[8]. W. Radford, R. Wyles, J. Wyles, J. Varesi, M. Ray, D. Murphy, A. Kennedy, A. Finch, E. Moody, F. Cheung, R. Coda, and S. Baur, “Microbolometer Uncooled Infrared Camera With 20 mK NETD,” SPIE, vol. 3436, p. 636, 1998.

[9]. Z. Celik-Butler and D. P. Butler, “Uncooled Infrared Detector Arrays,” Wiley Encyclopedia of Electrical and Electronics Engineering, vol. 10, p. 198, 1999.

[10]. P. C. Shan, Z. Celik-Butler, D. P. Butler and A. Jahanzeb, “Semiconducting YBaCuO thin films for uncooled infrared bolometers”, Journal of Applied Physics, 78 (12) pp 7334-7339, 1995.

[11]. A. M. Fowler, R. G. Probst, J. P. Britt, R. R. Joyce, and F. C. Gillett, “Evaluation of an indium antimonide hybrid focal plane array for ground-based infrared astronomy,” Opt. Eng., vol. 26, pp. 232–240, 1987.

[12]. N. Lum, J. Asbrock, R. White, R. Kelchner, L. Lum, L. Pham, C. McCreight, M. McKelvey, R. Jr. McMurray, W. Forrest, and J. Garnett, “Low-noise, low-temperature, 256 x 256 Si:As IBC staring FPA,” in Infrared Detectors and Instrumentation, Proc. SPIE, Apr. 1993, vol. 1946, pp. 100–109.

[13]. E. Beuville, M. Belding, A. Costello, R. Hansen and S. Petronio, “A High performance, low noise 128-channel readout integrated circuit for instrumentation and X-ray applications,” Nuclear Science Symposium Conference Record, IEEE, vol. 1, pp. 142-146, 16-22 Oct. 2004.

[14]. N. Bluzer and R. Stehlik, “Buffered direct injection of photocurrents into charge coupled devices,” IEEE Trans. Electron Devices, vol. 25, no. 2, pp. 160–166, 1978.

[15]. K. Chow, J. P. Rode, D. H. Seib, and J. D. Blackwell, “Hybrid infrared focal-plane arrays,” IEEE Trans. Electron Devices, vol. 29, no. 1, 1982.

[16]. J. T. Longo, D. T. Cheung, A. M. Andrewheung, A. M. Andrews, C. C. Wang, and J. M. Tracy, “Infrared focal planes in intrinsic semiconductors,” IEEE Trans. Electron Devices, vol. 25, no. 2, 1978.

[17]. L. J. Kozlowski, W. V. McLevige, S. A. Cabelli, A. H. B. Vanberwyck, D. E. Cooper, E. R. Blazejewski, K. Vural, and W. E. Tennant, “Attainment of high sensitivity at elevated operating temperatures with staring hybrid HgCdTe-on-Sapphire focal plane arrays,” Opt. Eng., vol. 33, no. 3, pp. 704–715, 1994.

[18]. P. Norton, “Infrared image sensors,” Opt. Eng., vol. 30, no. 11, pp. 1649–1660, 1991.

[19]. L. Kozlowski, S. Cabelli, R. Kezer, and W. Kleinhans, “10 x 132 CMOS/CCD readout with 25 μm pitch and on-chip signal processing including CDS and TDI,” in Infrared Readout Electronics, Proc. SPIE, 1992, vol. 1684, pp. 222–230.

[20]. C. Staller, L. Ramiirez, C. Niblack, M. Blessinger, and W. Kleiinhans, “A radiation hard, low background multiplexer design for spacecraft imager applications,” in Infrared Readout Electronics, Proc. SPIE, 1992, vol. 1684, pp. 175–181.

[21]. J.-L. Tissot, F. Rothan, C. Vedel, M. Vilain, J.-J. Yon, “LETI/LIR’s uncooled microbolometer development,” SPIE 3456, 605 (1998).

[22]. E. Mottin, J.-L. Martin, J.-L. Ouvrier-Buffet, M. Vilain, and J.-J. Yon, “320X240 microbolometer uncooled IRFPA,” SPIE 4028, 40 (2000).

[23]. C. Y. Wu, C. C. Hsieh, F. W. Jih, T. P. Sun, and S. J. Yang, “A new share-buffered direct-injection readout structure for infrared detector,” in Infrared Technology XIX, Proc. SPIE, 1993, vol. 2020, pp. 57–64.

[24]. C. Y. Wu and C. C. Hsieh, "New design techniques for a complementary metal-oxide semiconductor current readout integration circuit for infrared detector arrays," Opt. Eng., vol. 34, no. 1, pp. 160–168, Jan. 1995.

[25]. E.L. Dereniak, G.D. Boreman, Infrared Detectors and Systems, John Wiley & Sons Inc. New York, 1996.

[26]. W. L. Wolfe, " Infrared technology in Encyclopedia of Physical Sciences and Technology," Academic Press, 6, 648, 1987.

[27]. T. Bareen, N. Butler, M. Kohin, C. A. Marshall, R. Murphy, T. Parker, and R. Silva, "More applications of Uncooled Microbolometer Sensors," Proceedings of SPIE, 3436, 530, 1998.

[28]. A. L. Campbell, R. R. Naik, L. Sowards, and M. O. Stone, "Biological Infrared Imaging and Sensing," Micron, 33, 211, 2002.

[29]. F. Torella, R. Cowley, M. S. Thorniley, and C. N. McCollum, "Monitoring blood loss with near infrared spectroscopy," Comparative Chemistry and Physiology-Part A : Molecular and Integritive Physiology, 2002.

[30]. P. W. Kruse, D. D. Skatrud, "Uncooled Infrared Imaging Arrays and Systems," Semiconductors and Semimetals, vol. 47, pp. 43-121, Academic Press, New York, 1997.

[31]. D. P. Butler, Z. Celik-Butler, Roman Sobolewski "Yttrium Barium Copper Oxide as an Infrared radiation sensing material," Handbook of Advanced Electronic and Photonic Materials and Devices. vol 3, 2001.

[32]. A. Jahanzeb, C. M. Travers, D. P. Butler, Z. Celik-Butler, S. G. Tan "A Semiconductor YBaCuO Microbolometer for Room Temperature IR Imaging," IEEE, Transactions on Electron Devices, vol. 44, pp. 1795-1801, October 1997.

[33]. C. M. Travers, A. Jahanzeb, D. P. Butler, Z. Celik-Butler, S. G. Tan "Fabrication of Semiconducting YBaCuO Surface-Micromachined Bolometer Arrays," Journal of MEMS, vol. 6, no. 3, September 1997.

[34]. M. Almasri, D. P. Butler, Z. Celik-Butler "Uncooled Multimirror Broad-Band Infrared Microbolometers" Journal of MEMS, vol. 11, no.5, October 2002.

[35]. P. C. Shan, Z. Celik-Butler, D. P. Butler, A. Jahanzeb, C. M. Travers, W. Kula and R. Sobolewski, "Investigation of semiconducting YBaCuO thin films: A new room temperature bolometer", Journal of Applied Physics, 80 (12) pp 7118-7123, 1996.

[36]. M. Almasri, D. P. Butler, Z. Celik-Butler "Self-Supporting Uncooled Infrared Microbolometers with Low-Thermal Mass" Journal of MEMS, vol. 10, no. 3, September 2001.

[37]. H. Wada, T. Sone, H. Hata, Y. Nakaki, O. Kaneda, Y Ohta, M. Ueno, and M. Kimata, "YBaCuO uncooled microbolometer IRFPA," SPIE 4369, 297 (2001).

[38]. S. Mathews, "Thermal imaging on the rise", Laser Focus World, March 2004.

[39]. W. Radford, D. Murphy, M. Ray, S. Propst, A. Kennedy, J. Kojiro, J. Woolayaw and K. Soch, R. Coda, G. Lung, E. Moody, D. Gleichman, and S. Baur, "320x240 Silicon Microbolometer Uncooled IRFPAs With On-Chip Offset Correction", SPIE, Vol. 2746, pp. 82-93, 1996.

[40]. B.E. Cole, R. E.. Higashi, and R. A. Wood, "Monolithic Arrays of Micromachined Pixels for Infrared Application," IEEE Proc. International Electron Devices Meeting, pp. 459-462, 1998.

[41]. T. Breen, N. Butler, M. Kohin, C. A. Marshall, R. Murphy, T. Parker, R. Silva, "More Applications of Uncooled Microbolometer Sensors," SPIE, vol. 3436, pp. 530-540, 1998.

[42]. B. Meyer, R. Cannata, A. Stout, A. Gin, and P. Taylor, "Amber's Uncooled Microbolometer LWIR Camera," SPIE, vol. 2746, p. 13, 1996.

[43]. P. W. Kruse, D. D. Skatrud, "Uncooled Infrared Imaging Arrays and Systems," Semiconductors and Semimetals, vol. 47, pp. 43-121, Academic Press, New York, 1997.

[44]. R. A. Wood, "Use of Vanadium Oxide in Microbolometer Sensors," Patent No. 5450053, 1993.

[45]. R. E. Higashi, "Thermal Sensor and Method of Making same," Patent No. 6144285, 2000.

[46]. N. R. Butler, "Ambient Temperature IR Focal Plane Arrays," SPIE, vol. 4028, pp. 58-65, 2000.

[47]. R. A. Wood, "Use of Vanadium Oxide in Microbolometer Sensors," Patent No. Re.36615, 1997.

[48]. B.E. Cole, R.E. Higashi, and R.A. Wood, "Monolithic Two-dimensional arrays of micromachined microstructures for infrared applications," Proceedings of the IEEE 86, 1679 (1998).

[49]. C. Vedel, J. L. Martin, J. L. Ouvrier Buffet, J. L. Tissot, M. Vilain, and J. J. Yon, "Amorphous Silicon Based Uncooled Microbolometer IRFPA," SPIE, vol. 3698, pp. 276-283, 1999.

[50]. T. Schimert, D. Ratcliff, J. Brady, S. Ropson, R. Gooch, B. Ritchey, P. McCardel, K. Rachels, M. Wand, M. Weinstein, and J. Wynn, "Low Cost, Low Power Uncooled a:Si Based Micro Infrared Camera for Unattended Ground Sensor Applications," SPIE, vol. 3713, pp. 101-111, 1999.

[51]. J. Brady, T. Schimert, D. Ratcliff, R. Gooch, B. Ritchey, P. McCardel, K. Rachels, S. Ropson, M. Wand, M. Weinstein, and J. Wynn, "Advances in Amorphous Silicon Uncooled IR Systems," SPIE, vol. 3698, pp. 161-167, 1999.

[52]. W. Radford, R. Wyles, J. Wyles, J. Varesi, M. Ray, D. Murphy, A. Kennedy, A. Finch, E. Moody, F. Cheung, R. Coda, and S. Baur, "Microbolometer Uncooled Infrared Camera with 20 mK NETD," SPIE, vol. 3436, pp. 636-645, 1998.

[53]. M. S. Liu, J. S. Haviland and C. J. Yue, "Integrated Infrared Sensitive Bolometers," Patent No. US005260225A, 1992.

[54]. S. Sedky, P. Fiorini, K. Baert, L. Hermans, and R. Mertens, "Characterization and Optimization of Infrared Poly SiGe Bolometers," IEEE Transactions on Electron Devices, vol. 46, p. 675-682, 1999.

[55]. J. Wauters, "Doped Silicon Creates New Bolometer Material," Laser Focus World, pp. 145-149. 1997.

[56]. P. Fiorini, S. Sedky, M. Caymax and C. Baert, "Method of Fabrication of an Infrared Radiation Detector and Infrared Detector Device," Patent No. US009194722B1, 2001.

[57]. P. R. Gray, P. J. Hurst, S. H. Lewis, R. G. Meyer, Analysis and Design of Analog Integrated Circuits, John Wiley & Sons Inc. New York, 2001.

[58]. R. A. Wood in Uncooled Infrared Imaging Arrays and Systems, edited by P. W. Kruse and D. D. Skatrud, Semiconductors and Semimetals ~Academic, San Diego, 1997, vol. 47.

[59]. http://www.mosis.org.

[60]. T.-H. Yu, C.-Y. Wu, Y.-C. Chin, P.-Y. Chen, F.-W. Chi, J.-J. Luo, C.D. Chiang, and Y.-T. Cherng "A New CMOS Readout Circuit for Uncooled Bolometric Infrared Focal Plane Arrays", ISCAS 2000 - IEEE International Symposium on Circuits and Systems, May 28-31, (2000), II-493, Geneva, Switzerland.

[61]. Y. Shih and C. Wu, "The design of high-performance 128x128 CMOS image sensors using new current-readout techniques", IEEE International Symposium on Circuits and Systems, Albuquerque, New Mexico, USA, Nov. (1999), pp. 168-171.

[62]. A. Mahmood, S. Dayeh, D. P. Butler, Z. Celik-Butler, "Micromachined Infrared Sensor Arrays on Flexible Polyimide Substrates", IEEE Sensors 2003, pp 777-782, Toronto, Canada, 2003.

[63]. A. Yildiz, Z. Celik-Butler and D. P. Butler, "Microbolometers on a Flexible Substrate for Infrared Detection", IEEE Sensors Journal, 4, pp. 112-117, 2004.

[64]. A. Yaradanakul, D. P. Butler and Z. Celik-Butler, “Uncooled Infrared Microbolometers on a Flexible Substrate”, IEEE Transactions on Electron Devices, 49, pp. 930-933, 2002.

[65]. http://www.irfilters.reading.ac.uk/library/technical_data/infrared_materials/znse.htm.

[66]. http://www.drsinfrared.com.

BIOGRAPHICAL INFORMATION

Sandeep Kumar received his BS degree in electronics and communication from JMI University, India in 1998. He received his MS degree in electrical engineering from the University of Texas at Arlington, USA in 2002. He completed his PhD in electrical engineering from the University of Texas at Arlington, USA in 2007.

His graduate and professional experience include VLSI and solid state electronics, design, fabrication and characterization of CMOS compatible uncooled infrared micro-electro-mechanical systems (MEMS) sensors on silicon substrate.